Monte Carlo-based Development of a Shield and Total Background Estimation for the COBRA Experiment

Dissertation
zur Erlangung des Doktorgrades
des Fachbereichs Physik
der Universität Hamburg

vorgelegt von
Nadine Heidrich
aus Perleberg

Hamburg
2014

Monte Carlo-based
Development of a Shield and
Total Background Estimation
for the COBRA Experiment

Abstract

The COBRA experiment aims for the measurement of the neutrinoless double beta decay and thus for the determination the effective Majorana mass of the neutrino. To be competitive with other next-generation experiments the background rate has to be in the order of 10^{-3} counts/kg/keV/yr, which is a challenging criterion. This thesis deals with the development of a shield design and the calculation of the expected total background rate for the large scale COBRA experiment containing 13824 $6\,cm^3$ CdZnTe detectors. For the development of a shield single-layer and multi-layer shields were investigated and a shield design was optimized concerning high-energy muon-induced neutrons. As the best design the combination of $10\,cm$ boron doped polyethylene as outermost layer, $20\,cm$ lead and $10\,cm$ copper as innermost layer were determined. It showed the best performance regarding neutron attenuation as well as (n,γ) self-shielding effects leading to a negligible background rate of less than $2{\cdot}10^{-6}$ counts/kg/keV/yr. Additionally. the shield with a thickness of $40\,cm$ is compact and cost- effective. In the next step the expected total background rate was computed taking into account individual setup parts and various background sources including natural and man-made radioactivity, cosmic ray-induced background and thermal neutrons. Furthermore, a comparison of measured data from the COBRA demonstrator setup with Monte Carlo data was used to calculate reliable contamination levels of the single setup parts. The calculation was performed conservatively to prevent an underestimation. In addition, the contribution to the total background rate regarding the individual detector parts and background sources was investigated. The main portion arise from the Delrin support structure, the Glyptal lacquer followed by the circuit board of the high voltage supply. Most background events originate from α particles with a quantity of 99 % in total. Regarding surface events a contribution of 26.8 % was determined. Altogether, a background of less than $54{\cdot}10^{-3}$ counts/kg/keV/yr was determined showing the potential of the COBRA experiment.

Monte-Carlo-basierte
Entwicklung einer Abschirmung und
Gesamtuntergrundbestimmung
für das COBRA-Experiment

Kurzfassung

Das Ziel des COBRA-Experiments ist die Messung des neutrinolosen Doppelbetazerfalls und die damit verbundene Bestimmung der effektiven Majoranamasse des Neutrinos. Um konkurrenzfähig gegenüber anderen Experimenten zu sein, muss eine Untergrundrate in der Größenordnung von 10^{-3} Ereignissen/kg/keV/yr erreicht werden, was ein herausforderndes Kriterium ist. Diese Doktorarbeit beschäftigt sich mit der Entwicklung einer Abschirmung und der Berechnung der zu erwartenden Gesamtuntergrundrate für das COBRA-Großexperiment. Insgesamt beinhaltet das aktuelle Design für ein Großexperiment 13824 $6\,cm^3$ CdZnTe Detektoren. Für die Entwicklung der Abschirmung wurden einzelnen und mehreren Materialien im Kombination untersucht und das Design bezüglich hochenergetischer Myon-induzierter Neutronen optimiert. Als bestes Design wurde eine Kombination aus 10 cm Bor-dotiertem Polyethylen als äußerster Schicht, 20 cm Blei und 10 cm Kupfer als innerster Schicht bestimmt. Es zeigte das beste Ergebnis in Bezug auf Moderation und Absorption von Neutronen, sowie auf (n,γ) Selbstabschirmungseffekte. Dies führte zu einer vernachlässigbaren Untergrundrate von weniger als $2{\cdot}10^{-6}$ Ereignissen/kg/keV/yr. Darüber hinaus ist die Abschirmung mit einer Dicke von 40 cm kompakt und kosteneffizient. Im nächsten Schritt wurde die zu erwartende Gesamtuntergrundrate berechnet. Dazu wurden einzelne Teile des Aufbaus und verschiedene Untergrundquellen, wie natürliche und menschengemachte Radioaktivität, induzierter Untergrund durch kosmische Strahlung, sowie thermische Neutronen, berücksichtigt. Außerdem wurden gemessene Daten vom COBRA-Demonstrationsaufbau mit Monte-Carlo-Daten verglichen, um glaubwürdige Kontaminationslimits für einzelne Teile des Aufbaus zu bestimmen. Die Berechnung erfolgte konservativ, um eine Unterschätzung zu verhindern. Darüber hinaus wurden die Beiträge bezüglich der einzelnen Teile des Experimentenaufbaus und der einzelnen Untergrundquellen untersucht. Der Hauptbeitrag zur Gesamtuntergrundrate stammt von der Delrin-Halterung, dem Glyptallack gefolgt von der Leiterplatte für die Hochspannungsversorgung. Die meisten Untergrundereignisse werden durch α-Teilchen verursacht mit einer Häufigkeit von 99 %. Hinsichtlich Oberflächenereignisse wurde ein Beitrag von 26.8 % bestimmt. Insgesamt wurde eine Untergrundrate von weniger als $54{\cdot}10^{-3}$ Ereignissen/kg/keV/yr bestimmt, was das Potenzial des COBRA-Experiments zeigt.

Contents

Chapter 1

Preface and Motivation

"Neutrino physics is largely an art of learning a great deal by observing nothing."[1]
There is a grain of truth in this quotation and so it took over 20 years to detect
(anti-electron-) neutrinos the first time by F Reines and C.L. Cowan, although they
were postulated in 1930 by W. Pauli.

Nowadays neutrinos play an important role in cosmology as well as in modern parti-
cle and astroparticle physic. Furthermore, their properties are of fundamental interest.
Many neutrino oscillation experiments were a complete success in the last years, deter-
mining the parameters of the PMNS matrix. However, many questions concerning these
properties are still unanswered so far. Next to the unknown masses of neutrinos, their
ordering in the mass hierarchy as well as electromagnetic properties, their nature itself
being Dirac or Majorana particle is not clarified. In the Standard Model all particles
are Dirac particles leading to a distinction between particles and antiparticles. Yet, due
to the lack of additive properties, like charge, it is reasonable to assume that neutrinos
and anti-neutrinos are the same particles, hence Majorana particles. This would offer an
explanation of the small neutrino masses, also compared to their corresponding leptons,
through the Seesaw mechanism. In addition, the baryon asymmetry could be explained
under the assumption of a previous lepton asymmetry (leptogenesis) [2]. Additionally,
neutrinos would have a special role in the SM, being the only singlet fermion.

One way to answer this question is the measurement of the neutrinoless double beta de-
cay. Although the underlying physics occurring in this process are unknown, it is a fact
after the Schechter-Valle theorem, that the neutrinos have to be a Majorana particle.
The first hint of the neutrinoless double beta decay was given by the Heidelberg-Moscow
experiment in 2001. However, the result was controversial and furthermore, has been
recently refuted by the GERDA experiment in 2013.

One of the next-generation neutrinoless double beta experiments is COBRA aiming for
the measurement and thus discovery of the effective Majorana mass of less than $0.05\,\mathrm{eV}$
corresponding roughly to a half-life in the order of 10^{26} years. A crucial criterion to

---

[1]Haim Harari, Isreali physicist, [1]

achieve such half-life is, beside a high source mass and good energy resolution, an extremely low background rate. It has to be in the order of 10^{-3} counts/kg/keV/yr, which is a challenging aspect. All materials close to the detector as well as the detector material itself have to be radiopure. Furthermore, not only a shield must reduce external radiation sources effectively to a minimum, but also has to be constructed in a way it is as compact and cost-efficient as possible. Next to contamination measurements of all detector parts and test operation at a demonstrator setup in a low background environment, like an underground laboratory, a Monte Carlo survey to estimate the total expected background rate is mandatory.

In this thesis the Monte Carlo-based development of a radiation shield and the total background estimation for the COBRA experiment are presented. The full Monte Carlo campaign to determine the total background rate was done for the first time. Furthermore, measured data from the COBRA demonstrator setup at LNGS were used to compute contamination levels of operated detector parts. Chapter 2 gives an introduction on neutrino properties, double beta decay and particle interactions in matter. Additionally, background sources and Monte Carlo simulations are discussed in general. In Chapter 3 the COBRA experiment is presented including the concept of COBRA, the detector technology and the description of the demonstrator setup. The development of a shield follows in Chapter 4 starting with the explanation of the used method and pursued by the discussion about single-layer and multi-layer shields. A multi-layer shield design was optimized concerning the attenuation of high-energetic muon-induced neutrons and (n,γ) self-shielding effects resulting in a negligible background rate for fast neutrons. Chapter 5 deals with the total background estimation. Here, the individual parts of the setup are regarded concerning their contamination and contribution to the total background rate. Furthermore, a comparison to the measured data from the demonstrator setup is made to determine upper limits on the contamination levels of detector parts. Various background sources including natural and man-made radioimpurities in the environment, shield material and detector itself as well as cosmic ray-induced background and thermal neutrons are taken into account. Furthermore, each individual setup part is regarded separately. In the end, a conclusion is given in Chapter 6 including a discussion about the obtained results.

Chapter 2

Introduction

2.1 Neutrino Properties

Neutrinos are fundamental leptons with spin-$\frac{1}{2}$ like other fermions in the Standard Model (SM). Generally, in quantum field theory spin-$\frac{1}{2}$ particles are described by four-component spinors $\psi(x)$ which obey the Dirac equation

$$(i\gamma^\mu \partial_\mu - m)\,\psi = 0 \text{ with } \mu = 0, 1, 2, 3. \tag{2.1}$$

Here γ^μ are 4×4 matrices given in the common form

$$\gamma^0 = \begin{pmatrix} 1 & 0 \\ 0 & -1 \end{pmatrix} \text{ and } \gamma^i = \begin{pmatrix} 0 & \sigma_i \\ -\sigma_i & 0 \end{pmatrix} \text{ with i} = 1, 2, 3 \tag{2.2}$$

with σ_i corresponding to the 2×2 Pauli matrices

$$\sigma_1 = \begin{pmatrix} 0 & 1 \\ 1 & 0 \end{pmatrix}, \, \sigma_2 = \begin{pmatrix} 0 & -i \\ i & 0 \end{pmatrix}, \, \sigma_3 = \begin{pmatrix} 1 & 0 \\ 0 & -1 \end{pmatrix}. \tag{2.3}$$

The four independent components of the spinors $\psi(x)$ relate to particles and antiparticles with two possibilities for the helicity $\mathcal{H}$

$$\mathcal{H} = \frac{\vec{\sigma} \cdot \vec{p}}{|\vec{p}|} \tag{2.4}$$

with the standardized spin $\vec{\sigma}$ and the momentum $\vec{p}$. In addition, any spinor ψ can be written in chiral projections as

$$\psi = (P_L + P_R)\psi = P_L\psi + P_R\psi = \psi_L + \psi_R \tag{2.5}$$

with the two projection operators

$$P_{L,R} = \frac{1}{2}\left(1 \mp \gamma^5\right) \text{ with } \gamma^5 = i\gamma^0\gamma^1\gamma^2\gamma^3 = \begin{pmatrix} 0 & 1 \\ 1 & 0 \end{pmatrix}. \tag{2.6}$$

For massless particles, e.g. neutrinos in the SM, helicity and chirality are identical and it is an experimental fact that only left-handed neutrinos ($\mathcal{H} = -1$) and right-handed antineutrinos ($\mathcal{H} = +1$) are observed. Therefore, a two-component spinor (Weyl spinor) should be sufficient to describe neutrinos in principle.

Although neutrinos play an important role in particle and astro physics, as well as in cosmology, many properties are not known at the moment. One question refers to the nature of neutrinos. For all fundamental fermions in the SM it is possible to distinguish between particle and antiparticle by their charge (Dirac particles), except for neutrinos. They are possible Majorana particles [3]. Necessary requirements for Majorana particles to exist are vanishing additive quantum numbers, like charge, lepton number, etc. In conclusion, the lepton number is violated if neutrinos are Majorana particles. They can be distinguished by their helicity or chirality via CP transformation. The charge conjugation operator C transforms a right(left)-handed particle into a right(left)-handed antiparticle with untouched helicity and chirality. Only an additional parity transformation P changes as well the helicity. Therefore, a right(left)-handed particle is converted into a left(right)-handed antiparticle [4, 5].

Another open question is about the mass of neutrinos. In the SM neutrinos are supposed to be massless, but experiments, for example the Super-Kamiokande experiment [6], have shown a flavor oscillation comparable to the quark sector, where the weak and mass eigenstates are not identical, but connected via the CKM matrix[1]. For neutrinos the weak eigenstates $|\nu_\alpha\rangle$ with $\alpha = e, \mu, \tau$ and mass eigenstates $|\nu_i\rangle$ with $i = 1, 2, 3$ are connected via the PMNS matrix[2] U

$$|\nu_\alpha\rangle = \sum_{i=1}^{3} U_{\alpha i}|\nu_i\rangle. \tag{2.7}$$

The oscillations require that not all mass eigenstates have the same eigenvalue m_i. Especially, they demand that not all m_i are zero and thus, massless. In addition, such oscillations do not conserve individual lepton numbers, only total lepton number. For Dirac particles the 3×3 PMNS matrix can be described with three weak mixing angles and a CP-violating phases. For Majorana particles two additional phases are introduced, because of the requirement of identical particles and antiparticles. The observation of oscillations does not allow absolute mass measurements. It is only sensitive to Δm_{ij}^2

---

[1]CKM matrix: Cabibbo-Kobayashi-Maskawa matrix, Unitary matrix, which can be parametrized with three mixing angles and a phase [7]. It describes the flavor and mass eigenstate mixing in the quark sector. Current experimental results for the values can be found in [8].

[2]PMNS matrix: Pontecorvo-Maki-Nakagawa-Sakata matrix [9]. Current experimental results for the values can be found in [8].

with $i, j = 1, 2, 3$. Recent results are given by [8]

$$\Delta m_{21}^2 = 7.50^{+0.19}_{-0.20} \cdot 10^{-5} \, \text{eV}^2 \tag{2.8}$$
$$\left|\Delta m_{32}^2\right| \approx \left|\Delta m_{31}^2\right| = 2.32^{+0.12}_{-0.08} \cdot 10^{-3} \, \text{eV}^2.$$

Because Δm_{32}^2 can be positive or negative, two potential orderings, also called hierarchies, emerge, shown in Figure 2.1. In the normal hierarchy ν_3 is the heaviest and in the inverted hierarchy ν_3 is the lightest neutrino. Determination of the neutrino mass hierarchy is a fundamental step in neutrino physics, because it can be used, for example, to calculate the absolute mass scale of neutrinos, as well as define the scope for neutrinoless double beta decay experiments [10], see Chapter 2.2.1. Current and future experiments are, for example, NOνA[3], JUNO[4] and PINGU[5].
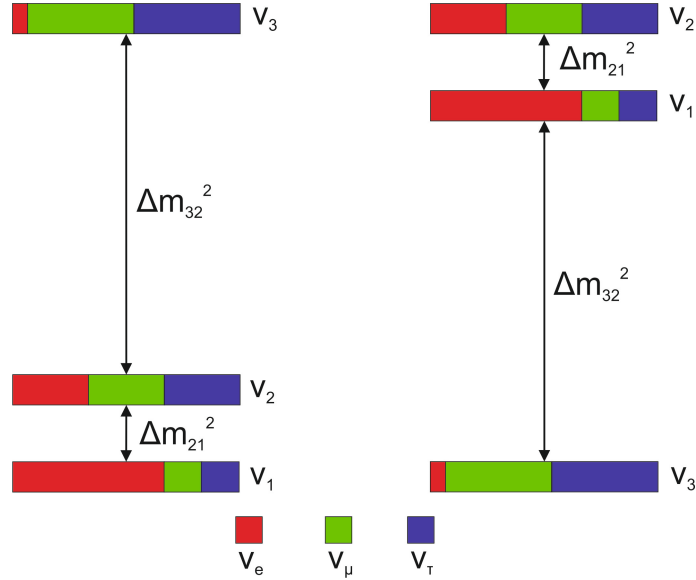
Figure 2.1: Depicted are the two neutrino mass hierarchies. In the normal hierarchy (on the left hand side) ν_3 is the heaviest, in the inverted hierarchy (on the right hand side) it is the lightest neutrino.

An upper limit for the summed neutrino mass was determined by the PLANCK[6] experiment [16]

$$M = \sum_i m_i = 0.23 \, \text{eV} \tag{2.9}$$

from cosmological constraints based on the measurements of the cosmic microwave background (CMB), lensing-potential power spectra and baryon acoustic oscillation (BAO) data.

---

[3]NOνA: NuMI Off-Axis ν_e Appearance, USA [11]
[4]JUNO: Jiangmen Underground Neutrino Observatory, China [12]
[5]PINGU: Precision IceCube Next Generation Upgrade, South Pole [13, 14]
[6]PLANCK: named after German physicist Max Planck, space observatory [15]

Direct methods for neutrino mass determinations are, for example, based on kinematic arguments of the β decay. Here, the upper endpoint of the electron spectrum and the curvature of the spectrum near the endpoint are sensitive to m_{ν_e}, which is the incoherent sum of the mass eigenvalues m_i with $i = 1, 2, 3$

$$m_{\nu_e} = \sqrt{\sum_i |U_{ei}|^2\, m_i^2}. \tag{2.10}$$

The best constraints on m_{ν_e} come from the tritium decay. The recent result on the upper limit is given by [17, 8]

$$m_{\nu_e} < 2\,\mathrm{eV}. \tag{2.11}$$

Past and future experiments in this sector are the Mainz [18] and the KATRIN[7] experiment.

Furthermore, a sensitive probe of Majorana neutrino masses is provided by the neutrinoless double beta decay, see also Chapter 2.2.1. If the electron neutrino is indeed a Majorana mass eigenstate, the effective Majorana mass is given by the coherent sum

$$\langle m_{\beta\beta}\rangle = \left|\sum_i U_{ei}^2 m_i\right| = \left|\sum_i |U_{ei}|^2\, e^{2i\alpha_i} m_i\right| \tag{2.12}$$

with the Majorana phases α_i. A first controversial result was published by the former Heidelberg-Moscow experiment in 2001 [20, 21, 22]

$$\langle m_{\beta\beta}\rangle = 0.32^{+0.03}_{-0.03}\,\mathrm{eV}. \tag{2.13}$$

However, in 2013 the current GERDA[8] experiment announced first results disproving the Heidelberg-Moscow experiment [23, 24].

From the theoretical point of view a Dirac mass term of the form

$$-\mathcal{L}_D = m_D \left(\overline{\psi_L}\psi_R + \overline{\psi_R}\psi_L\right) \tag{2.14}$$

with $\overline{\psi_R}\psi_L = \left(\overline{\psi_L}\psi_R\right)^+$ and $\overline{\psi_L}\psi_L = \overline{\psi_R}\psi_R = 0$ mixes two different Weyl spinors of opposite chirality corresponding to the type of mass generated in the SM. The exclusion of right-handed neutrinos therefore ensures that neutrinos are massless [4].

A Majorana mass term can be written with only one Weyl spinor ψ and its charge conjugated ψ^c of the form

$$-\mathcal{L}_M = \frac{1}{2}\left(m_M \overline{\psi}\psi^c + m_M^* \overline{\psi^c}\psi\right) \tag{2.15}$$

---

[7]KATRIN: Karlsruhe Tritium Neutrino, Germany [19]
[8]GERDA: Germanium Detector Array, Italy

with m_M called the Majorana mass. Using the chiral projections of ψ and ψ^c one gets two hermitian mass terms

$$
\mathcal{L}_M = \mathcal{L}_M^L + \mathcal{L}_M^R \text{ with}
$$
$$
-\mathcal{L}_M^L = \frac{1}{2} m_L \left(\overline{\psi_L} \psi_R^c + \overline{\psi_R^c} \psi_L \right) \tag{2.16}
$$
$$
-\mathcal{L}_M^R = \frac{1}{2} m_R \left(\overline{\psi_R} \psi_L^c + \overline{\psi_L^c} \psi_R \right).
$$

Defining two Majorana fields $\phi_{1,2}$

$$
\phi_1 = \psi_L + \psi_R^c \text{ and } \phi_2 = \psi_R + \psi_L^c \tag{2.17}
$$

Equation 2.16 can be rewritten as

$$
-\mathcal{L}_M^L = \frac{1}{2} m_L \overline{\phi_1} \phi_1 \text{ and } -\mathcal{L}_M^R = \frac{1}{2} m_R \overline{\phi_2} \phi_2. \tag{2.18}
$$

Here, $\psi_{L,R}$ are interaction eigenstates, while $\phi_{1,2}$ are mass eigenstates. In general, both types of mass are combined corresponding to the Dirac–Majorana mass term

$$
-2\mathcal{L}_{DM} = m_D \left(\overline{\psi_L} \psi_R + \overline{\psi_L^c} \psi_R^c \right) + m_L \overline{\psi_L} \psi_R^c + m_R \overline{\psi_L^c} \psi_R + h.c.
$$

$$
= \left(\overline{\psi_L} \, \overline{\psi_L^c} \right) \begin{pmatrix} m_L & m_D \\ m_D & m_R \end{pmatrix} \begin{pmatrix} \psi_R^c \\ \psi_R \end{pmatrix} + h.c. \tag{2.19}
$$

$$
= \overline{\Psi_L} M \Psi_R^c + \overline{\Psi_R^c} M \Psi_L
$$

with the mass matrix M, $\Psi_L = \begin{pmatrix} \psi_L \\ \psi_L^c \end{pmatrix}$ and $\Psi_R^c = (\Psi_L)^c = \begin{pmatrix} \psi_R^c \\ \psi_R \end{pmatrix}$.

In the SM only the fields ψ_L and ψ_R^c are present, but not the fields ψ_R and ψ_L^c. They are also called sterile neutrinos and do not participate in weak interaction in the SM. The mass eigenstates can be calculated by diagonalizing M with a transformation matrix T [25]. They are given by

$$
\tilde{m}_{1,2} = \frac{1}{2} \left[(m_L + m_R) \pm \sqrt{(m_L - m_R)^2 + 4m_D^2} \right]. \tag{2.20}
$$

The eigenvalues can be either negative or positive. To obtain positive masses, one uses $\tilde{m}_k = \epsilon_k m_k$ with $m_k = |\tilde{m}_k|$, $\epsilon_k = \pm 1$ and $k = 1, 2$ [26].

Some interesting aspects are:

- $m_L = m_R = 0$
  Resulting in $m_{1,2} = m_D$ with two degenerate Majorana eigenstates emerging, which can be used to construct a Dirac field with a corresponding Dirac mass term. Therefore, a Dirac field can be seen as a composite of two degenerate Majorana fields [25].

- $m_D = 0$
  Resulting in $m_{1,2} = m_{L,R}$ corresponding to the pure Majorana case [25].

- $m_R \gg m_D$, $m_L = 0$

  This scenario is popular within the seesaw model of neutrino mass generation consisting of making one particle light at the expense of making another heavy. One obtains two mass eigenvalues

  $$m_1 = \frac{m_D^2}{m_R} \ll m_D^2 \text{ and } m_2 = m_R \left(1 + \frac{m_D^2}{m_R^2} \right) \approx m_R. \qquad (2.21)$$

  Thus, if the Majorana mass m_R is sufficiently large, the observable mass m_1 is reduced in a way that they explain the upper limits of current experimental data, even though m_D is of the order of MeV–GeV. Therefore, the seesaw mechanism also provides an explanation of the intra-familial hierarchy $m_\nu \ll m_D$, while the Dirac neutrino masses are similar to the Dirac masses of other fermions of the same generation [4, 5].

The generalization to n flavors requires an n-component Weyl spinor in flavor space with normal Weyl spinors of different flavor as entries. The masses are correspondingly $n \times n$ matrices [27].

2.2   Double Beta Decay

The double beta decay ($\beta\beta$ decay) is a low-energy nuclear process which changes the nuclear charge Z by two units while leaving the atomic mass A unchanged. The transition takes place among isobaric isotopes. With the Weizsäcker mass formula [28] the isobars can be described as

$$\begin{aligned}
E_B &= \Delta m \cdot c^2 \\
&= a_V A - a_S A^{\frac{2}{3}} - a_F \left(N - Z \right)^2 - a_C Z^2 \cdot A^{-\frac{1}{3}} + \delta \cdot a_p A^{-\frac{1}{2}}.
\end{aligned} \qquad (2.22)$$

Here, E_B is the binding energy of a nucleus with empirically determined constants a_V, a_S, a_F, a_C, a_P and the number density N. The factor δ corresponds to the pairing energy and is given by

$$\delta = \begin{cases} +1 & \text{for even-even nuclei} \\ 0 & \text{for even-odd or odd-even nuclei} \\ -1 & \text{for odd-odd nuclei.} \end{cases} \qquad (2.23)$$

For odd A the pairing energy vanishes resulting in one parabola, while for even A two separate parabolas emerge allowing for $\beta\beta$ decay, which is schematically depicted in Figure 2.2 for $A = 116$. Hence, all $\beta\beta$ decay emitters are even-even nuclei.

The $\beta\beta$ decay can be understood as two subsequent β decays via a virtual intermediate state. This requires that the ground or excited state of the first daughter-nucleus $m(Z + 1, A)$ has to be energetically higher (see Figure 2.2: Cd compared to In) and
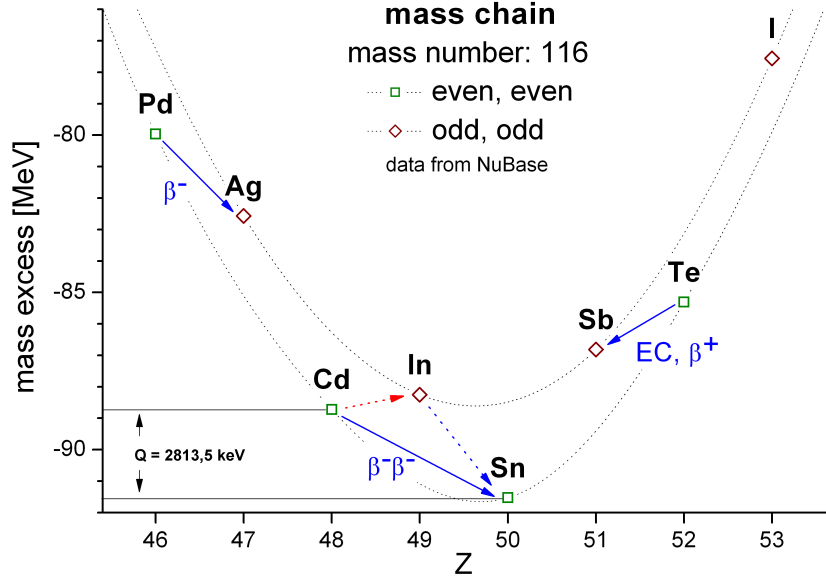
Figure 2.2: Depicted is the binding energy/mass excess versus Z for $A = 116$ corresponding to the Weizsäcker mass formula. For even A two separate isobars emerge allowing for $\beta\beta$ decay. [29]

in contrast the second daughter-nucleus $m(Z + 2, A)$ has to be energetically lower (see Figure 2.2: Cd compared to Sn) than the original one $m(Z, A)$:

$$m(Z + 1, A) > m(Z, A) > m(Z + 2, A). \tag{2.24}$$

Thus, a single beta decay is energetically impossible and two successive single beta decays are therefore forbidden. So far 36 $\beta\beta$ decay emitters with different decay modes are known and listed in [30].

2.2.1   Decay Modes

There are two different decay modes for the $\beta\beta$ decay including either two ($2\nu\beta\beta$ decay) or no ($0\nu\beta\beta$ decay) neutrinos. The Feynman diagrams are depicted in Figure 2.3, showing in Figure 2.3a the $2\nu\beta\beta$ decay and in Figure 2.3b the $0\nu\beta\beta$ decay. In addition, the two-nucleon (2n mechanism) is described, neglecting other mechanisms [31].

The 2ν Double Beta Decay

The $\beta\beta$ decay was first discussed in the form

$$(Z, A) \rightarrow (Z + 2, A) + 2e^- + 2\overline{\nu}_e \tag{2.25}$$

by M. Goeppert – Mayer in 1935 [32] describing two simultaneous neutron decays including two neutrinos, which is also shown as a Feynman diagram in Figure 2.3a. Since
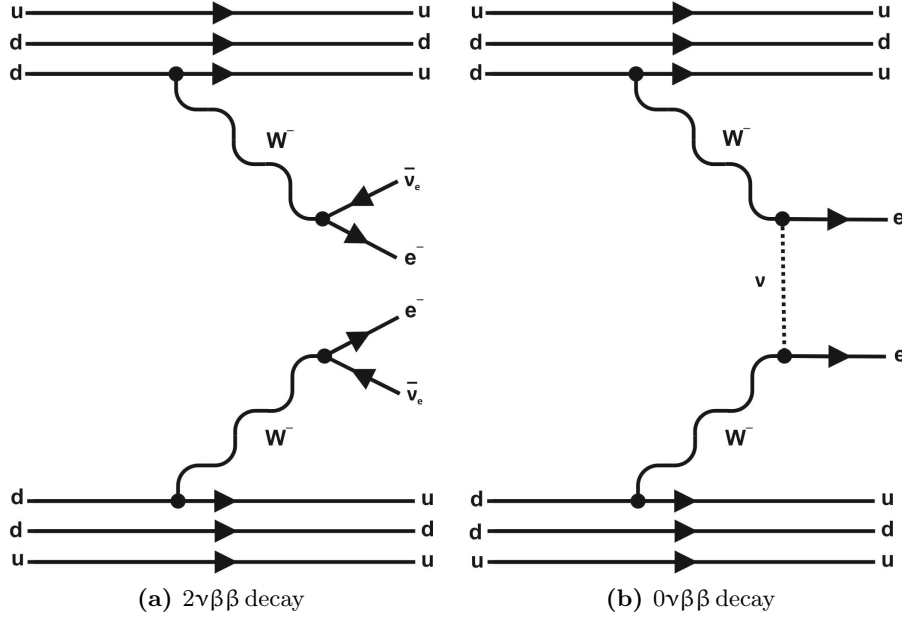
(a) $2\nu\beta\beta$ decay   **(b)** $0\nu\beta\beta$ decay

Figure 2.3: Depicted are the Feynman diagrams for the $2\nu\beta\beta$ decay (on the left-hand side) and $0\nu\beta\beta$ decay (on the right-hand side) with either two neutrinos or no neutrino in the final state. For the $0\nu\beta\beta$ decay the 2n mechanism is illustrated.

this process conserves the lepton number, it is allowed within the SM. In addition, the prediction of massless neutrinos in the SM is consistent with the decay mode. As the $2\nu\beta\beta$ decay is a higher-order effect, expected half-lifes are long compared to the regular β decay. For ^{116}Cd, for example, the NEMO[9] 2 experiment determined a half-life of

$$T_{\frac{1}{2}}^{^{116}\mathrm{Cd}} = (3.75 \pm 0.35 \pm 0.21) \cdot 10^{19}\,\mathrm{yr}\ [8]. \tag{2.26}$$

The 0ν Double Beta Decay

The second possible decay mode was introduced by W. H. Furry in 1939 [36] in the form of

$$(Z, A) \rightarrow (Z + 2, A) + 2e^- \tag{2.27}$$

with no neutrino in the final state. The Feynman diagram is shown in Figure 2.3b. Violating the lepton number conservation by two units, this process is forbidden in the SM. The $0\nu\beta\beta$ decay can be understood as two subsequent steps, called the "Racah sequence"

$$\begin{aligned}(Z, A) \rightarrow &(Z + 1, A) + e^- + \overline{\nu}_e\\ (Z + 1, A) + \nu_e \rightarrow &(Z + 2, A) + e^-.\end{aligned} \tag{2.28}$$

---

[9]NEMO: Neutrino Ettore Majorana Observatory, France [33, 34, 35]

First a neutron decays emitting a right-handed $\overline{\nu}_e$, which has to be absorbed at a second neutron within the same nucleus as left-handed ν_e. To fulfill these requirements, both particle and antiparticle have to be identical. Thus, the neutrino has to be a Majorana particle. Furthermore, a mechanism allowing for helicity matching is required. There are different possibilities satisfying this condition. Here, neutrino masses are the most popular one, because neutrino mass eigenstates for $m_\nu > 0$ have no fixed helicity and besides the dominant left-handed contribution, have an admixture of a right-handed one. A second method accounting for helicity matching could be a new interaction allowing for right-handed currents.

Besides the unknown underlying mechanism of the decay, it is possible to relate the 0νββ decay to a non zero effective Majorana mass for the electron neutrino after the Schechter-Valle theorem (Black Box theorem) [37], which is schematically illustrated in Figure 2.4. The two emitted electrons with the two u and d quarks can be coupled to the two ν_e at some loop level in a way a Majorana mass term occurs.
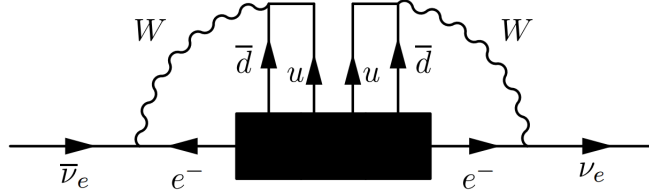
Figure 2.4: Schematically depicted is the Schechter-Valle theorem. A positive observation of the 0νββ decay would prove a finite Majorana mass regardless the underlying mechanism illustrated as Black Box operator. [37]

However, the 0νββ decay can effectively be seen as a scattering process with the Black Box as operator, which arises underlying new physics [38].

Alternative processes

Equivalent to the previously discussed β⁻β⁻ decay the β⁺β⁺ decay also in combination with electron capture (EC) exists. Three different variants are possible:

$$(Z, A) \to (Z - 2, A) + 2e^+ (+2\nu_e) \tag{2.29}$$

$$e_B^- + (Z, A) \to (Z - 2, A) + e^+ (+2\nu_e) \tag{2.30}$$

$$2e_B^- + (Z, A) \to (Z - 2, A)(+2\nu_e) \tag{2.31}$$

The β⁺β⁺ decay is always accompanied by EC/EC or β⁺/EC and additionally the 2νββ decay and 0νββ decay mode are feasible. Only six nuclei are known, which can undergo these processes. The expected half-lifes for the β⁺β⁺ decay are in the order of 10^{26} years, because the transition energy Q, also called Q-value, is reduced by a factor of $4m_ec^2$. The processes in combination with EC have lower half-lifes making the experiment more realistic, but are harder to detect experimentally.

Furthermore, $\beta^+\beta^+$ decay modes have an enhanced sensitivity to right-handed currents allowing for a clarification of the underlying physics mechanism, if the $0\nu\beta\beta$ decay exists and will ever be observed [39].

2.2.2   Decay Rates

Starting from Fermi's Golden Rule the decay rates can be described analogously to the β decay keeping in mind that the $\beta\beta$ decay is of second-order perturbation theory. Regarding only ground-state transitions the decay rate $\lambda_{2\nu}$ is

$$\frac{\lambda_{2\nu}}{\ln 2} = \left(T_{\frac{1}{2}}^{2\nu}\right)^{-1} = G^{2\nu}\left(Q,Z\right)\left|M_{GT}^{2\nu} + \frac{g_V^2}{g_A^2}M_F^{2\nu}\right|^2 \qquad (2.32)$$

with $G^{2\nu}$ as the phase space and the matrix elements $M_{GT}^{2\nu}$ for Gamow-Teller transitions and $M_F^{2\nu}$ for Fermi transitions [27]. The Fermi transitions are forbidden or strongly suppressed due to isospin selection rules. The decay rate can be approximated with [27]

$$\lambda_{2\nu} \propto Q^{11} \qquad (2.33)$$

with the transition energy $Q = E_{e1} + E_{e2} + E_{\nu 1} + E_{\nu 2} - 2m_e$ and therefore scales with Q^{11}.

The neutrinoless case requires as already mentioned neutrinos to be Majorana particles and further a helicity matching. The different mechanisms allowing helicity mismatch are associated with different nuclear matrix elements. Considering massive Majorana neutrinos only the decay rate is given by

$$\frac{\lambda_{0\nu}}{\ln 2} = \left(T_{\frac{1}{2}}^{0\nu}\right)^{-1} = G^{0\nu}\left(Q,Z\right)\left|M_{GT}^{0\nu} - M_F^{0\nu}\right|^2 \left(\frac{\langle m_{\beta\beta}\rangle}{m_e}\right)^2 \qquad (2.34)$$

or approximately

$$\lambda_{0\nu} \propto Q^5 \qquad (2.35)$$

with $Q = E_{e1} + E_{e2} - 2m_e$ [27]. Hence, the half-life $T_{\frac{1}{2}}^{0\nu}$ scales with a factor of Q^{-5} compared to Q^{-11} for $2\nu\beta\beta$ decay resulting in a lower half-life for higher Q-values.

The phase space for $0\nu\beta\beta$ decay is larger than for $2\nu\beta\beta$ decay, because the number of final states is restricted by the Q-value, which is below $5\,\mathrm{MeV}$, for the real emitted neutrinos in the $2\nu\beta\beta$ decay case. The virtual neutrino in the $0\nu\beta\beta$ decay is restricted to the volume of the nucleus, which necessitates considering states up to about $100\,\mathrm{MeV}$ [27]. Nevertheless, the expected half-life of the $0\nu\beta\beta$ decay is still higher compared to the $2\nu\beta\beta$ decay due to the requirement of helicity matching.

Of greater interest is the effective Majorana neutrino mass $\langle m_{\beta\beta}\rangle$, which can be deduced from the half-life measurement. Taking neutrino mixing into account, it is given by

$$\langle m_{\beta\beta}\rangle = \left|\sum_i U_{ei}^2 m_i\right| = \left|\sum_i |U_{ei}|^2 \eta_i m_i\right| \qquad (2.36)$$

with the mixing matrix elements U_{ei}, see section 2.1, and the corresponding mass eigenvalues m_i. The factor η_i refers to CP-phases including Dirac as well as Majorana phases. The nuclear matrix elements $M_{GT}^{0\nu}$ and $M_F^{0\nu}$ are the main uncertainty in determining $\langle m_{\beta\beta} \rangle$ from half-life measurements. Furthermore, they depend on the nuclear model parameters and calculation methods. For the nuclear model five strategies are followed. The three most popular ones are the nuclear shell model (NSM) [40], the quasi-random phase approximation (QRPA) [41] and the interaction boson approximation (IBM) [42]. In Figure 2.5 the calculated nuclear matrix elements for the five different models are
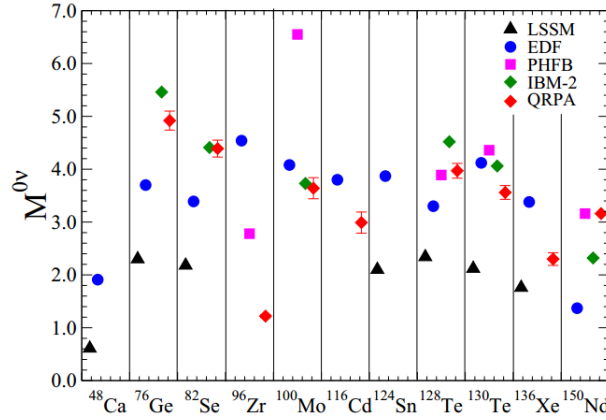
Figure 2.5: Shown are nuclear matrix elements for different ββ isotopes calculated with three different nuclear models. Large deviations between the models can be seen resulting in the main uncertainty in determining $\langle m_{\beta\beta} \rangle$. [43]

depicted showing large deviations between them.

2.2.3   The Measurement of the 0νββ decay

Typical energies for ββ decay are in the region of a few MeV distributed among the four leptons. The signals of the 2νββ decay and 0νββ decay can be clearly distinguished. While the signal of 0νββ decay is a peak in the sum spectrum of both electrons at the Q-value, a continuous spectrum is assumed for the 2νββ decay. Being a nuclear decay, the actual measured quantity is a half-life, whose value can be determined from the radioactive decay law

$$T_{\frac{1}{2}}^{0\nu} = \ln 2 \cdot M \cdot a \cdot t \cdot \frac{N_A}{N_{\beta\beta}} \qquad (2.37)$$

with the used mass M, the isotopical abundance a, the measuring time t, the Avogadro constant N_A and the number of double beta events $N_{\beta\beta}$. If no peak is observed and a constant background is expected scaling linearly with time, the 0νββ decay half-life limit can be estimated from experimental quantities [44] to be

$$T_{\frac{1}{2}}^{0\nu} \propto a\,\epsilon \sqrt{\frac{M \cdot t}{B \cdot \Delta E}}. \qquad (2.38)$$

Here, ϵ is the detection efficiency, ΔE the energy resolution and B the background rate given per kg, keV and years. With zero background the half-life measurement depends linearly on the measuring time. Thus, the sensitivity to $\langle m_{\beta\beta} \rangle$ scales with $\sqrt{Mt}$.

The quantity 2.38 is also called sensitivity to the measurable half-life and allows for comparison of existing and future experiments.

Taking the present knowledge of neutrino oscillation parameters into account, the possible scope of the effective Majorana mass $\langle m_{\beta\beta} \rangle$ can be derived in relation to the mass of the lightest mass eigenstate m_{min}, as illustrated in the left panel of Figure 2.6. The two different mass hierarchies result in different projections. Here, the normal hierarchy is shown in blue, while the inverted hierarchy is in red. The width of the innermost hatched bands corresponds to the uncertainty of the Majorana phases. Experimental errors of the oscillation parameters widen the areas additionally as shown. The two projections merge into each other for $\langle m_{\beta\beta} \rangle \geq 0.1 \, \text{eV}$ referring to the degenerate mass pattern. However, this is already disfavored by cosmology. The middle panel of Figure 2.6 shows the relation of $\langle m_{\beta\beta} \rangle$ with the summed neutrino mass $M = m_1 + m_2 + m_3$ constrained by observational cosmology. The right-hand panel depicts $\langle m_{\beta\beta} \rangle$ as a function of $m_{\nu_e} = \langle m_\beta \rangle$ determined through the analysis of beta decays. Due to the large intrinsic width of the $\beta\beta$ decay constraint, it is not possible to distinguish between both hierarchies. But if a value of $\langle m_{\beta\beta} \rangle \leq 0.01 \, \text{eV}$ is ever established, the normal hierarchy is the only option.

The next-generation experiments like GERDA in the second phase and COBRA aim for $\langle m_{\beta\beta} \rangle \approx 0.05 \, \text{eV}$. To achieve the corresponding high half-life it is important for future experiments to have an appropriately large source mass and energy resolution available accordingly to Equation 2.38. Additionally, the background rate becomes a crucial criterion and has to be reduced to a sufficiently low level. With an energy resolution of approximately $2\,\%$ at the Q-value of ^{116}Cd and a realistic exposure, this would correspond to a background rate in the order of 10^{-3} counts/kg/keV/yr.
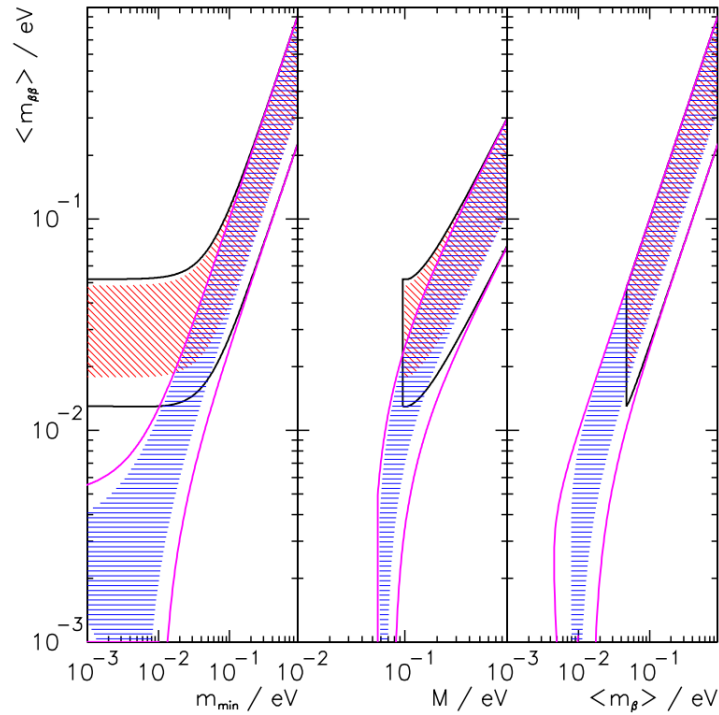
Figure 2.6: Depicted is the dependence of $\langle m_{\beta\beta} \rangle$ on various mass quantities. In the left panel the relation of $\langle m_{\beta\beta} \rangle$ to the mass of the lightest mass eigenstate m_{min} is plotted. The middle panel shows $\langle m_{\beta\beta} \rangle$ versus the summed mass $M = m_1 + m_2 + m_3$, while the right panel depicts $\langle m_{\beta\beta} \rangle$ as function of $m_{\nu_e} = \langle m_\beta \rangle$. The width of the hatched areas derives from unknown Majorana phases, while the allowed areas are given by solid lines. Here, errors of the oscillation parameters were taken into account. The two patterns correspond to the normal (in blue) and the inverted hierarchy (in red). For $\langle m_{\beta\beta} \rangle \geq 0.1 \, \text{eV}$ the two sets merge into each other referring to the degenerate hierarchy. [8]

2.3 Particle Radiation Interactions with Matter

In this section the different possible radiation interactions and the energy loss of the initial particle are discussed in general, preparing the development of a radiation shield in Chapter 4.

The potential radiation background sources can be divided into two groups discriminating their interactions with matter. The first group represents the charged particle radiations (e.g. heavy charged particles, electrons), which interact continuously through the Coulomb force in any medium. The second group contains uncharged radiation (e.g. neutrons and gamma rays), which have to undergo an interaction involving nuclei of the absorber material to radically alter the incident radiation in a single encounter. The encounters result in the full or partial energy loss of the incident radiation to electrons or nuclei causing also secondary radiation.

2.3.1   Heavy Charged Particles

Heavy charged particles, for example α particles, interact mainly with matter through Coulomb forces. Interactions with nuclei are also possible, but occur rarely [45]. Entering the absorber material, the charged particle interacts simultaneously with many electrons leaving the absorber atom behind either excited or ionized. The transferred energy comes at the expense of the charged particle and its velocity. Due to the fact, that the maximum energy that can be transferred is still a small fraction of the total energy, the primary charged particle must lose its energy in many encounters.
The linear stopping power S for charged particles is defined as the differential energy loss divided by the corresponding differential path length [45]

$$S = -\frac{dE}{dx} \tag{2.39}$$

The Bethe formula describes the energy loss and is given by [46]

$$-\frac{dE}{dx} = \frac{4\pi e^4 z^2 N Z}{m_0 v^2} \cdot \left[\ln \frac{2m_0 v^2}{I} - \ln \left(1 - \frac{v^2}{c^2} \right) - \frac{v^2}{c^2} \right] \tag{2.40}$$

with the velocity v and the charge of the primary particle ze, the electron rest mass m_0 and the electron charge e. The quantities N and Z are as previously mentioned in section 2.2 the number density and the atomic number of the material. I represents the average excitation and ionization potential of the absorber.
Comparing different charged particles of the same energy, the only factor that may change is z. Therefore, particles with greater charge will have larger energy loss. The dependence on different absorber materials relies on the electron density, the product of NZ. Thus, high atomic number, high-density materials result in the greatest linear stopping power.
The Bethe formula, Equation 2.40, fails for low particle energies. Charge exchange between primary particle and absorber material becomes more important, in which the charged particle accumulates electrons from the absorber reducing its charge and hence linear energy loss.

2.3.2   Fast Electrons

Compared to heavy charged particles, fast electrons lose their energy at a much smaller rate. Their path through absorbing matter is influenced by the orbital electron, which have the same mass and with whom the fast electrons interact. Therefore, large deviations are possible. In addition, electron-nuclear interactions can change the electron direction abruptly.
The specific energy losses due to ionization and excitation, also called collision losses,

for fast electrons is also derived by Bethe [46, 45]

$$\left(\frac{dE}{dx}\right)_c = \frac{2\pi e^4 NZ}{m_0 v^2} \cdot \left(\ln\frac{m_0 v^2 E}{2I^2(1-\beta^2)} - (\ln 2)(2\sqrt{1-\beta^2} - 1 + \beta^2)\right.$$
$$\left. + (1-\beta^2) + \frac{1}{8}(1-\sqrt{1-\beta^2})^2\right). \quad (2.41)$$

The symbols have the same meaning as in Equation 2.40 and $\beta = v/c$. Due to two reasons Equation 2.40 and 2.41 differ from each other [47]. First due to the small mass of electrons, the incident particles deflects. Furthermore, the collision takes place between two identical particles. Thus, their indistinguishability has to be taken into account. Next to collision losses, energy may be lost by radiation processes as well as by Coulomb interactions. These radiative losses are bremsstrahlung or electromagnetic radiation and are described by

$$\left(\frac{dE}{dx}\right)_r = \frac{NEZ(Z+1)e^4}{137m_0^2 c^4} \cdot \left(4\ln\frac{2E}{m_0 c^2} - \frac{4}{3}\right). \quad (2.42)$$

Radiative losses are most important for high electron energies and for absorber materials of large atomic number, which correspond to the factors E and Z in the numerator of Equation 2.42. In addition, the yield of bremsstrahlung for heavy charged particles can be neglected due to the factor m_0 in the denominator.

For electrons of interest in this thesis, mostly beta particles or secondary electrons from gamma ray interactions, typical energies are less than a few MeV. Therefore, radiative losses are a small fraction compared to collision losses and are only significant in absorber materials of high atomic number.

2.3.3 Gamma Rays

Three interaction mechanisms play an important role for gamma rays: photoelectric absorption, Compton scattering and pair production. All processes lead to the partial or complete transfer of gamma ray photon energy to electron energy. As result, the photon may disappear completely or is scattered at a significant angle, which contrasts with the charged particles previously discussed.

- **Photoelectric Absorption**

In the photoelectric absorption process a photon interacts with an absorber atom. The photon disappears completely. In its place, an energetic photoelectron is ejected by the atom from one of its bound shells. The energy of the photoelectron is given by [45]

$$E_e = h\nu - E_b \quad (2.43)$$

with the binding energy E_b. The interaction also creates an ionized absorber atom with a vacancy in one of its bound shells. This vacancy is filled through capture of a free

electron and/or rearrangement of electrons from other shells of the atom. Therefore, one or more X-ray photons may be generated as well.

The photoelectric process dominates for relatively low energy gammas. Furthermore, it is enlarged for absorber materials of high atomic number Z. A rough approximation for the probability of photoelectric absorption per atom τ is given by [45]

$$\tau \cong \text{constant} \cdot \frac{Z^n}{E_\gamma^{3.5}}. \tag{2.44}$$

The exponent n varies between 4 and 5 over the gamma energy. An analytic expression valid over all ranges of E_γ and Z does not exists.

- **Compton Scattering**

In the process of Compton scattering an incident photon interacts with an electron in the absorber material. As result, the photon is deflected through an angle θ with respect to its original direction and a portion of its energy is transferred to the electron, called the recoil electron. Since all angles are possible, the energy transferred varies from zero to a large fraction of the gamma ray energy and is given by

$$E' = \frac{E}{1 + \frac{E}{m_0 c^2}(1 - \cos\theta)} \tag{2.45}$$

with the incident photon energy E and the scattered photon energy E'. For an angle of $\theta = 180°$ the photon transfers the maximal energy resulting in a sharp cut-off in the spectrum, called Compton edge.

The probability of Compton scattering per atom of the absorber depends on the number of electrons available as scattering targets and thus increases linearly with Z.

- **Pair Production**

The process of pair production is energetically possible if the photon energy exceeds twice the rest-mass energy of an electron. The interaction must take place in the Coulomb field of a nucleus. As result, the photon disappears and is replaced by an electron-positron pair. The positron will subsequently annihilate and therefore, two annihilation photons are normally produced as secondaries in this interaction.

Since the gamma ray energy must approach several MeV, the probability of this process remains low and plays an important role for high-energy gamma rays only, but its magnitude varies approximately with the square root of the atomic number [48].

In Figure 2.7 the relative importance of the three processes is schematically depicted for different absorber materials and gamma-ray energies. The left line represents the energy at which the probabilities of photoelectric absorption τ and Compton scattering σ are equal. The right line corresponds to the same aspect for Compton scattering σ and pair production κ.
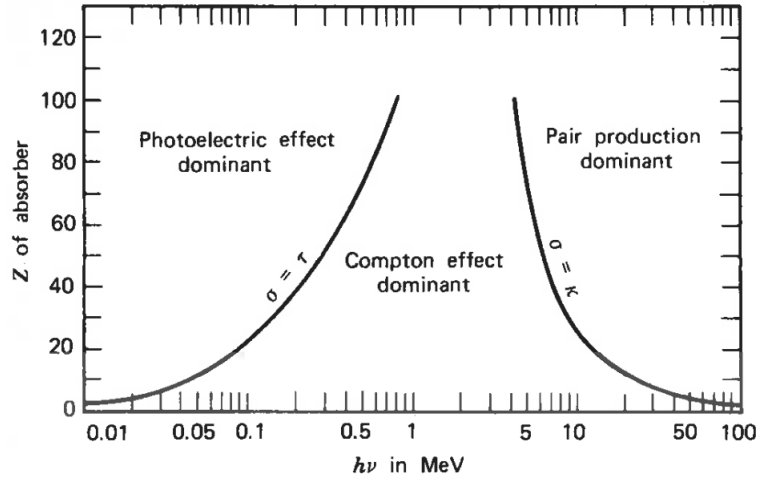
Figure 2.7: Depicted is relative importance of the three processes of gamma-ray interactions for different absorber materials and gamma-ray energies. The left line indicate the energy at which the probabilities of photoelectric absorption τ and Compton scattering σ are equal. The right line corresponds to the same aspect for Compton scattering σ and pair production κ. [45]
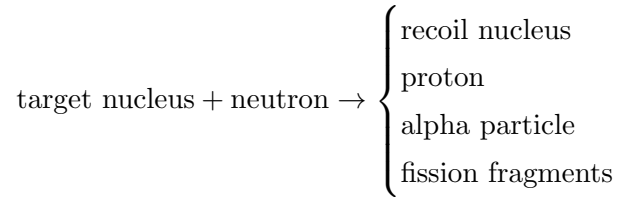
2.3.4 Neutrons

Neutrons carry no charge and thus cannot interact via the Coulomb force. Neutrons are able to penetrate many centimeters of materials without any type of interaction and can therefore be totally invisible. When a neutron undergoes an interaction, it is with a nucleus of the absorbing material resulting in either total disappearance and replacement by one or more secondary radiations or a significant alteration of energy or direction of the neutron. The secondary radiation consists almost always of heavy charged particles depending on the incident energy.

The relative probabilities of various interaction types change dramatically with neutron energy. Therefore, neutrons are divided into two categories: "fast" and "slow" neutrons. The dividing line is approximately at 0.5 eV corresponding to the cadmium cutoff, where the absorption cross section in cadmium drops abruptly [45].

The important interactions for slow neutrons are elastic scattering with absorber nuclei and neutron-induced nuclear reactions. Elastic collisions tend to be very probable, even though, due to the small kinetic energy of slow neutrons, little energy is transferred to the nucleus. However, they bring the slow neutrons into thermal equilibrium with the absorber material before other interaction types take place. Therefore, a big amount of the population of the slow neutrons refers to thermal neutrons with an energy of approximately 0.025 eV [45]. More significant for slow neutrons are neutron-induced reactions, because secondary radiation of sufficient energy to be directly detected is produced. In most materials the radiative capture reaction, (n,γ) reaction, is the most probable and plays an important role in the attenuation of neutrons.

With increasing energy the probabilities of most neutron-induced reactions drop off. Scattering becomes more important, because the neutron can transfer a sufficient amount of energy in one collision resulting in a moderation of the neutron. Secondary radiations are recoil nuclei. For even higher energies, inelastic scattering with nuclei can take place. The recoil nucleus is elevated to an excited state during the collision. The nucleus de-excites and emits a gamma ray. Possible reaction products are listed below:

$$\text{target nucleus} + \text{neutron} \rightarrow \begin{cases} \text{recoil nucleus} \\ \text{proton} \\ \text{alpha particle} \\ \text{fission fragments} \end{cases}$$

The energy loss of the neutron is greater compared to an equivalent elastic collision. Inelastic scattering and subsequently secondary gamma rays are important regarding shielding of high-energy neutrons.

2.4   Background Sources in General

Although the sensitivity to the measurable half-life, see section 2.2.3, is only inversely proportional to the square root of the background rate B, it plays an important role to increase the sensitivity, because other variables, like the source mass M or the efficiency ϵ, are mostly limited by experimental parameters or for economic reasons.

In Figure 2.8 the dependence of the sensitivity on the background rate, the energy resolution and the measuring time is shown. In comparison it can be seen, that the sensitivity is increased by a better energy resolution and lower background rate.

Even though background sources vary from experiment to experiment, they can be roughly divided into the following categories, listed in approximate order of importance [49]:

1. Environmental radioactivity

2. Radioimpurities in detector and shield material

3. Airborne radioactivity

4. Primary and secondary components of the cosmic radiation

5. Thermal neutrons

Furthermore, a sixth category has to be added, which is also crucial for $0\nu\beta\beta$ decay experiments:
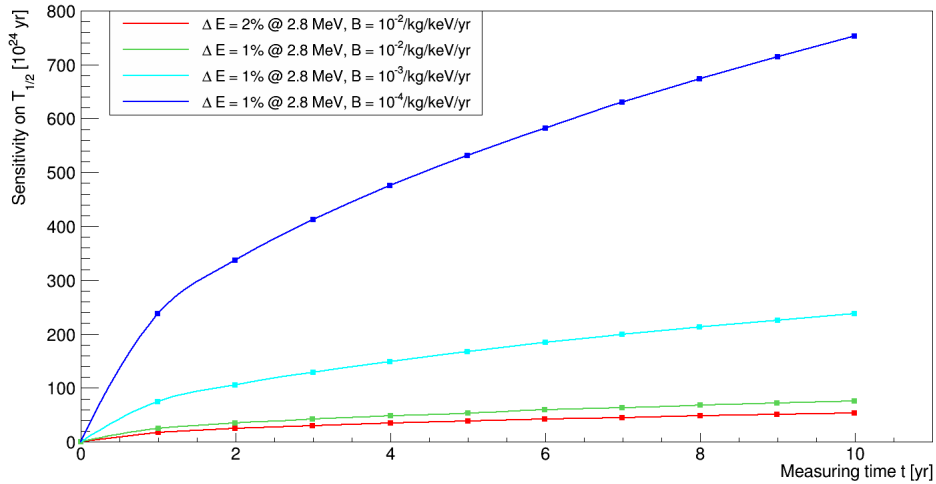
6. The $2\nu\beta\beta$ decay

Figure 2.8: Depicted is dependence of the sensitivity on the background rate, the energy resolution and the measuring time. A better energy resolution and/or a lower background rate lead to a higher sensitivity.

In general, background reduction is only meaningful in context. The degree of radiopurity is crucial to the level that has to be achieved in other parts. In addition, interrelations exist. The thickness of a shield against gamma radiation influences the cosmic ray-induced background. To achieve a certain background rate and hence for building a shield, such aspects have to be kept in mind.

2.4.1 Environmental Radioactivity

Radionuclides in the environment can be sorted generally into three types: primordial, cosmogenic and man-made.

The primordial category includes the Uranium series, the Thorium series and ^{40}K. Most γ radiation originates from these sources. The integrated γ flux at sea level is typically 10 photons $cm^{-2}s^{-1}$ [49] for energies over 50 keV and at 1 m above ground. In contrast, the cosmic ray photon flux density contributes only with a small fraction below 1 % [49]. At LNGS[10] the photon flux was measured with NaI(Tl) detectors at different sites of the underground laboratory and determined to 0.3–0.4 $cm^{-2}s^{-1}$ [50].

In general, the uranium series begins with naturally occurring ^{238}U (natural abundance: 99.27 %), followed by thorium, protactinium, radium, radon, polonium, astatine, lead, bismuth and thallium and ends with ^{206}Pb. Next to gamma rays also alpha and beta rays are emitted. In Table 2.1 the uranium series is summarized. The thorium series, see Table 2.2, begins with naturally occurring ^{232}Th (natural abundance: 100 %) and terminates with ^{208}Pb. The series includes the following elements: actinium, radium, radon, lead, bismuth and polonium. like the uranium series, the emitted radiation is

---

[10]LNGS: Laboratori Nazionali del Gran Sasso, underground laboratory, Italy

also a mixture of alpha, beta and gamma rays. All other decay series can be neglected [49]. A mathematical model describing abundances and activities in a decay chain as a function of time is given by the Bateman equation [51]

$$N_n(t) = \prod_{j=1}^{n-1} \lambda_j \sum_{i=1}^{n} \sum_{j=1}^{n} \left(\frac{N_i(0)e^{-\lambda_j t}}{\prod_{p=1,p\neq j}^{n}(\lambda_p - \lambda_j)} \right) \tag{2.46}$$

with the decay constant λ depending on decay rates and initial abundances. Secular equilibrium in the decay chains, in which the half-life of the daughter radionuclide is negligible compared to the half-life of the parent radionuclide, is rarely achieved in most surface and near-surface environments due to migration of nuclei. Especially, radon, a member of both decay series, is able to escape from solids either by recoil or by diffusion and is further discussed in section 2.4.3.

The nuclide ^{40}K is not part of a decay series. Natural potassium contains $0.012\,\%$ ^{40}K, which decays to ^{40}Ca emitting a beta particle with $1.311\,$MeV endpoint energy ($89\,\%$) or to ^{40}Ar emitting a gamma ray of $1.46\,$MeV ($11\,\%$) and characteristic Ar X-rays.

Next to the already mentioned isotopes, ^{235}U was added to the possible list of background sources due to activity measurements of the analyzed detector parts in Chapter 5, although it is the third natural decay chain and could be neglected. ^{235}U decays with a half-life of $7.038\cdot10^8$ years to ^{231}Th emitting an alpha particle with an energy of $4.494\,$MeV. Natural uranium contains $0.72\,\%$ ^{235}U.

Next to primordials, cosmogenic nuclides exist, but the total activity is only in the per mill range of the primordial activity [49]. Therefore, they are only important if the detector material itself consists of cosmogenic nuclides or is activated.

In contrast, background from fission-product activities that originate from past weapons testing are also important to consider. The most prominent contributor is ^{137}Cs, which can be found as trace in construction materials of the laboratory and shielding materials or other structures. With a half-life of 30.07 years, ^{137}Cs decays emitting beta rays with an energy of $1.176\,$MeV ($5.4\,\%$) to ^{137}Ba or with an energy of $0.512\,$MeV ($94.6\,\%$) to the metastable isotope ^{137m}Ba. Natural occurring cesium consists to $100\,\%$ of the stable isotope ^{133}Cs. Furthermore, ^{85}Kr is released by nuclear power plants resulting in constant increase in the atmosphere. It decays emitting a beta particle of $0.687\,$MeV with a half-life of 3934.4 days. Due to its absence in activity measurements of different detector parts in Chapter 5 it is neglected.

Table 2.1: Tabulated is the uranium series with the half-life of each isotope, the branching
ratio and the energy of emitted α-, β- and γ rays. [52]

half-life	isotopes decay branch [%]	α-decay energy [MeV] (branch [%])	β-decay energy [MeV] (branch [%])	γ-decay energy [keV] (emiss. prob. [%])
$4.468\cdot 10^9$ y	$^{238}_{92}$U	α: 4.197 (77)		
	$100 \downarrow \alpha$	α: 4.147 (23)		γ: 49.55 (0.062)
24.1 d	$^{234}_{90}$Th		β: 0.199 (72.5)	γ: 92.37 (2.42)
	$100 \downarrow \beta$		β: 0.104 (17.8)	γ: 63.28 (4.1)
			β: 0.060 (7.1)	γ: 92.79 (2.39)
1.175 m	$^{234m}_{91}$Pa		β: 2.29 (98.4)	
	$100 \downarrow \beta$		β: 1.53 (0.62)	γ: 766.37 (0.316)
			β: 1.25 (0.74)	γ: 1001.03 (0.839)
$2.45\cdot 10^5$ y	$^{234}_{92}$U	α: 4.775 (72.5)		
	$100 \downarrow \alpha$	α: 4.723 (27.5)		γ: 53.20 (0.123)
$7.538\cdot 10^4$ y	$^{230}_{90}$Th	α: 4.688 (76.3)		
	$100 \downarrow \alpha$	α: 4.621 (23.4)		γ: 67.67 (0.38)
1600 y	$^{226}_{88}$Ra	α: 4.784 (94.5)		
	$100 \downarrow \alpha$	α: 4.601 (5.55)		γ: 186.10 (3.51)*
3.8235 d	$^{222}_{86}$Rn	α: 5.490 (99.9)		
	$100 \downarrow \alpha$	α: 4.987 (0.08)		
3.05 m	$^{218}_{84}$Po	α: 6.002 (100)		
	0.018 99.98			
	$\beta \swarrow \searrow \alpha$			
∼2 s	$^{218}_{85}$At $^{214}_{82}$Pb		β: 0.73 (40.5)	γ: 295.21 (18.15)
26.8 m	$\alpha \searrow \swarrow \beta$			γ: 241.98 (7.12)*
			β: 0.67 (46)	γ: 351.92 (35.1)
19.9 m	$^{214}_{83}$Bi		β: 3.275 (19.9)	γ: 609.32 (44.6)*
	0.021 99.979		β: 1.88 (7.18)	γ: 768.36 (4.76)*
	$\alpha \swarrow \searrow \beta$		β: (17.5)	γ: 1120.29 (14.7)*
			β: (8.26)	γ: 1238.11 (5.78)*
			β: 1.51 (16.9)	γ: 1764.49 (15.1)*
			β: 1.02 (16.9)	γ: 2204.21 (4.98)*
1.3 m	$^{210}_{81}$Tl $^{214}_{84}$Po	α: 7.687 (100)		
164.3 μs	$\beta \searrow \swarrow \alpha$			
22.3 y	$^{210}_{82}$Pb		β: 0.063 (19)	
	$\sim100 \downarrow \beta$		β: 0.017 (81)	γ: 46.54 (4.24)
5.013 d	$^{210}_{83}$Bi		β: 1.161 (99)	
	$\sim100 \downarrow \beta$			
138.4 d	$^{210}_{84}$Po	α: 5.305 (99)		
	$100 \downarrow \alpha$			
stable	$^{206}_{82}$Pb			

Table 2.2: Tabulated is the thorium series with the half-life of each isotope, the branching ratio and the energy of emitted α-, β- and γ rays. [52]

half-life	isotopes decay branch [%]	α-decay energy [MeV] (branch [%])	β-decay energy [MeV] (branch [%])	γ-decay energy [keV] (emiss. prob. [%])
	$^{232}_{90}$**Th**			
$1.405 \cdot 10^{10}$ y	$100 \downarrow \alpha$	α: 4.012 (77.9)		
		α: 3.954 (22.1)		γ: 63.81 (0.27)
	$^{228}_{88}$**Ra**			
5.75 y	$100 \downarrow \beta$		β: 0.039 (60)	
			β: 0.015 (40)	
	$^{228}_{89}$**Ac**			
6.15 h	$100 \downarrow \beta$		β: 2.18 (10)	γ: 338.32 (11.3)
			β: 1.70 (11.6)	γ: 968.97 (16.2)*
			β: 1.11 (31.0)	γ: 911.21 (26.6)*
	$^{228}_{90}$**Th**			
1.9131 y	$100 \downarrow \alpha$	α: 5.423 (71.1)		
		α: 5.340 (28.2)		γ: 84.37 (1.22)
		α: 5.221 (0.44)		γ: 215.99 (0.28)
	$^{224}_{88}$**Ra**			
3.664 d	$100 \downarrow \alpha$	α: 5.685 (94.9)		
		α: 5.449 (5.1)		γ: 240.99 (4.1)
	$^{220}_{86}$**Rn**			
55.6 s	$100 \downarrow \alpha$	α: 6.288 (99.9)		
		α: 5.747 (0.11)		γ: 549.73 (0.11)
	$^{216}_{84}$**Po**			
0.145 s	$100 \downarrow \alpha$	α: 6.778 (100)		
	$^{212}_{82}$**Pb**			
10.64 h	$100 \downarrow \beta$		β: 0.569 (12)	γ: 300.09 (3.25)
			β: 0.331 (83)	γ: 238.63 (43.5)
			β: 0.159 (5)	
	$^{212}_{83}$**Bi**			
60.55 m	35.94 64.06			
	$\alpha \swarrow \searrow \beta$	α: 6.089 (27.1)	β: 2.248 (86.6)	γ: 1620.74 (1.5)*
		α: 6.050 (69.9)	β: 1.521 (6.8)	γ: 727.33 (6.7)
	$^{208}_{81}$**Tl** $^{212}_{84}$**Po**			
3.053 m	$\beta \searrow \swarrow \alpha$	α: 8.785 (100)		
0.298 μs			β: 1.80 (51)	γ: 583.19 (30.6)*
			β: 1.52 (21.7)	γ: 860.56 (4.5)*
			β: 1.29 (22.8)	γ: 511.77 (8.2)
			β: 1.52 (3.1)	γ: 2614.53 (35.8)*

2.4.2 Radioimpurities in Detector and Shield Material

The existence of primordial radionuclides in ores and other materials results in a contamination in the final products needed as detector or shielding material. With some exceptions, the main radioactivity originates from the uranium and thorium decay series and potassium, as mentioned in the previous section.

It is possible to separate copper from practically all radionuclides in the environment, since it is purified after smelting by electrolytic dissolution and redeposition in the solution. The purification of other metals, like lead, is usually much more difficult, because the formation of a slag is involved in the smelting process. The slag takes up lithophile elements including mineral-forming elements Si, Al and O, as well as alkali and earth-alkali elements and most transition elements. Hence, potassium and nuclides from the decay series are concentrated in the slag. Therefore, special chemical separation processes have to be applied. In contrast, the main contamination of plastic materials is ^{14}C, since they consists generally of C, H and O. Nevertheless, possible contamination may derive from additives or mechanical engineering of hard plastics.

The COBRA detector material CdZnTe was measured determining upper limits of radioimpurities. Although it is said that CdZnTe can be produced radiopure, it is further investigated in Chapter 5.

2.4.3 Airborne Radioactivity

Traces of radioactive gases or dust particles in the ambient air also contribute to the background. Radon ^{222}Rn and ^{220}Rn are short-lived radioactive gases originating from the decay chains of uranium and thorium present in the soil or construction materials. As already mentioned, radon can migrate and hence escape materials disturbing the equilibrium in the materials itself. Because of a shorter half-life of ^{220}Rn (55.6 s) its concentration in air is normally below ^{222}Rn, although its activity is often the same or higher in rocks, soil and building materials. Therefore, ^{222}Rn is the strongest source of airborne radioactivity. Its concentration in laboratories is of about $40\,\mathrm{Bq/m^3}$ on average [49].

The ^{220}Rn family dies out rather quickly with the longest half-life of 10.64 h of the progeny ^{212}Pb. In contrast, ^{222}Rn feeds into ^{210}Pb with a half-life of 22.3 years. However, the last γ-active progeny of ^{222}Rn is ^{214}Bi with a half-life of 19.9 min. Therefore, at least the γ activity of the ^{222}Rn family dies out rather quickly within an hour.

The direct Rn progeny are originally positively charged [49] and thus, can be attracted by bias supply, e.g. high voltage (HV). The deposition of radon progeny on surfaces is called play-out effect [49] and is strongly enhanced on statically charged surfaces such as plastics. Here, the most important isotopes are the progeny of ^{210}Pb, ^{210}Bi and ^{210}Po.

2.4.4   Cosmic Ray-induced Background

Primary cosmic ray particles enclose mainly protons (90 %), α particles (9 %) and heavier particles (1 %). They hit the atmosphere with a rate of about 1000 counts/m^{2}s [49]. After their interaction with atmospheric nuclei, a variety of other particles is produced, in particular neutrons, electrons, neutrinos, protons, muons and pions. The maximum of the total intensity of these secondaries is at an altitude of 14 km [49]. After that, the intensity drops gradually, with the nucleons experiencing the sharpest decline. At ground level, most particles are muons (75 %) followed by pions, protons, neutrons, electrons and gamma rays.

In underground experiments, like COBRA, only muons and neutrons are relevant particles, since electrons and gammas are directly absorbed by the rock or by e.g. lead, if produced in the shield. The hadronic component is negligible in underground laboratories, but contributes to the production of cosmogenic nuclei on the surface. Thus, different background sources originating from cosmic rays are discussed in the following sections.

Muon-induced Background

In general, muons do not contribute as a serious background, since they can be identified and vetoed as they pass through the detector. Still, muon-induced backgrounds are important. At shallow sites, where the muon rate is rather high, the muon veto rate contributes to the experiment's dead time. In addition, low-energy muons can undergo nuclear capture producing neutrons and unwanted radioactive isotopes, which is discussed in the next section.

High-energy muons create spallation products, e.g. neutrons, photons and radioisotopes. Produced in the surrounding rock, in the local shield or in the detector itself, secondary neutrons are not easily tagged. Especially neutrons produced in the rock are not necessarily in time coincidence with a muon veto. These neutrons may represent a fundamental limiting background that only deeper sites can reduce sufficiently.

The LNGS laboratory has a depth of 1400 m corresponding to 3800 m w.e.[11], which is rather deep and the muon flux is suppressed by a factor of 10^6 compared to sea level.

Radioisotope Production

Secondary cosmic ray particles generate background also indirectly through the production of radioactive nuclei. In particular at ground level or during air transportation, the activation by the hadronic component can reach specific radioactivity levels higher than the contamination from primordial nuclides and thus dominates the background at the beginning of the underground operating. Therefore, avoiding the transport in air of

---

[11]w.e.: Abbreviation for "water equivalent"

the most sensitive components is often worthwhile. In addition, a common practice is keeping materials exposed at the surface underground for several months or even years before usage to eliminate short-lived cosmogenic activities, because even shallow depths reduce the cosmic ray nucleon rate by several orders of magnitude. But also at deeper sites cosmogenic radionuclides are produced.

Neutron-induced Background

At depths greater than a few tens of meters, neutrons are mainly produced by radioactive processes. Nevertheless, the spectrum from spallation is much harder up to several GeV in neutron energy. Cosmic ray muons produce neutrons through several different mechanisms depending on energies and depths [53]. The most important channels are inelastic scattering and radioactive capture. However, contributing processes are the following [53]:

1. **Negative muon capture on nuclei**
   Negative muons with sufficiently low energy can be attracted into the Coulomb field of a nucleus, forming a "muonic atom" bound state. The bound muon can either decay ($\mu^- \to e^- + \overline{\nu}_e + \nu_\mu$) or else undergo a nuclear capture via the weak charged-current process:

 $$\mu^- + A(Z, N) \to \nu_\mu + A(Z - 1, N + 1). \tag{2.47}$$
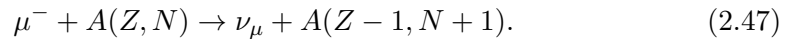
2. **Electromagnetic showers generated by muons**
   Photons and electrons from bremsstrahlung and pair production are released, while muons pass through matter producing a particle shower. The contribution from such processes is small, depending on $< Z^2 >$ and thus become more important for high-Z targets, e.g. lead.

3. **Muon interactions with nuclei via exchange of virtual photons**
   As a muon passes through matter, it can produce neutrons through deep-inelastic scattering involving a virtual photon.

   $$\mu + \text{nucleus} \to \mu + \text{nucleus}^* + n \tag{2.48}$$
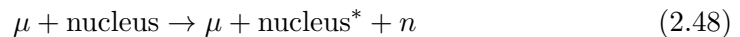
   It is one of the least understood processes in muon interactions at high energies.

4. **Muon-nucleon quasielastic scattering**
   For completeness, the contribution of neutron production from neutron knockout by muon-nucleus quasielastic scattering has to be kept in mind.

5. **Secondary neutron production from any of the above processes**

In general, the intensity of the muon-induced neutrons decreases slower with greater depth as the intensity of muons itself, because of induced particle showers. Thus, the

intensity of the muon-induced neutrons depends on the average muon energy $< E_\mu >$ at the corresponding depth [54]:

$$N_n(h) \propto \langle E_\mu(h) \rangle^{0.75}. \tag{2.49}$$

Although the measurement of the neutron flux is complicated due to its low intensity, different groups measured the flux with different methods at the LNGS. Two measurements offer information about the spectrum of the neutron flux. The results are summarized in Table 2.3.

Table 2.3: Tabulated is the measured neutron flux at the LNGS from two different groups and different detection methods.[55, 56]. With increasing energy the neutron flux drops off.

Energy	Neutron flux [55] $[10^{-6}\text{cm}^{-2}\text{s}^{-1}]$	Energy	Neutron flux [56] $[10^{-6}\text{cm}^{-2}\text{s}^{-1}]$
$(0-50)\,\text{meV}$	1.08 ± 0.02		
$50\,\text{meV} - 1\,\text{keV}$	1.84 ± 0.20		
$1\,\text{keV} - 2.5\,\text{MeV}$	0.54 ± 0.01	$(1-2.5)\,\text{MeV}$	0.14 ± 0.12
$(2.5-5)\,\text{MeV}$	0.27 ± 0.14	$(2.5-5)\,\text{MeV}$	0.13 ± 0.04
$(5-10)\,\text{MeV}$	0.05 ± 0.01	$(5-10)\,\text{MeV}$	0.15 ± 0.04
$(10-15)\,\text{MeV}$	$(0.6 \pm 0.2) \cdot 10^{-3}$	$(10-15)\,\text{MeV}$	$(0.4 \pm 0.4) \cdot 10^{-3}$
$(15-25)\,\text{MeV}$	$(0.5 \pm 3.0) \cdot 10^{-6}$		

In addition, the production rate of muon-induced neutrons was determined by different groups for different underground laboratories. The LVD collaboration calculated the rate for the LNGS resulting in an averaged number of muon-induced neutrons of [57]:

$$\langle N \rangle = (1.5 \pm 0.4) \cdot 10^{-4} \, \frac{\text{neutrons}}{\text{muon} \cdot \text{g} \cdot \text{cm}^2}. \tag{2.50}$$

Compared to the result of the LSD detector, this number is significantly smaller [58]:

$$\langle N \rangle = (5.3^{+0.95}_{-1.02}) \cdot 10^{-4} \, \frac{\text{neutrons}}{\text{muon} \cdot \text{g} \cdot \text{cm}^2}. \tag{2.51}$$

The difference was not clarified so far, but cannot be explained by different depth, nor large systematic errors [57].

2.4.5   Thermal Neutrons

The neutron flux originating from thermal neutrons dominates the activation processes and neutron scattering events underground. Additionally, the intensity of this neutron source is depth-independent, because thermal neutrons originate from either (α,n)-reactions or moderation after spontaneous fission (SFN).

The primordial alpha emitters produce secondary neutrons mainly through (α,n) reactions from alpha decays in the uranium and thorium chains. In addition, all thorium and uranium isotopes are able to undergo spontaneous fission in nature, emitting two or three neutrons, instead of the predominant α decay. In particular, ^{238}U has to be considered, because the fission half-life is with $4.468 \cdot 10^9$ years smaller compared to other nuclides, like ^{235}U and ^{232}Th. Nevertheless, the dominant production mechanism are (α,n) reactions, since the fission-to-alpha branching ratio is often much smaller than the (α,n) probability. The branch ratio for ^{238}U for the spontaneous fission decay mode is 0.00005 %.

2.4.6   The $2\nu\beta\beta$ decay

Despite all discussed background sources, the $0\nu\beta\beta$ decay is always accompanied by the $2\nu\beta\beta$ decay leading to a projection of $2\nu\beta\beta$ decay events in the peak region of $0\nu\beta\beta$ decay. The fraction F of $2\nu\beta\beta$ events in the peak region can be calculated by [59, 60]

$$F = \frac{8Q}{m_e} \left(\frac{\Delta E}{Q} \right)^6 \qquad (2.52)$$

This background cannot be removed, but with a sufficiently good energy resolution both decays can be discriminated, which is also discussed in Chapter 5.

2.5   Monte Carlo Simulations in General

Monte Carlo (MC) simulations are methods relying on repeated random sampling to gain numerical results. They are used by experiments to obtain information about important parameters, which cannot be measured directly, e.g. the efficiency. Analytical calculations are often also not possible due to the complexity of the underlying physics processes. For the description of one problem (e.g. passage of a neutron through a slab of material) the individual likely events comprising the problem are simulated sequentially banking temporarily generated secondary particles. The probability distributions governing these events are statistically sampled to describe the total problem by taking also into account the rules concerning individual processes and materials. In general, the number of trials necessary to adequately describe a problem is usually large. The statistical sampling process is based on the selection of random numbers.

2.5.1   Geant4 and VENOM

The COBRA experiment uses the simulation package VENOM, which was developed by the collaboration. It is based on the Geant4 [61, 62] simulation framework for MC

simulations of the passage and transport through matter. Both are object-orientated written in C++. Geant4 is a simulation toolkit, which already offers models and cross sections for various interactions of particles with matter and additionally provides methods for tracking, geometry, hits, etc. VENOM uses these methods and models. Furthermore, it provides the choice of the appropriate interaction method, initialization of parameters, data output and geometry definitions.

Since the Geant4 9.3 version, VENOM applied the physics list of the Geant4 underground physics example (DMXPhysicsList), which included the Livermore package for low-energy electromagnetic processes down to particle energies of 250 meV [63]. In the Geant4 9.4 version, the modular physics list Shielding [64] was introduced and is recommended for underground physics by the Geant4 collaboration. It uses the Fritiof string model (FTF) [65, 66] and the Bertini cascade (BERT) [67] for the high and low energies up to 5 GeV ranges for proton, neutron, pion and kaon interactions. It can be compared to the FTFP_BERT reference list [68], but uses different neutron cross-section data: JENDL/HE-2007 [69, 70] up to 3 GeV and evaluated cross-sections above 3 GeV. Neutron interactions below 20 MeV are described by high-precision data-driven models with data obtained from the ENDF/B-VII library [71]. Furthermore, thermal scattering off chemically bound atoms was added for neutron energies below 4 eV. This is important in particular for model thermalisation in plastics [72]. For electromagnetic processes the standard physics packages [73, 74] provided by Geant4 are implemented. Their validity range of electromagnetic models is from 1 keV to 10 PeV. Both physics lists were tested and used for the MC simulations in Chapter 4 and 5. The currently used Geant4 version is 9.6p02.

VENOM offers two different possibilities for the definition of the simulated setup geometry including the definition of materials and the construction of individual volumes composing the physical geometry. The first option is to define the MC geometry in the source code of VENOM by the user, which has several disadvantages [75]. Therefore, an alternative was implemented using GDML[12] [76]. GDML is based on the XML document structure rules and is developed at CERN[13] like Geant4. Thus, both are fully compatible. All used MC geometries in Chapter 4 and 5 were generated with GDML.

Monte Carlo Simulation Cuts

Cuts are used in MC simulations to restrict the length of a track analyzed in the MC saving CPU time and memory. A cut can refer to a actual length, but also to an energy or time limit.

With the DMXPhysicsList the following cuts were used. The default cut value was set

---

[12]GDML: Geometry Description Markup Language
[13]CERN: Conseil Européen pour la Recherche Nucléaire. Switzerland

to 1 μm affecting gammas and positron interactions. For electrons the cut was decreased to 10 nm. Regarding neutrons an energy limit was set to 250 eV corresponding to the validity range of the Livermore package.

In contrast, the Shielding reference list uses only one default cut, which is fixed to 0.7 mm.

2.5.2   Precision and Accuracy of Monte Carlo Results

MC results represent an average of the contributions from many histories sampled during the course of the problem assigning a score x_i to each random walk. Typically a range of scores will be produced depending on the selected recorded aspect and chosen variance reduction techniques. The true answer is the expected value of x, $E(x)$, given by

$$E(x) = \int x f(x) dx \qquad (2.53)$$

with $f(x)$ is the seldom known history score probability density function [77]. By MC random walks $f(x)$ is implicitly sampled and the true answer can be estimated by

$$\overline{x} = \frac{1}{N} \sum_N x_i. \qquad (2.54)$$

If N approaches infinity, $\overline{x}$ tends to the limit $E(x)$. The variance S can be estimated by MC as well, leading to

$$S^2 = \frac{\sum_N (x_i - \overline{x})}{N - 1} \approx \overline{x^2} - \overline{x}^2 \qquad (2.55)$$

with

$$\overline{x^2} = \frac{1}{N} \sum_N x_i^2 \qquad (2.56)$$

for large N [77]. The estimated variance of $\overline{x}$ is given by [77]

$$S_{\overline{x}}^2 = \frac{S^2}{N}. \qquad (2.57)$$

The Equations 2.53 - 2.57 do not depend on any restriction on the distribution, beyond requiring that $E(x)$ exists and is finite. Furthermore, it is important to note that $S_{\overline{x}}$ is proportional to $1/\sqrt{N}$, which is a drawback to the MC method.

Regarding precision and accuracy of MC, there is a extremely important difference. Precision is the uncertainty in $\overline{x}$ caused by the statistical fluctuations of the x_i. In contrast, accuracy is a measure of how close the expected value $E(x)$ is to the true physical quantity. This aspect is schematically depicted in Figure 2.9. The difference between $E(x)$ and the true value is called systematic error, which is seldom known.
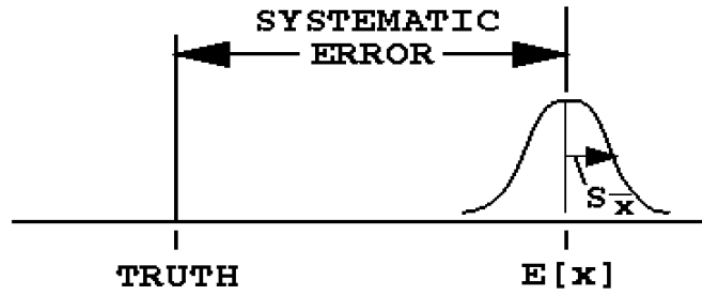
Figure 2.9: Schematically depicted is the difference of the precision and the accuracy of a MC
result. Precision is the uncertainty in $\overline{x}$ caused by the statistical fluctuations of
the x_i. In contrast, accuracy is a measure of how close the expected value $E(x)$ is
to the true physical quantity, which is called systematic error [77].

Therefore, uncertainty refers only to the precision of the MC result and not to the
accuracy.

There are three factors affecting the accuracy of a MC result and additionally four
user-controlled factors regarding the precision [77]:

- **The Code**
  Inaccuracies originating from the code encompass all physics features including
  used calculations as well as mathematical methods. In addition, there can be un-
  certainties in the data, e.g. transport and reaction cross sections or other constants
  and in the quality of the differential cross section in energy and angle. Further-
  more, coding errors can always be a problem, but GEANT4 is a mature and heavily
  used simulation tool. Therefore, a serious coding error should be diminished.

- **Problem Modeling**
  Further inaccuracies arise from an inappropriate model of energy and angular
  distribution of the radiation source. Additionally, the geometrical description and
  the physical characteristics of the used materials are modeling factors.

- **The User**
  Regarding the accuracy, user errors involving the problem input or subroutines
  are the main issues, followed by the abuse of variance reduction techniques. Fur-
  thermore, the precision is affected by the following user-controlled choices. First,
  the choice of forward vs. adjoined calculation depends on the relative sizes of
  the source and detector regions. Forward calculations transport particles from
  source to detector whereas in adjoined calculations the particles are transported
  backwards from detector to source. In this work forward calculations are used,
  because they are preferable if the detector is larger and the source region is small.
  In addition, the detector size is important. Hence, lower-dimensional detectors are
  easier to estimate than larger ones. At least, the number of simulated particles
  will improve the precision, because the precision is proportional to $1/\sqrt{N}$.

Chapter 3

The COBRA Experiment

3.1 The Concept of COBRA

The aim of the next-generation experiment COBRA[1] [78] is to prove the existence of
the $0\nu\beta\beta$ decay and to measure its half-life by using cadmium zinc telluride (CdZnTe)
semiconductor detectors.

The concept for a large scale setup consists of a three dimensional array of CdZnTe detectors with a total mass of several hundred kg enriched in ^{116}Cd up to $90\,\%$. CdZnTe contains nine double beta candidates, some of them being β^+ emitters, listed in Table 3.1.

Table 3.1: Tabulated are $\beta\beta$ isotopes in CdZnTe with their decay mode, Q-value and natural
abundance. The most interesting isotopes for COBRA are ^{116}Cd (high Q-value),
^{130}Te (high nat. abundance) and ^{106}Cd (high Q-value, $2\beta^+$ emitter). [78, 79]

Isotope	Decay Mode	Q-value [keV]	nat. Abundance [%]
^{70}Zn	$2\beta^-$	1001	0.62
^{114}Cd	$2\beta^-$	534	28.7
^{116}Cd	$2\beta^-$	2814	7.5
^{128}Te	$2\beta^-$	868	31.7
^{130}Te	$2\beta^-$	2527	33.8
^{106}Cd	$2\beta^+ - \beta^+/EC - EC/EC$	2771	1.21
^{64}Zn	$\beta^+/EC - EC/EC$	1096	48.6
^{120}Te	$\beta^+/EC - EC/EC$	1722	0.1
^{108}Cd	EC/EC	231	0.9

The detector material provides its own source, allowing for high masses and a high
detection efficiency. In addition, CdZnTe has important advantages. The material is

---

[1]COBRA: CdZnTe $0\nu\beta\beta$ Research Apparatus, Italy

radiopure, can be operated at room temperature and still provides an excellent energy resolution of a few percent. Furthermore, due to the industrial development of CdZnTe detectors, it is a mature technology and comparatively inexpensive. In Figure 3.1 the CdZnTe detectors are illustrated in two different sizes. The smaller one has a size of $1\,cm^3$ and is operated in the demonstrator setup, while the larger ones are of a size of $6\,cm^3$ and are discussed for a large scale setup.
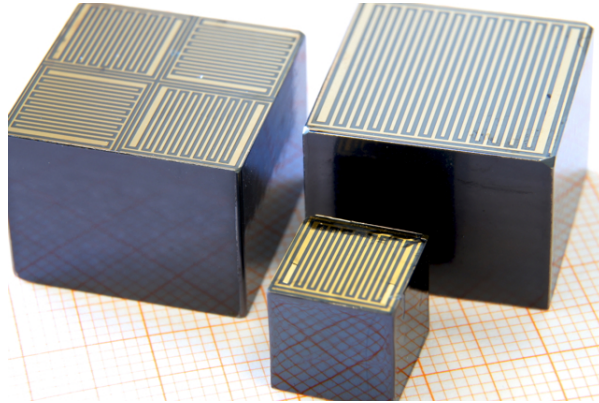

Figure 3.1: Depicted are CdZnTe detectors in two different sizes ($1\,cm^3$ and $6\,cm^3$). The smaller one is operated in the demonstrator setup, while the larger ones are investigated for a large scale setup. Furthermore, two different electrode designs are considered. [80]

As ^{116}Cd has a high Q-value ($2814\,keV$), a good matrix element and a large phase space it is certainly the most interesting isotope for COBRA. The high Q-value is well above the prominent full-energy peak of the ^{208}Tl γ-line ($2615\,keV$), which is an advantage concerning the background level. A drawback of ^{116}Cd is its low $2\nu\beta\beta$ decay half-life in the order of 10^{19} years leading to the necessity of a very good energy resolution to disentangle the $2\nu\beta\beta$ and $0\nu\beta\beta$ decay. In addition, the detection sensitivity for decays of other double beta isotopes with smaller Q-value, e.g. ^{130}Te, is limited.

Next to ^{116}Cd, ^{130}Te with a high natural abundance and ^{106}Cd, which also has a high Q-value, are interesting. Even though the Q-value of ^{130}Te is not above the ^{208}Tl γ-line, it is between the full-energy peak and the Compton edge of this line, which is helpful to reduce the γ-background. Additionally to its high natural abundance, the half-life of the $2\nu\beta\beta$ decay half-life is high. Therefore, expensive isotope enrichment will be cheaper and due to the high $2\nu\beta\beta$ decay half-life in the order of 10^{21} years, less $2\nu\beta\beta$ decay background will be detected in the $0\nu\beta\beta$ decay signal region.

^{106}Cd is one of the most promising candidates for $0\nu\beta^+\beta^+$ decay. The Q-value is relatively large, but the phase space is reduced, because the energy is decreased by $4\cdot m_e$ due to the emission of two positrons, see section 2.2.1. Nevertheless, with the planned array of several thousand of CdZnTe detectors, it is possible for a coincidence analysis, which focuses on the detection of simultaneous signals in more than one detector. The very distinctive signature of this decay in form of four gamma lines at $511\,keV$ can

therefore be detected. The β^+/EC decay mode is interesting in particular, because of a possible contribution of a right handed current, the second most popular decay mechanism for $0\nu\beta\beta$ decay after the mass driven mechanism [39].

3.2 CPG Detector Technology

Within the R&D program, two different detector technologies are investigated. These are coplanar grid detectors (CPG) and pixelated detectors. The efforts referring to the investigation of pixelated detectors are not considered in this thesis, but are discussed in [81].

The CPG technology [82] was developed for CdZnTe to counteract the missing hole signal at the cathode of the detector. Due to a smaller drift velocity compared to the electrons and the presence of high concentrations of hole-trapping defects, the hole signal is mostly lost during data acquisition (DAQ). This problem can be solved by an anode which is structured into two comb-shaped parts isolated from each other emulating the function of a Frisch grid [83], which is commonly employed in gas and liquid ionization detectors. The two parts of the anode are on a slightly different potential and are read out separately. The amplitudes of the two pulses form the basis of event reconstruction. The opposite side of the CPG is a uniform cathode. In Figure 3.1 the two comb-shaped parts of the anode can be seen. For the bigger detectors two different electrode layouts are investigated.

In operation a high-voltage ($\sim 1\,\mathrm{kV}$) is applied between the cathode and one anode, while a bias (~ 50–$100\,\mathrm{V}$) is applied between the anodes. With such a readout approach, high masses with only a small number of readout channels are possible. Near to the ROI[2] at the Q-value of ^{116}Cd energy resolutions better than $2\,\%$ FWHM at $2615\,\mathrm{keV}$ with cost efficient low resolution detectors were achieved.

The anode held at higher potential is called collecting anode (CA), while the other anode refers to the non-collecting anode (NCA). Electrons, which were excited into the conduction band by a particle interaction in the bulk of the detector, drift straight towards the anode plane until they get close to the anode grid rails. Here, they are diverted by the near-anode field and collected in the CA. The proper treatment of the design principle follows the Shockley-Ramo theorem [84] and begins with the calculation of the weighting potentials. In Figure 3.2 the weighting potential of the CA and NCA was calculated along a plane through the center of the detector. The two weighting potentials are nearly equal at most locations in the detector and arise with a slope of 1/2 between the cathode and the anode plane. The CA and NCA weighting potentials are 1 and 0 respectively, by definition, at the CA rail. These properties of the weighting potential allow for a difference signal based on the raw CA and NCA signals, that is proportional to the charge from ionization and independent of the interaction depth. Following the Shockley-Ramo theorem the raw CA Δq_{CA} and NCA signal Δq_{NCA} are

---

[2]ROI: region of interest

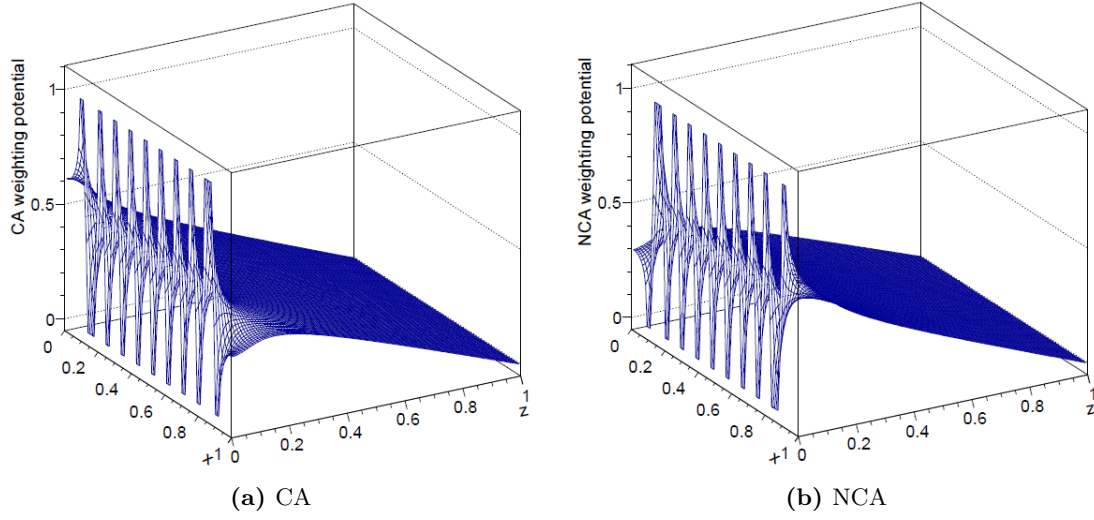**(a)** CA   **(b)** NCA

Figure 3.2: Depicted are the weighting potentials for the CA and NCA calculated along a plane
through the center of the detector, which are nearly equal at most locations. From
the cathode and the anode plane the weighting potential arises with a slope of $1/2$.
[85]

$$\Delta q_{CA} = \frac{1}{2} Q_0 (z_0 + 1) \qquad (3.1)$$

$$\Delta q_{NCA} = \frac{1}{2} Q_0 (z_0 - 1), \qquad (3.2)$$

with the magnitude of mobile charge Q_0 produced by the interaction at a distances z_0
between the anode plane and the interaction location. The depth dependence is removed
by subtraction

$$Q_0 = \Delta q_{CA} - \Delta q_{NCA}. \qquad (3.3)$$

Since Δq_{NCA} is always negative, the equation represents a sum of the absolute ampli-
tudes. To reconstruct the interaction depth z_0, the charge magnitude dependence is
removed

$$z_0 = \frac{\Delta q_{CA} + \Delta q_{NCA}}{\Delta q_{CA} - \Delta q_{NCA}}. \qquad (3.4)$$

These operational principles are the zeroth-order behavior. First-order effects, like elec-
tron trapping or hole trapping, complicate this simple picture and are further discussed
in [85].

3.3   Demonstrator Setup

The COBRA demonstrator setup is situated in the Italian underground laboratory LNGS to investigate the experimental issues of operating CdZnTe detectors in a low background environment and to identify potential background sources, while additional studies are being proceeded in surface laboratories.
The LNGS has an overburden of 1400 m of rock coverage corresponding to approximately 3800 m w.e. reducing the cosmic ray flux by about six orders of magnitude.

The current setup is able to handle in total 64 1 cm^3 CPG detectors, arranged in four layers each holding 4×4 detectors in a Delrin[3] support structure, shown in Figure 3.3b. The whole setup is schematically depicted in Figure 3.3a. To shield against the external gamma flux, 5 cm of ultra-radiopure copper and 20 cm of low-radioactivity lead surround the inner detector chamber. Coaxial cables and copper traces on a Kapton[4] foil, which are fed through the shield, guarantee the supply of bias voltage and signal read out.
Pre-amplifiers for semiconductor detectors have to be very sensitive. Electromagnetic (EM) disturbances can disturb the pre-amplifier by faking physics events in the cables from detector to the pre-amplifier or in the pre-amplifier itself. Therefore, the lead castle is enclosed by an electromagnetic interference (EMI) shield made of galvanized steel sheets, housing also the pre-amplifier of the readout chain. The weakest point of an EMI shield is the feed-through of the cables to operate the pre-amplifier. Thus, a copper chute was constructed to complete the EMI shield [86].
Since natural Cadmium contains 12 % abundance of the isotope ^{113}Cd, which has a very high cross section for thermal neutron capture, especially thermal neutrons have to be shielded. Therefore, the last layer consists of 7 cm boron-loaded polyethylene.
The whole setup is flushed with gaseous nitrogen constantly preventing radon contamination. The nitrogen is evaporated from liquid nitrogen.
In November 2013 the last layer was installed.
The DAQ system records complete pulse shapes for each event using 128 ADCs[5] and is optimized for event reconstruction and to allow for event discrimination.
In addition, a pulser was installed to send a simultaneous, fixed-amplitude signal to the pre-amplifier allowing stability tests of the DAQ system and more important coincidence analysis over the full detector array due to the synchronization of the clocks in the ADC modules. A time resolution smaller than 0.5 ms is achieved [87].

---

[3]Delrin: Polyoxymethylene (POM) developed by DuPont
[4]Kapton: Polyimide developed by DuPont and used for flexible circuits
[5]ADC: Analog-to-digital converter

(a) Schematic demonstrator setup

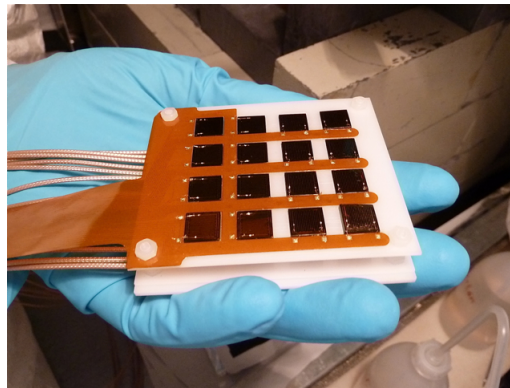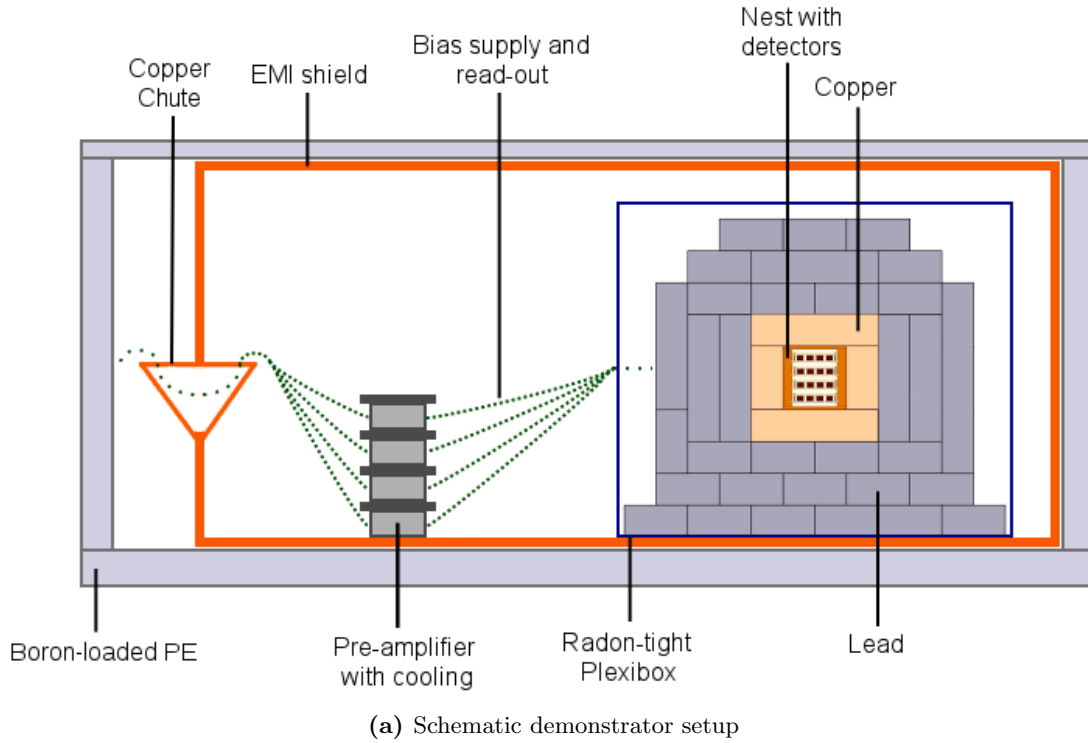**(b)** Complete 4×4 CPG detectors layer

Figure 3.3: Shown are pictures of the demonstrator setup at LNGS. The first picture shows the whole setup schematically. The shield is constructed out of copper and lead. Furthermore, an EMI shield surrounds the lead castle covered with boron-loaded polyethylene. A layer out of 4×4 CPG detectors supported by a Delrin structure with the bias supply and read-out cable can be seen in the second one. Altogether, four layers are implemented in the demonstrator setup.

3.4   Current Status

Since November 2013 COBRA operates 64 1 cm^3 CPG detectors arranged in four layers in the demonstrator setup at the LNGS. Furthermore, calibration runs with ^{22}Na and ^{228}Th are regularly performed. At the time of this thesis only the data with layer 1 (L1) and layer 2 (L2) was calibrated and available. Altogether, an exposure of 84.376 kg·days was achieved until June 2013. With a rate of approximately 2.0 kg·days/week for 48 detectors and 2.7 kg·days/week for 64 detectors the exposure is expected to be much higher for the combined data with the third (Start: July 2013) and forth layer (Start: November 2013). The processing and analysis algorithms of the recorded pulse shapes were implemented in the software package MAnTiCORE[6]. It offers special support to manage and track the numerous processing settings and calibration parameters. Further information about the analysis algorithms is described in citeschulz.

Figure 3.4 shows the energy resolution of 32 1 cm^3 CPG detectors, which are operated in the demonstrator setup at LNGS. The median value is 1.5 % FWHM. The two worst detectors are from an older batch and not representative of detectors that will be deployed in the future.
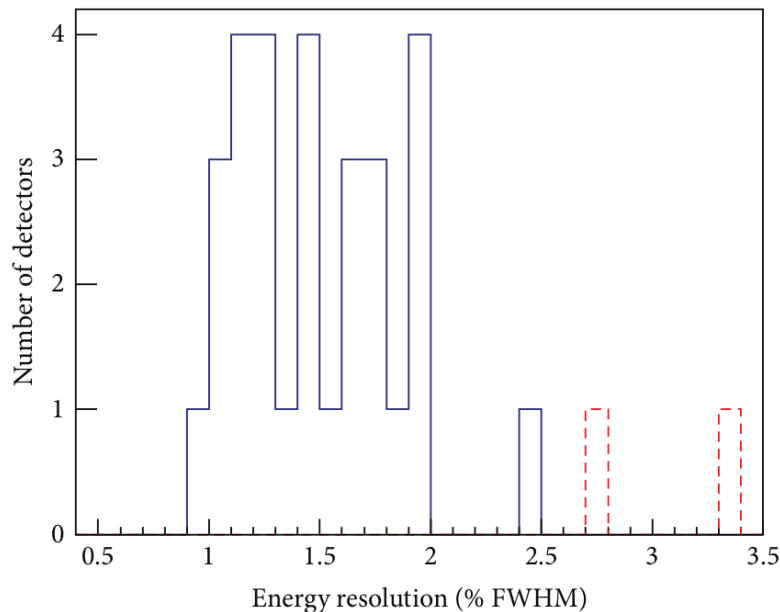
Figure 3.4: Plotted are the resolutions of 32 operating detectors in the demonstrator setup at LNGS extrapolated to 2.814 MeV. The two worst detectors, indicated with a dashed red line, are from an older batch and not representative. The median value is 1.5 % FWHM. [87]

Figure 3.5 shows the spectrum of the L2 data. Here, the interaction depth z is plotted against the deposited energy E. The cathode is positioned at $z = 1$, while are at $z = 0$.

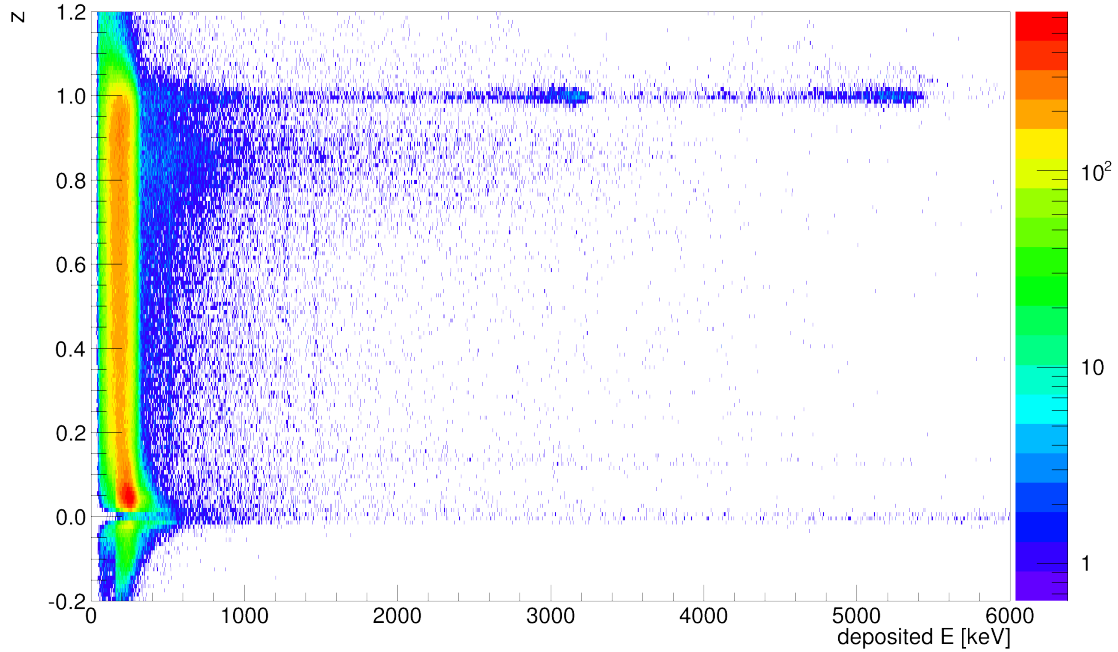[6]MAnTiCORE: Multiple-Analysis Toolkit for the COBRA Experiment

Figure 3.5: Shown is the interaction depth z versus the deposited energy E of the L2 data,
corresponding to an exposure of 84.376 kgd. The following feature can be identified:
β spectrum from ^{113}Cd in the high counting region below 200 keV, α peak at
3.249 MeV from ^{190}Pt, α peak at 5.407 MeV from ^{210}Po, radon progeny in the
hump region ($0.8 < z < 1$), γ lines at 1.46 MeV from ^{40}K and at 0.511 MeV
from annihilation. Other events correspond mostly to α contamination on lateral
surfaces, which also cause the main background in the ROI.

Some important features and background sources can be identified. In the high counting
region below 200 keV the β spectrum from ^{113}Cd can be seen. This background source
is part of the detector material, therefore intrinsic and irreducible. At the cathode side
($z = 1$) two regions with higher statistic corresponding to α peaks can be recognized.
The first peak at 3.249 MeV corresponds to ^{190}Pt. Platinum is part of the cathode
material. The second one at 5.407 MeV belongs to ^{210}Po. Polonium is a progeny of
radon and its grandmother nuclide ^{210}Pb with its high half-life of 22.3 years is able to
settle down on surfaces, in particular on statically charged surfaces, see section 2.4.3.
Furthermore, a hump between $0.8 < z < 1$ can also be assigned to the radon progeny
^{210}Bi and ^{210}Po, which deposited on the surface of Delrin support structure [88].
The anode region ($z = 0$) is dominated by reconstruction distortions, which also cause
reconstructed events with $z < 0$ or $z > 1$. In addition, a γ line at 1.46 MeV originating
from ^{40}K can be spotted. A second γ line at 0.511 MeV from annihilation is also visible.
Other events originate mainly from α contamination on lateral surfaces [89], which also
cause the main background in the ROI. Thus, they also have to be considered as potential
background sources for a large scale setup and are further investigated in Chapter 5.

Chapter 4

Development of a Shield

An efficient radiation shield for a large scale COBRA experiment is developed by Monte Carlo simulations comparing commercially available shielding materials. A shield is the crucial setup part to achieve a total background level of 10^{-3}/kg/keV/yr to be competitive with other experiments. Thus, the goal was to identify the most effective combination of different material layers to reduce external radiation to a minimum.

A discussion about Monte Carlo simulations in general, the used simulation framework and applied cuts can be found in Section 2.5.

4.1 Method

Regarding the listed categories of background sources in Section 2.4, the most important one is radioactivity in the environment, the detector, support structures, surrounding air and the shielding material. For the development of a shield the radioimpurity of the detector itself and the surrounding support structure and air cannot be influenced and has to be dealt with other techniques, like e.g. coincidence analysis. Furthermore, radiopurity of the shielding materials has to be considered for the ordering of the individual layers. Produced α, β, γ rays in the shield material, e.g. lead, should be removed by other material layers. Therefore, a more radiopure material, e.g. copper, should be used as inner layer instead of e.g. lead. Furthermore, radioactivity in the environment, e.g. from the rock or concrete, has to considered. But as α, β, γ rays generated in the shield are re-absorbed, also radioactivity in the environment is negligible. More important for the development of a shield are higher energetic particles from the primary and secondary component of cosmic rays. Here, muons can be generally vetoed by a possible active component of a shield or, especially for COBRA, identified by the modular design through coincidence analysis. Another component are muon-induced neutrons, which can travel large distances unnoticed, because the neutron energy can have up to several GeV and they carry no charge. Furthermore,

natural cadmium contains the isotope ^{113}Cd, which has a high cross section for neutron capture, with a natural abundance of 12.22 %. In a ^{113}Cd(n,γ)^{114}Cd reaction γ rays with an energy of several MeV are emitted resulting in possible entries in the ROI. Thus, the development of a shield starts with tests for the effectiveness in shielding against high-energetic muon-induced neutrons keeping in mind material properties, like radiopurity.

The strategy to investigate a shield was to examine each considered material for its muon-induced neutron interactions properties, see Section 4.3, and then to maximize the attenuation for the neutron radiation by combining multiple materials, building a multi-layer shield, see chapter 4.4.

Any neutron shield has to be constructed in a way that high-energetic neutrons are moderated as fast as possible and subsequently captured. An accompanied complication for the shield design are secondaries, like gammas from capture processes. Their production and attenuation are also regarded. Additionally, a shield should be as compact and cost-effective as possible.

In the simulation monoenergetic neutrons were aimed at the center of a 1 m thick slab, subdivided into 1 mm thick slices, of each material. The used GDML geometry had the size of 10 m×10 m×1 m. The dimension in x and y are much larger as in z, guaranteeing the whole hadronic shower is contained. The geometry is schematically depicted in Figure 4.1. Here, the blue arrows represent the incoming monoenergetic neutrons, while the red arrows represent the neutron flux after passing through the material. In addition, the neutrons are tracked throughout the volume, because of the fine binning. The energies of the simulated neutrons E vary between 1 keV and 10 MeV to cover a wide energy range. Neutrons with energies smaller than 1 keV can be neglected, although they are much more common, see Table 2.3 in Section 2.4, but are not able to either reach or penetrate a shield.

A standard neutron shield consists of three layers: a moderator, an absorber and a high-density material, e.g. a metal [90]. The high-density material can be used for photon absorption or neutron capture and moderation or even both. Therefore, the position of the metal was either set in front or behind the moderator and absorber combination. The most efficient moderator is hydrogen, because neutrons can lose up to all of its energy in one collision. For heavier nuclei, only partial energy transfer is possible. If the energy of the neutron is sufficiently high, inelastic scattering can take place in which the remaining nucleus is elevated to an excited state. Although the neutron loses a greater fraction of its energy compared to an elastic scattering, the nucleus de-excites, emitting a gamma ray leading to secondary radiation. For more information about neutron interactions and the production of other secondaries in general, see Section 2.3.4.
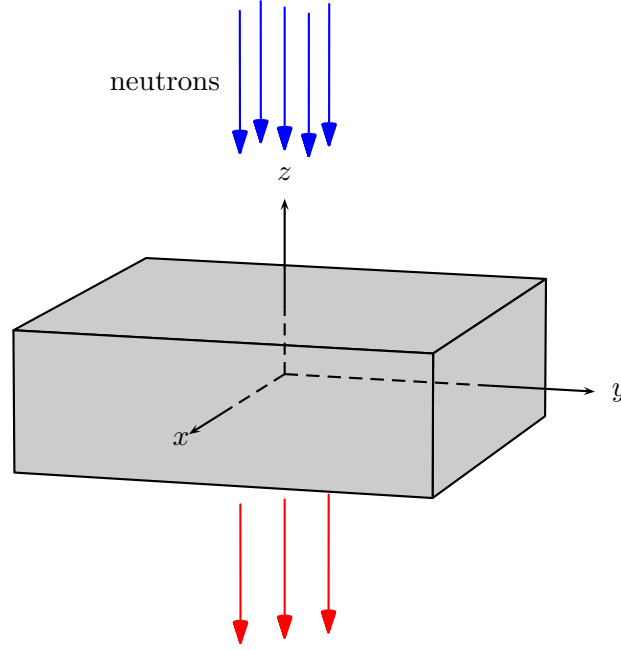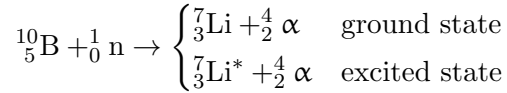
Figure 4.1: Schematically plotted is the GDML geometry used for the simulations of the development of a shield. The dimensions are $10\,\text{m} \times 10\,\text{m} \times 1\,\text{m}$, guarenteeing the whole shower is contained. The blue arrows represent the incoming monoenergetic neutrons, while the red arrows represent the neutron flux after passing through the material. The incident energies vary between $1\,\text{keV}$ and $10\,\text{MeV}$.

Popular absorber materials next to gadolinium and cadmium are boron and lithium, which can also be combined with hydrocarbons. For ^{10}B the reaction can be written as

$$^{10}_{5}\text{B} + ^{1}_{0}\text{n} \rightarrow \begin{cases} ^{7}_{3}\text{Li} + ^{4}_{2}\alpha & \text{ground state} \\ ^{7}_{3}\text{Li}^{*} + ^{4}_{2}\alpha & \text{excited state} \end{cases}$$

For thermal neutrons about $94\,\%$ of all reactions lead to the excited state [45]. Another popular reaction with ^{6}Li is the following. Here, the reaction proceeds only to the ground state.

$$^{6}_{3}\text{Li} + ^{1}_{0}\text{n} \rightarrow ^{3}_{1}\text{H} + ^{4}_{2}\alpha$$
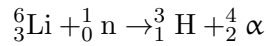
In Figure A.1 the total cross section for neutrons in ^{10}B and ^{6}Li are plotted. It is shown that for a wide energy range the total cross section is above 1 barn. For thermal neutrons at approximately $1\,\text{meV}$ the total cross section increases rapidly due to (n,α) reactions. For neutron energies above $1\,\text{MeV}$ inelastic scattering becomes important.

Produced secondary α particles can be neglected, because due to the high-density material in the shield the energy loss is great, see also Section 2.3.1. However, also neutrons can be produced through (α,n) reactions and are further discussed as possible background source in Section 5.

The considered materials with their properties concerning composition and density used

in the simulations are listed in Table 4.1. All tabulated materials are commercially available and most of them are special neutron shielding materials, e.g. (doped) hydrocarbons. In addition, some pure metals like copper, lead and iron were added.

Table 4.1: Tabulated are the composition and the density of the examined materials. Most of them are special neutron shielding materials, e.g. hydrocarbons. In addition some pure metals like copper, lead and iron were added for photon capture purpose.

Material	Composition [ratio]	Density [g/cm^3]
Copper	nat.	8.96
Lead	nat.	11.35
Iron	nat.	7.824
PE	CH_2 [1:2]	0.92
PE+Li (7.5 %)	CH_2,Li [1:2:0.24]	1.06
PE+B (30 %)	CH_2,B [1:2:0.34]	1.12
PE+B (5 %)	CH_2,B [1:2:0.18]	1.6

With the received data, the best neutron attenuators can be determined as well as the development of the hadronic shower throughout the material investigated. After the shield the combination of the neutron and gamma rate as well as their kinetic energy should be reduced to a minimum. This way, they can be neglected as background sources. Furthermore, the thickness of single shield layers is varied in 5 or 10 cm steps due to the standardized size of material bricks. In total, the shield should have a size of maximal 40 cm to fit in the current hut at LNGS.

In the analysis of the simulations the neutron and gamma population is investigated as function of the thickness d of the block. The population is defined as

$$N_{i,\mathrm{norm},E} = \frac{N_{i,E}}{N_{\mathrm{n,sim}}} \tag{4.1}$$

with $i = \mathrm{n}, \gamma$ and the incident neutron energy $E = 1\,\mathrm{keV}, 2.5\,\mathrm{MeV}, 5\,\mathrm{MeV}, 10\,\mathrm{MeV}$. $N_{i,E}$ is the number of neutrons or gammas in a single 1 mm bin, while $N_{\mathrm{n,sim}}$ is the total number of simulated neutrons. In general, a quantity of 10^6 neutrons was generated per simulation. Therefore, $N_{\mathrm{n,sim}} = 10^6$. Furthermore, two cuts were applied to $N_{i,E}$. The first one deals with the momentum direction to reduce backscattering effects. Compared to the schematic plot of the used geometry in Figure 4.1 the momentum in z, p_z, has to be smaller than zero

$$p_{z,i} < 0 \text{ with } i = \mathrm{n}, \gamma. \tag{4.2}$$

The second cut neglects stopped neutrons and gammas with kinetic energy E_{kin} equal to zero

$$E_{kin,i} > 0 \text{ with } i = \mathrm{n}, \gamma. \tag{4.3}$$

4.1.1   Previous Shield Design

A passive shield was already developed by D.Y. Stewart from the University of Warwick [91] concerning neutrons and photons attenuation. In Figure 4.2 the shield design is schematically depicted. A special feature of this shield is a recurring sequence of polyethylene (PE), 5 %-boronated polyethylene PEB5 and lead guaranteeing a neutron moderation and absorption followed by a gamma capture material. Furthermore, layers of lithium-doped (PELi) and bismuth-doped polyethylene (PEBi) are used.
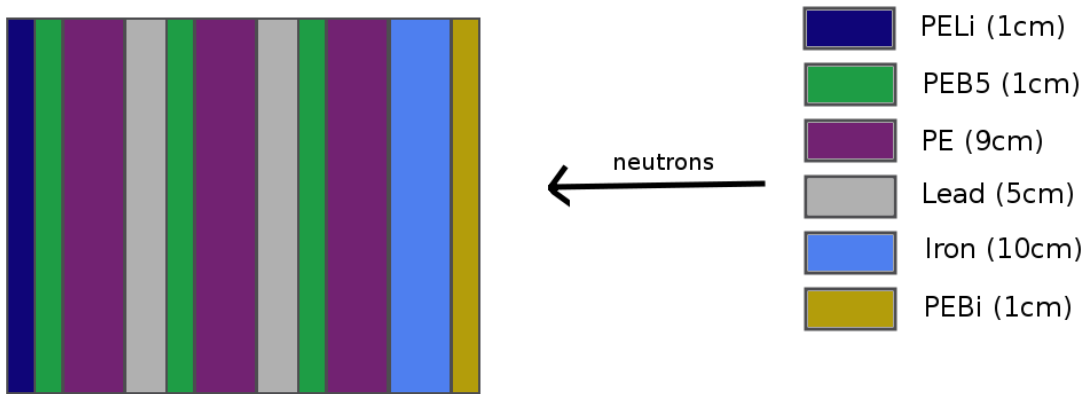
Figure 4.2: Schematically illustrated is the shield design by the University of Warwick. It consists of eleven narrow layers making it complex and hard to construct.

On the other hand, due to eleven layers in total, the shield design is complex. Furthermore, many layers are narrow with only 1 cm thickness requesting a more difficult mounting construction. The whole shield has a size of 52 cm.

4.2   Comparison of the Physics Lists

In Section 2.5 the simulation package VENOM was introduced. Furthermore, the two relevant physics lists used with VENOM, DMXPhysicsList and Shielding, were discussed.

For the shield development both physics list were tested and compared with each other. For the test simulation, neutrons with an initial energy of 5 MeV were aimed at a 1 m slab of material, either PEB5 or lead. Furthermore, the slab is subdivided into 1 mm bins as discussed in Section 4.1. Due to different cuts[1], which are applied within the individual lists, all test simulations were performed four times. The neutron quantity is 10^6 for each simulation.

Figure 4.3a shows the neutron attenuation $N_{n,norm,5MeV}$, defined in Equation 4.1, for PEB5 and lead. The general shape of the spectra is discussed in Section 4.3. However,

---

[1]As described in Section 2.5, the default cut of the DMXPhysicsList is 1 μm, while in the Shielding physics list 0.7 mm were set.

all four simulations with PEB5 show the identical development. For the lead simulations small deviations can be identified, but can be neglected. Nevertheless, the shape is the same.

The production and attenuation of gammas $N_{\gamma,\mathrm{norm,5MeV}}$ is plotted in Figure 4.3b. Here, the development for the rate in lead as well as in PEB5 are equal no matter which physics list or corresponding cut were used. Therefore, both physics lists are in agreement within the statistic error.

However, the Shielding reference list is an official Geant4 physics lists and recommended by the Geant4 collaboration leading to regular maintenance and updates, while the DMXPhysicsList originates from a Geant4 example. Hence, for all further simulations the Shielding reference list with the implemented default cuts is used.
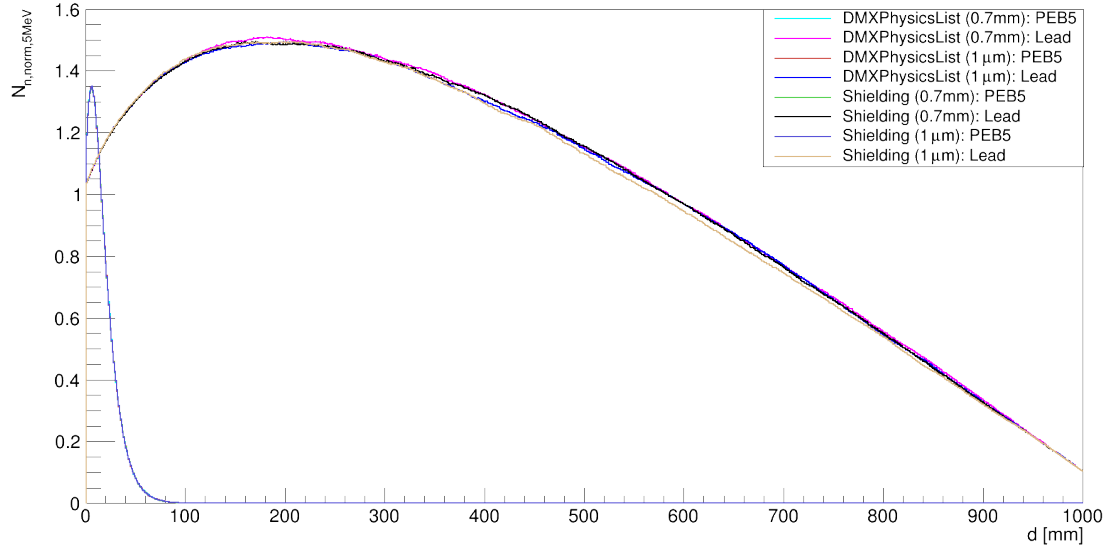
(a) Neutron population $N_{\mathrm{n,norm,5MeV}}$ for PEB5 and Lead
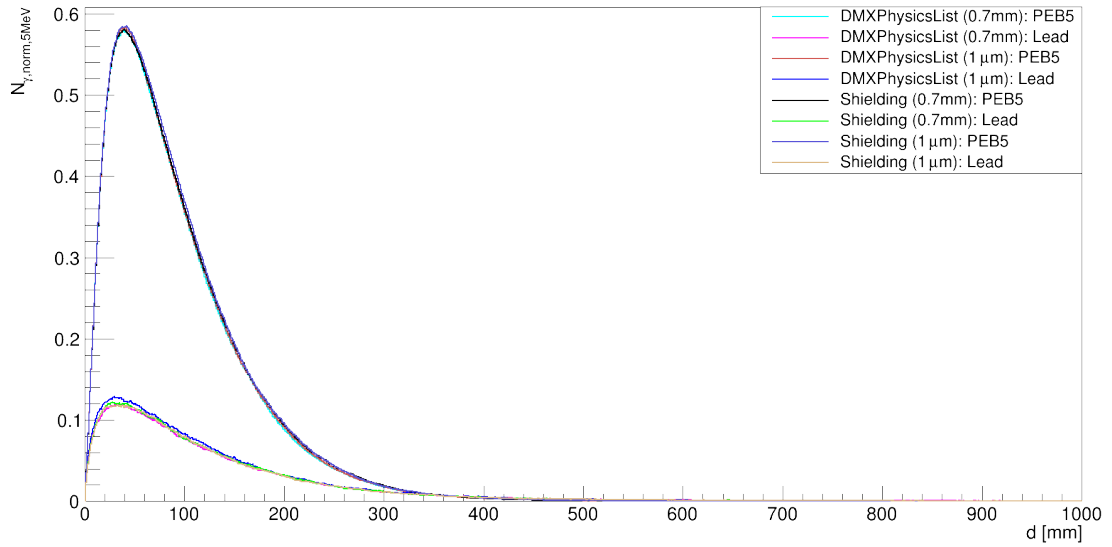
(b) Gamma population $N_{\gamma,\mathrm{norm,5MeV}}$ for PEB5 and Lead

Figure 4.3: Plotted are the population of neutrons $N_{\mathrm{n,norm,5MeV}}$ and gammas $N_{\gamma,\mathrm{norm,5MeV}}$ in PEB5 and lead simulated with different physics lists and applied cuts. The shape of all four spectra fit to each other. The neutron population for PEB5 as well as the gamma population for PEB5 and lead show the same result. For the neutron population of lead small deviations can be identified, but can be neglected.

4.3   Single-layer Shield Properties

In this section the properties of the considered materials are investigated concerning the effectiveness to shield muon-induced neutrons. As described in Section 4.1, neutrons were aimed at a 1 m thick slab of material. The simulated neutron energies E are 1 keV, 2.5 MeV, 5 MeV and 10 MeV and in the analysis the neutron and gamma population, see Equation 4.1, is calculated depending on the thickness d of the block.

In Figure 4.4a the neutron population $N_{n,norm,1\,keV}$ is depicted. The PEB5 performs best next to the lithium doped polyethylene (PELi) and the 30 %-boronated polyethylene (PEB30). Here, less than 5 cm are sufficient to reduce the neutron rate below 10^{-2} for all three materials. The cross section for (n,α) reactions is one order of magnitude higher for boron than for lithium, see Figure A.1. Therefore, boron absorbs neutrons better. On the other hand, fast neutrons are less moderated if the abundance of boron is higher. Hence, less neutrons are captured by PEB30 compared to PEB5 after a certain thickness d. After 8 cm of PEB30 the neutron rate can be reduced down to 10^{-4}, while 2 cm are already sufficient for PEB5. The doped hydrocarbons clearly dominate the pure polyethylene due to (n,α) reactions of thermal neutrons. In contrast, all metals are decreasing the neutron population worse and need much higher thicknesses of material, e. g. iron requires 30 cm for a neutron rate below 1 %, because for neutron energies less than 1 MeV elastic scattering dominates in metals. Furthermore, the cross section of (n,α) reactions, exemplary depicted in Figure A.2a for ^{208}Pb and in Figure A.2b for ^{63}Cu, is several orders of magnitude smaller compared to ^{10}B and ^{6}Li.

In Figure 4.4b the gamma population originating from (n,γ)-reactions is plotted. Here, lead is a superior shielding material. The γ-production is smaller than from all other materials reaching roughly 10^{-3} at maximum, because the cross section for radiative capture has a minimum for neutrons with an energy of 1 keV. But even though, with decreasing neutron energy, the cross section increases gently and thus also the gamma rate. In contrast, the hydrocarbons show a remarkable feature that has to be kept in mind. Although their performance with respect to neutron moderation and capture is very good, there is a huge difference in terms of photon attenuation. Thus, all hydrocarbons perform worse than the high-density materials calling for a 30 cm thick block of material at least to reduce the photon rate below 10^{-2} comparing to 25 cm for the worst displayed metal iron.

Concentrating on the determination of the thickness of a shield or for the first layer of a potential multi-layer shield, neutrons with higher energy are examined. The neutron population with an initial energy of 5 MeV $N_{n,norm,5\,MeV}$ is depicted in Figure 4.5a. The result is comparable to the data received from the simulations with an initial energy of 1 keV. The best performing material is PEB5. The neutron population drops by three orders of magnitude for PEB5 after less than 10 cm and by less than one order of magnitude lead after 1 m. The corresponding gamma population per simulated neutron with an initial energy of 5 MeV $N_{\gamma,norm,5\,MeV}$ is shown in Figure 4.5b. Compared

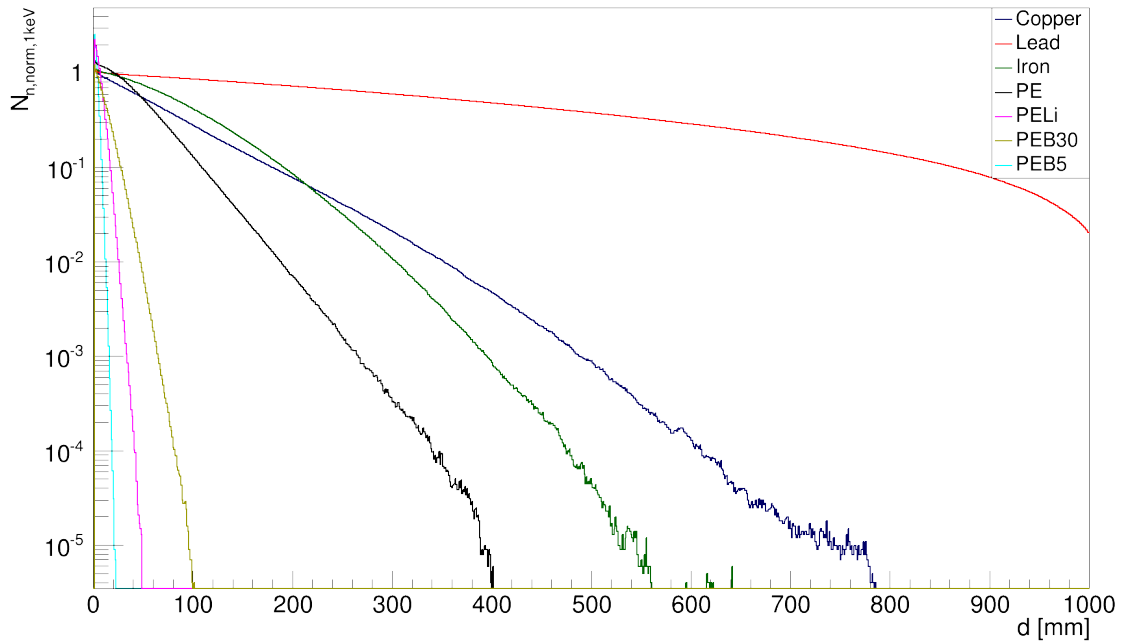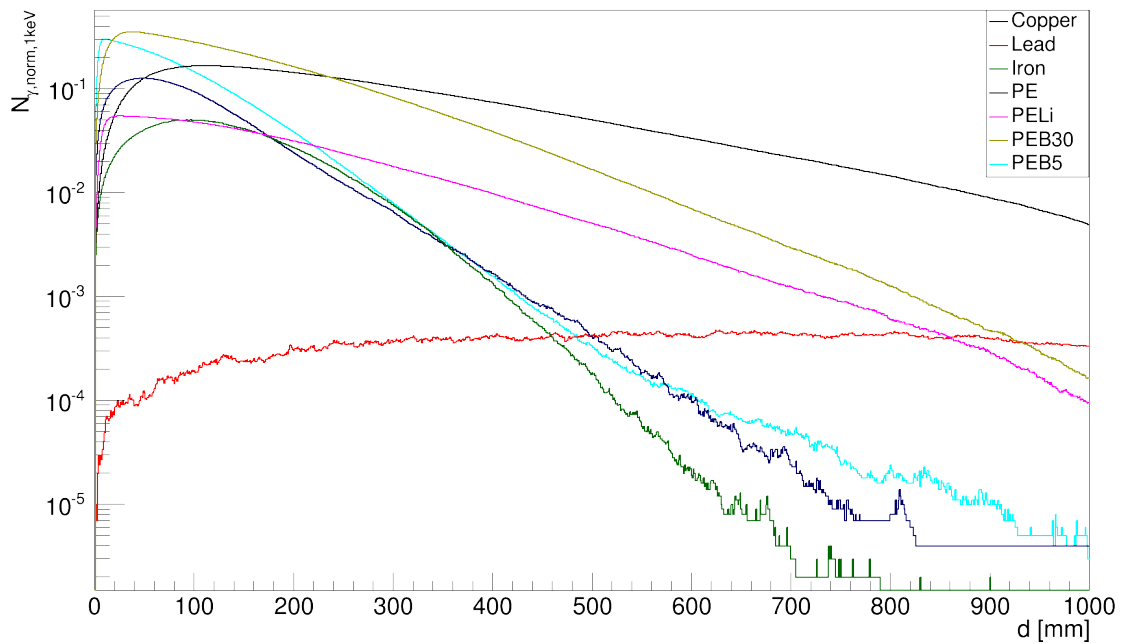**(a)** Neutron population $N_{\mathrm{n,norm,1\,keV}}$

(b) Gamma population $N_{\gamma,\,\mathrm{norm,1\,keV}}$

Figure 4.4: Plotted is the population for neutrons and gammas for an incident neutron energy of $E = 1\,\mathrm{keV}$. Regarding effectiveness against neutron shielding PEB5 performs best next to PELi and PEB30, while lead shows a low production rate for gammas.

to the results of $E = 1\,\mathrm{keV}$ the gamma population in metals increases for $E = 5\,\mathrm{MeV}$ because inelastic scattering and radiative capture becomes more important with increas-
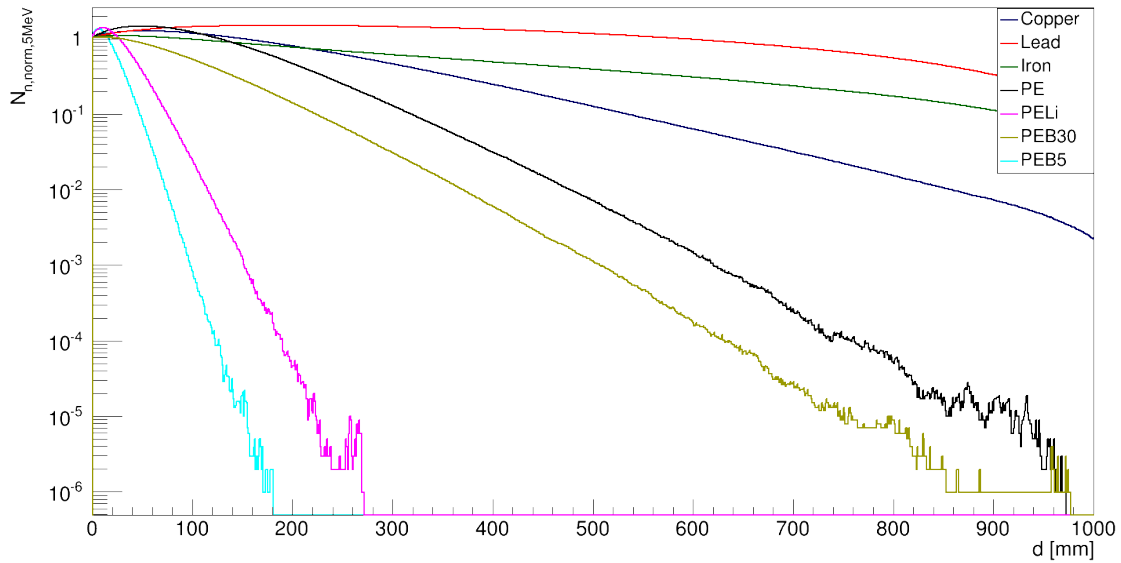
(a) Neutron population $N_{n,norm,5\,MeV}$
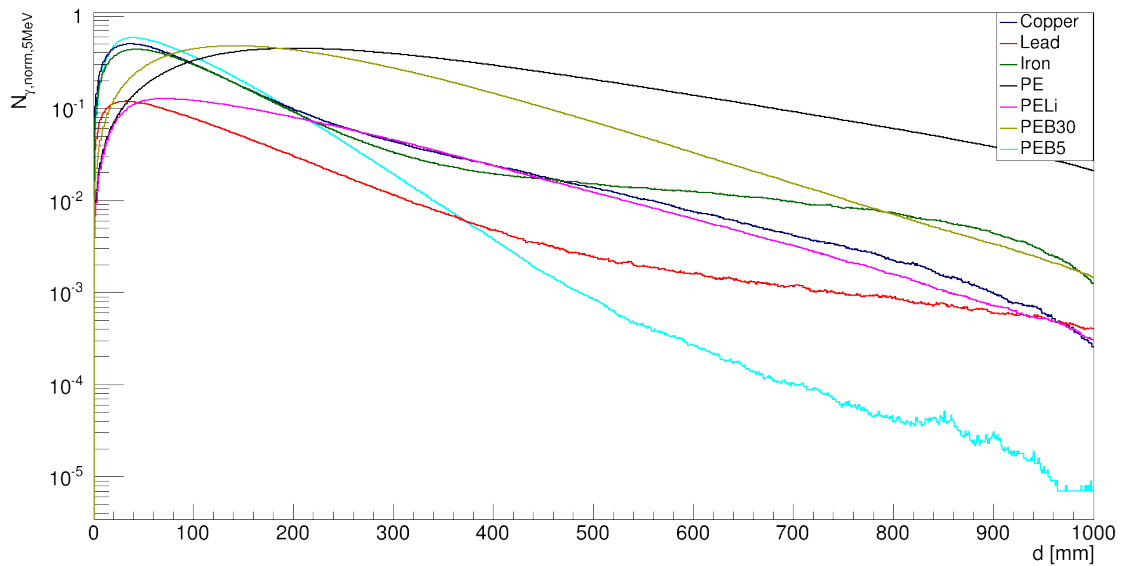
(b) Gamma population N_γ, norm,5 MeV

Figure 4.5: Plotted is the population for neutrons and gammas for an incident neutron energy of $E = 5\,MeV$. The results are comparable to the $E = 1\,keV$ simulation. For an effective neutron attenuation PEB5 or PELi is the best choice, while lead performs best regarding (n,γ) self shielding effects.

ing neutron energy. Regarding self-absorption of gamma rays, it is shown that PE and nearly all doped PEs hardly re-absorb their own gamma radiation, making more than $1\,m$ material necessary to decrease the gamma rate below 10^{-2}. An exception is PEB5 demanding approximately $35\,cm$. The superior material lead for $E = 1\,keV$, produces a maximum number of photons of 0.11 in the $E = 5\,MeV$ case. Copper generates in

contrast a maximum number of photons of 0.5. Furthermore, the gamma population drops below 10^{-2} after 30 cm of lead, whereas copper needs 60 cm. Therefore, lead is the best choice for shields up to a thickness of 30 cm. For thicker shields PEB5 reduces the gamma rate better, because all neutrons are captured and thus, no additional gammas are produced. With this, even lower rates are achievable. Therefore, PEB5 would be the best choice for a possible single-layer shield due to the great properties concerning neutron attenuation. However, not only the quantity is decisive, but also the kinematic energy of the remaining particles. Figure 4.6 shows the kinetic energy of neutrons and gammas after a certain thickness of PEB5 shield for an initial neutron energy of 5 MeV. The kinetic energy for neutrons after 5 cm and 10 cm of PEB5 differ from each other. Although the shape resemble, the quantity is reduced by two orders of magnitude for a thicker shield. Yet, few neutrons with energy above the ROI are registered. For gammas, even after 50 cm kinetic energies above the ROI are detected. Thus, a single-layer shield is unpractical due to the necessity of more than 50 cm of material.
For higher initial neutron energies the material thickness has to be larger. In Figures C.1 – C.2 in Appendix C the neutron and gamma population are plotted for initial energies E of 2.5 MeV and 10 MeV.

In Table 4.2 necessary thicknesses of materials are summarized regarding an effective neutron attenuation and (n,γ) self-absorbing effects. Here, the neutron rate is below 10^{-2} and the gamma rate below 10^{-3} referring to the performance of PEB5.

Table 4.2: Summarized are thicknesses of different materials regarding an effective neutron attenuation and (n,γ) self-absorbing effects with different initial neutron energies E for the first layer of a shield. The neutron rate is below 10^{-2} and the gamma rate below 10^{-3} referring to the performance of PEB5.

	Neutron population				Gamma population		
	d [cm] (2.5 MeV)	d [cm] (5 MeV)	d [cm] (10 MeV)		d [cm] (2.5 MeV)	d [cm] (5 MeV)	d [cm] (10 MeV)
Copper	80	< 85	85	Copper	85	< 90	< 90
Lead	< 100	> 100	> 100	**Lead**	**< 65**	**< 70**	**< 90**
Iron	< 100	> 100	> 100	Iron	100	> 100	> 100
PE	30	< 50	55	PE	> 100	> 100	> 100
PELi	**< 10**	**< 15**	**15**	PELi	80	< 85	90
PEB30	<25	< 40	<45	PEB30	85	> 100	> 100
PEB5	**< 5**	**< 10**	**10**	**PEB5**	**45**	**< 50**	**< 55**

Regarding an effective neutron attenuation also PELi is a good choice. With a maximum thickness of 10 cm for $E_{n,sim} = 10$ MeV the neutron population can be reduced down to 10^{-2}. In contrast, lead is the best choice regarding (n,γ) self shielding effects for thin layers, whereas PEB5 is the better material for thicker layers. But even though, a multi-layer shield is required to reduce the combined neutron and gamma rate further.
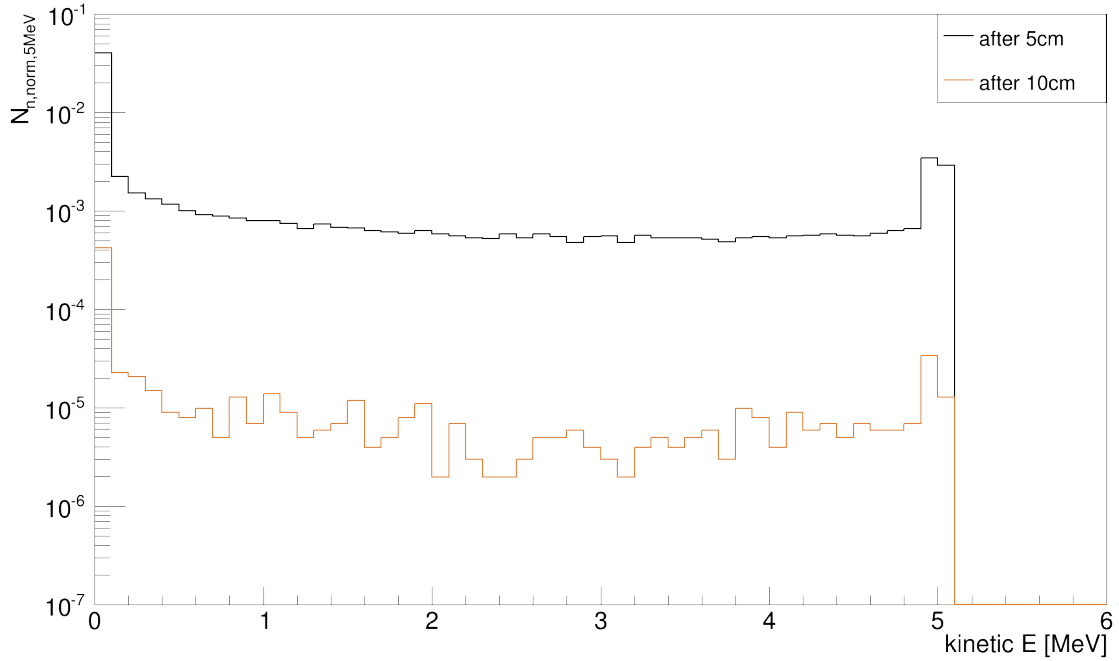
(a) Kinetic energy of neutrons
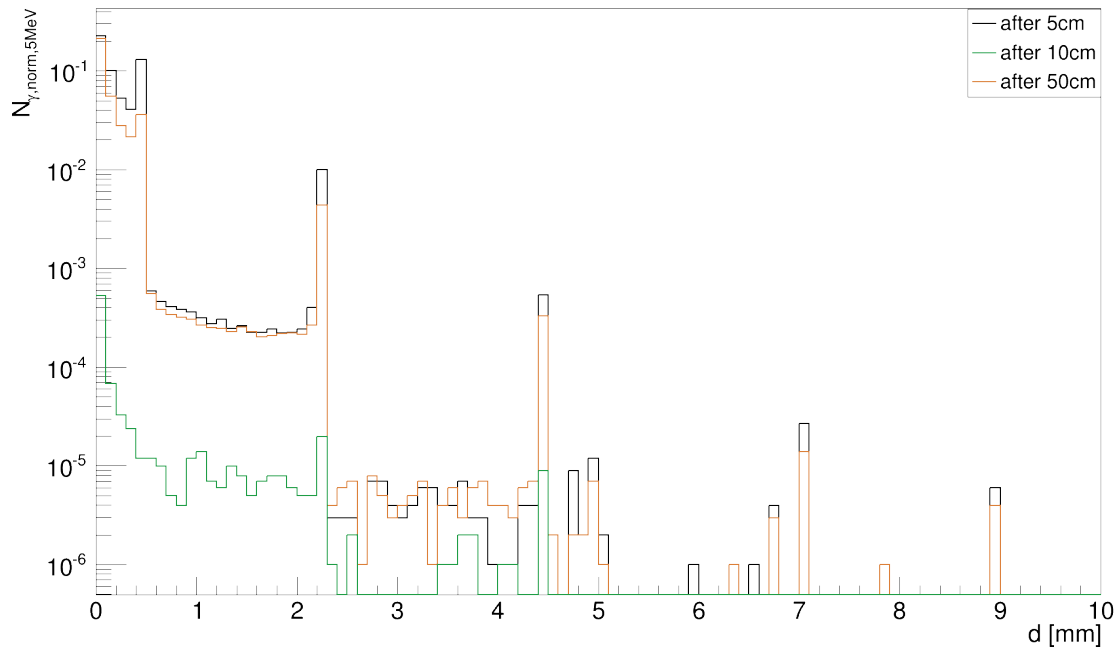
(b) Kinetic energy of gammas

Figure 4.6: Plotted is the kinetic energy for neutrons and gammas for an incident neutron
energy of $E = 5\,\text{MeV}$ in a PEB5 shield after certain thicknesses. The shape of
the kinetic energy spectra for neutrons resemble after $5\,\text{cm}$ and $10\,\text{cm}$ of PEB5,
although the quantity is reduced by two orders of magnitude. Few neutrons with
energy above the ROI are registered. For gammas still after $50\,\text{cm}$ the energies
above the ROI are detected.

4.4 Multi-layer Shield Properties

In this section the most effective combination of three materials is defined starting with the determination of the thickness of the second material layer. Recommended thickness of a single layer shield or rather the first layer was already determined in Section 4.3 and summarized in Table 4.2.

For this purpose, the GDML geometry consisting of a 1 m thick block was divided into two material layers. To investigate the flux of neutrons and neutron-induced secondary radiation the block was subdivided into 1 mm slices. A neutron beam with different initial energies was then focused to the center of the block. Regarding Section 4.3, considered combinations were:

PEB5 (10 cm) − Lead/Copper (90 cm)
PELi (10 cm) − Lead/Copper (90 cm)

Doped polyethylene displayed a very good performance concerning neutron attenuation and 10 cm of material is sufficient to reduce the neutron population below 10^{-2} for initial neutron energies up to 10 MeV. Furthermore, lead is the best choice for thinner layers to decrease gamma population. Copper is added, because it can be produced radiopure, even though it shows a worse performance regarding neutron attenuation and (n,γ) self shielding effects.

In Figure 4.7a the neutron attenuation $N_{\text{n,norm,5\,MeV}}$ is plotted for an incident neutron energy of $E = 5$ MeV. The results from Section 4.3 are confirmed. After 10 cm of PEB5 the neutron rate drops below 10^{-3}, whereas 10 cm of PELi only reach 0.03. At the border to the second layer the neutron rate drops. The neutrons are backscattered and thus, removed by the cut, see Equation 4.3. The further attenuation of neutrons can be distinguished between copper and lead. In both cases, copper reduces the neutron rate better, because the cross section for radiative capture is approximately five orders of magnitude higher, see Figure A.2. Nevertheless, the neutron rate slopes down gentler. Thus, more high-density material is needed to decrease the neutron rate by one order of magnitude, e.g. 35 cm of copper in combination with 10 cm PEB5 for the most compact solution.

Regarding the gamma population $N_{\gamma,\text{norm,5\,MeV}}$, depicted in Figure 4.7b, the results from Section 4.3 are also confirmed. After an increase within the doped PE layer, both metals, especially lead, decrease the photon rate effectively, because less neutrons with smaller energies are entering the lead layer. After additional 10 cm of lead the gamma rate is reduced to 10^{-4} for neutron energies $E \leq 5$ MeV for PEB5.

In Figure 4.8 the kinetic energy of neutrons and gammas after a certain thickness are plotted for the PEB5 − Lead shield. The quantity of neutrons is decreased from 584 to 577 by adding 10 cm of additional lead. Also, the energy distribution is moved to lower energies from 0.81 MeV to 0.46 MeV calculated as average. However, the difference between the distribution after 20 cm or 30 cm is minimal. In contrast, for the gamma
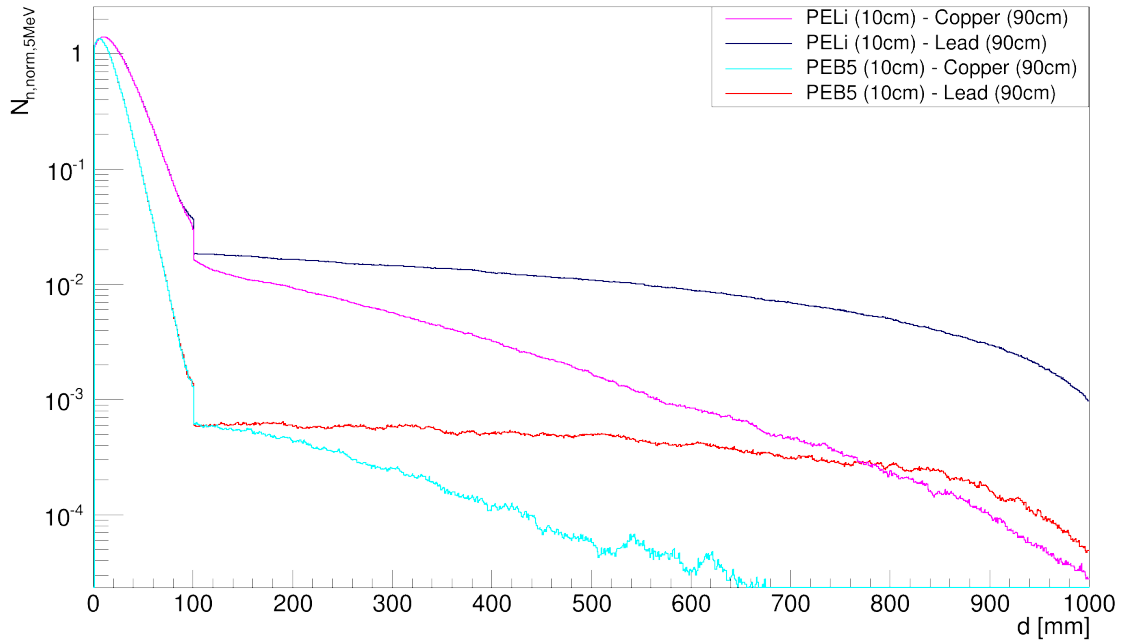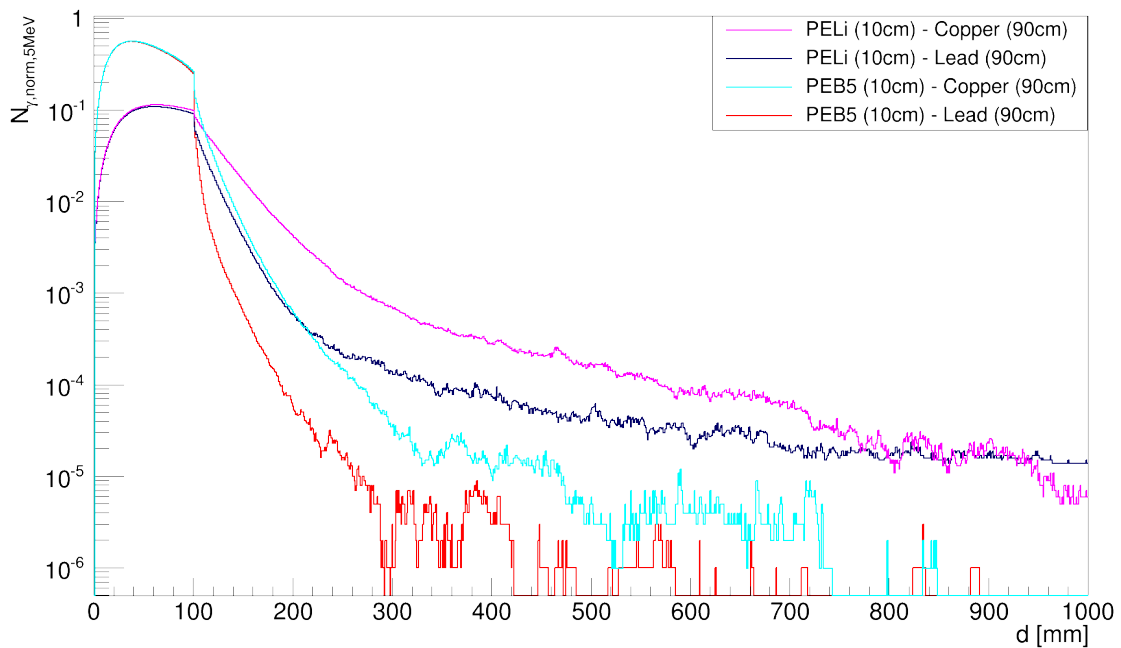
(a) Neutron population $N_{\mathrm{n,norm,5\,MeV}}$ for two layer shields

(b) Gamma population $N_{\gamma,\mathrm{norm,5\,MeV}}$ for two layer shields

Figure 4.7: Plotted is the population for neutrons and gammas for an incident neutron energy of $E = 5\,\mathrm{MeV}$ in two layer shields. PEB5/PELi reduces the neutron rate down to $10^{-2}/0.03$. The further attenuation of neutrons can be distinguished between copper and lead. Copper reduces the neutron rate better. Regarding the gamma population both metals, especially lead, decrease the photon rate effectively.
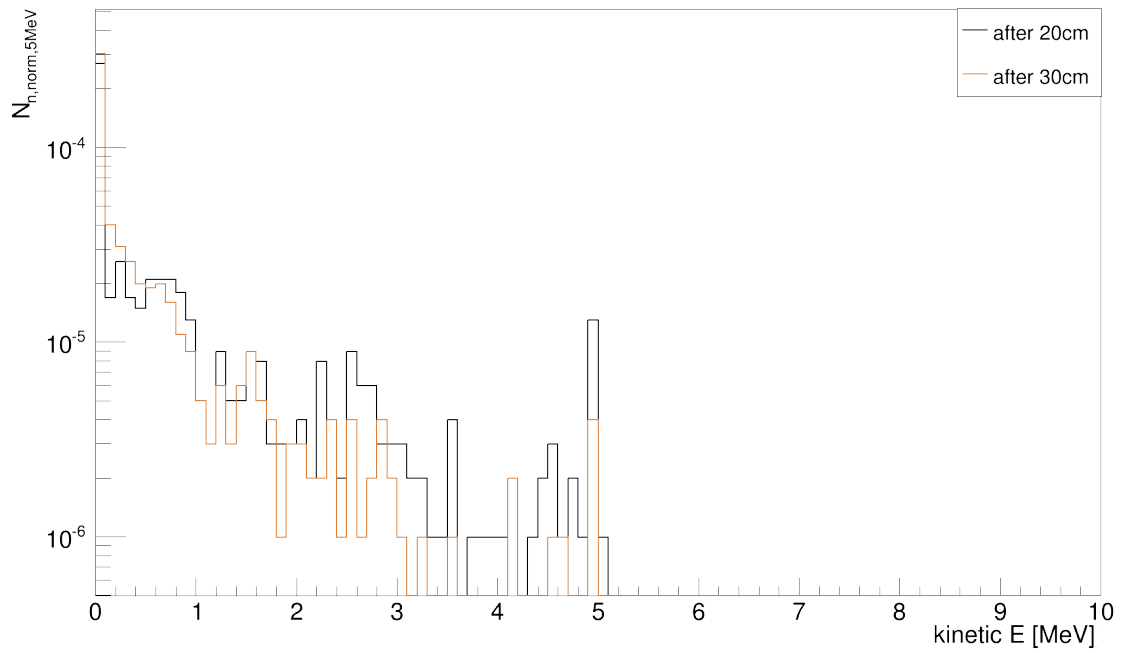
(a) Kinetic energy of neutrons
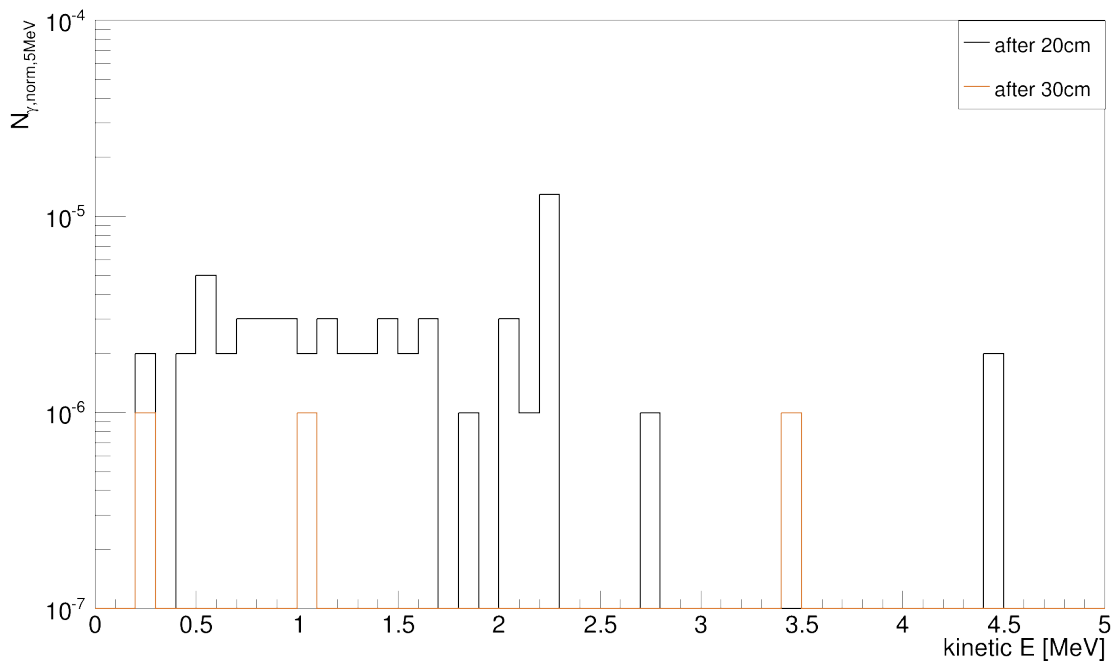
(b) Kinetic energy of gammas

Figure 4.8: Plotted is the kinetic energy for neutrons and gammas for an incident neutron energy of $E = 5\,\text{MeV}$ in a PEB5 $(10\,\text{cm})$ – Lead shield after certain thicknesses. The spectra of the kinetic energy for neutrons equal with minimal deviations. For gammas, their population is decreased for an additional $10\,\text{cm}$ of lead.

population the additional 10 cm of lead are decisive. The quantity is reduced from 58 to 3 entries. Yet, a statement for the kinetic energy distribution is limited due to the statistic. The kinetic energy average 1.5 MeV after 10 cm of lead compared to 1.6 MeV after 20 cm.

In Table 4.3 necessary thicknesses for the second material layer are summarized regarding an effective neutron attenuation and (n,γ) self-absorbing effects for different initial energies compared to the combination of 10 cm PEB5 and 10 cm lead. The corresponding figures for $E = 2.5$ and 10 MeV can be found in Appendix C, Figure C.3 – C.4.

Table 4.3: Summarized are thicknesses of lead and copper in combination with either PELi or PEB5 regarding an effective neutron attenuation and (n,γ) self-absorbing effects with different initial neutron energies E as second layer of a shield. The neutron rate is below 10^{-3} and the gamma rate below 10^{-4} corresponding to the performance of the PEB5 (10 cm) – Lead (10 cm) shield.

Neutron population			
	d [cm] (2.5 MeV)	d [cm] (5 MeV)	d [cm] (10 MeV)
PELi (10cm), Lead	–	90	> 90
PELi (10cm), Copper	–	< 50	< 70
PEB5 (10cm), Lead	**–**	**–**	**60**
PEB5 (10cm), Copper	**–**	**–**	**< 30**
Gamma population			
	d [cm] (2.5 MeV)	d [cm] (5 MeV)	d [cm] (10 MeV)
PELi (10cm), Lead	< 10	< 25	> 90
PELi (10cm), Copper	< 20	< 50	70
PEB5 (10cm), Lead	**< 10**	**10**	**20**
PEB5 (10cm), Copper	15	< 20	< 35

No second layer is necessary for neutron energies $E \leq 5$ MeV for PEB5 or $E \leq 2.5$ MeV for PELi to reduce the neutron population down to 10^{-3}. For higher energies copper is the best choice. Regarding (n,γ) self-shielding effects, lead is recommendable. Especially for higher energies, lead performs better. Here, only 20 cm are needed compared to 35 cm for copper in combination with PEB5 for $E = 10$ MeV.
As already mentioned, a standard neutron shield is built of three layers: moderator, absorber and metal. In this study the moderator and the absorber were combined to one layer. Thus, doped PE is used. Furthermore, lead is used for gamma capture and attenuation purposes. Therefore, a standard neutron shield is complete. But even though, in regard to other important and already discussed background sources, especially ra-

dioactivity, copper is used as inner layer, the third layer.

For the determination of the thickness of the third layer, the simulation is comparable to the previous one determining the thickness of the first and second layer. The used GDML geometry consists of a 1 m thick block containing now three materials. Neutron beams with different initial energies were then also focused to the center of the block. Considered combinations were:

Lead (30 cm) – PEB5 (10 cm) – Copper (60 cm)
PEB5 (10 cm) – Lead (10 cm) – Copper (80 cm)
PEB5 (10 cm) – Lead (20 cm) – Copper (70 cm)

To investigate the order of the materials, a shield starting with lead instead of doped PE was added to the list. Furthermore, the thickness of lead as second layer is varied to satisfy neutron energies up to 10 MeV.

Figure 4.9a displays the neutron attenuation $N_{\text{n,norm,5 MeV}}$ for the three shield combinations. The shield with lead as first layer is very effective to reduce the neutron rate to 10^{-5} after 40 cm in total. Therefore, no third layer is necessary. In contrast, the combination does not reduce the photon rate sufficiently. In Figure 4.9b the photon population $N_{\gamma,\text{norm,5 MeV}}$ is depicted. At first, the gamma rate decreases down to 10^{-2}, increases again after 30 cm up to 0.2 in the PEB5 layer, resulting in a plateau near 10^{-4} after additional 20 cm of copper. The rise in the PEB5 layer can be explained by the cross section for radiative capture, which is larger for ^{10}B for moderated neutrons with smaller energies compared to the cross section for neutrons with initial energies of 5 MeV in ^{208}Pb.

For shields starting with PEB5, the neutron rate as well as the photon rate are reduced continuously. Here, a neutron population of less than 10^{-4} can be achieved with either 30 cm or 20 cm of copper depending on the thickness of the lead layer. Concerning the gamma rate no third layer is needed. Furthermore, for 20 cm of lead as second layer the gamma rate can be reduced down be 10^{-5}, but increases again in the copper layer due to radiative capture processes in copper. In Table 4.4 necessary thicknesses for the third layer are summarized for different initial energies compared to the performance of the PEB5 (10 cm) – Lead (20 cm) shield. Figures concerning other initial neutron energies can be found in Appendix C Figure C.5 – C.6.

Regarding an effective neutron attenuation and (n,γ) self-shielding effects the combination PEB5 (10 cm) – Lead (20 cm) is the best choice. Keeping in mind the measured neutron flux at LNGS, see Table 2.3, which indicates only few neutrons per cm^2 and second, 45 cm of copper should not be added to the shield. In Figure 4.10 the kinetic energy of neutrons and gammas after an additional 10 cm and 20 cm of copper is depicted. A thicker shield reduces the neutron population less than one order of magnitude, but the energy distribution is moved to lower energies from 0.30 MeV to 0.14 MeV calculated as average. The deviations in the spectra of the kinetic energy of the gamma population is minimal and dominated by statistical fluctuations. The gamma rate is reduced from

Table 4.4: Summarized are thicknesses of copper in combination with PEB5 and lead regarding
an effective neutron attenuation and (n,γ) self-absorbing effects with different initial
neutron energies $E_{n,sim}$ as third layer of a shield. The neutron rate is below 10^{-4}
and the gamma rate below 10^{-5} corresponding to the performance of the PEB5
(10 cm) – Lead (20 cm) shield

Neutron population			
	d [cm] (2.5 MeV)	d [cm] (5 MeV)	d [cm] (10 MeV)
PEB5 (10cm), Lead (10cm), Copper	–	30	35
PEB5 (10cm), Lead (20cm), Copper	–	20	< 30
Lead (30cm), PEB5 (10cm), Copper	–	–	–
Gamma population			
	d [cm] (2.5 MeV)	d [cm] (5 MeV)	d [cm] (10 MeV)
PEB5 (10cm), Lead (10cm), Copper	–	–	45
PEB5 (10cm), Lead (20cm), Copper	–	–	45
Lead (30cm), PEB5 (10cm), Copper	> 60	> 60	> 60

19 to 13 entries. The kinetic energy average 1.4 MeV after 10 cm of copper compared
to 2.1 MeV after 20 cm and thus, higher energetic gammas are emitted. Therefore, the
best performing combination is

<div align="center">

PEB5 (10 cm) – Lead (20 cm) – Copper (10 cm).

</div>

coming also to a compromise with compactness and cost-effectiveness.

In Section 5.14.2 the corresponding background rate of fast neutrons with the LNGS
fitting energy and angular distribution is calculated. Furthermore, the result is compared
to the one obtained with the previous shield design from the University of Warwick,
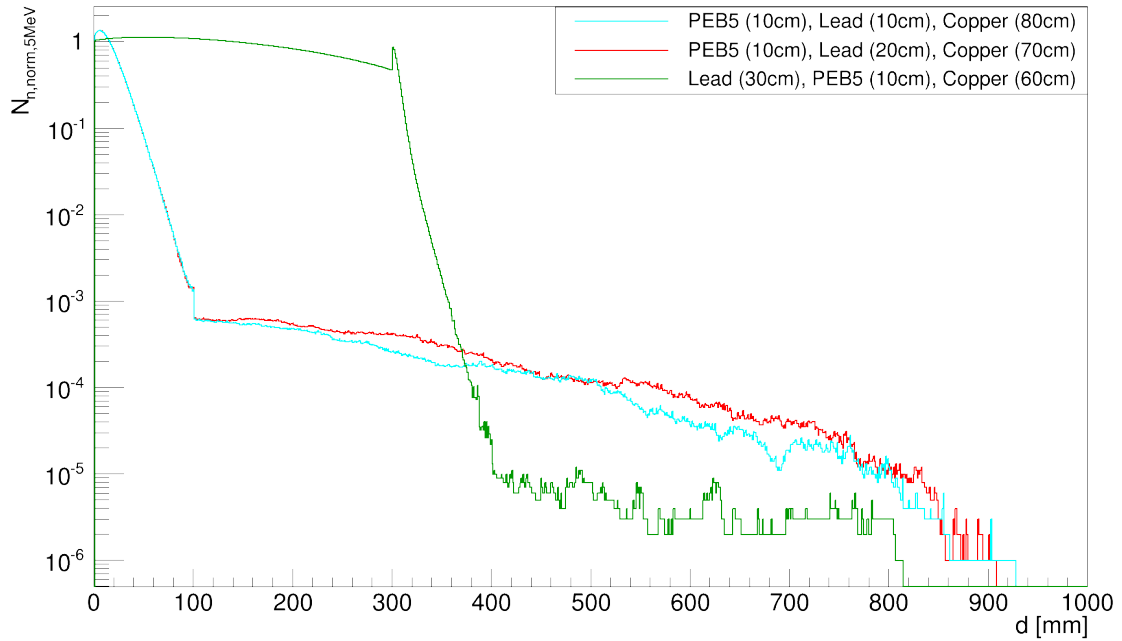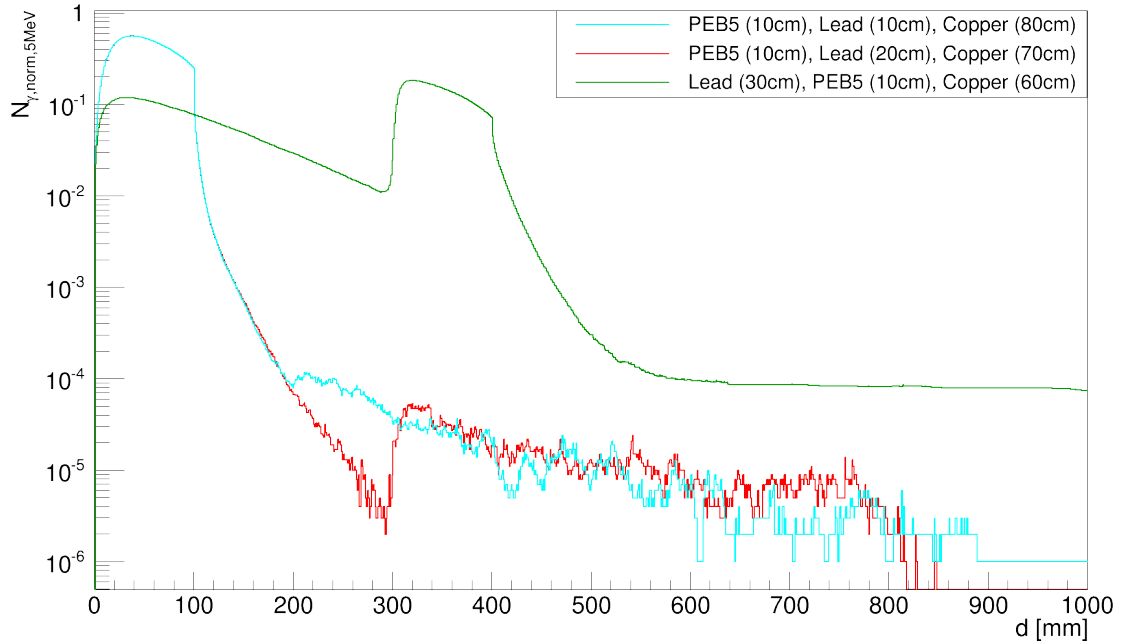introduced in Section 4.1.1.

(a) Neutron population $N_{\mathrm{n,norm,5\,MeV}}$ for three layer shields

(b) Gamma population $N_{\gamma,\mathrm{norm,5\,MeV}}$ for three layer shields

Figure 4.9: Plotted is the population for neutrons and gammas for an incident neutron energy of $E = 5\,\mathrm{MeV}$ in three layer shields. The shield with lead as first layer is very effective to reduce the neutron rate to 10^{-5}. No third layer is needed. But the photon population results in a plateau near 10^{-4}, after increasing in the PEB5 layer due to radiative capture. Shields starting with PEB5 reduce the neutron as well as the photon rate continuously.
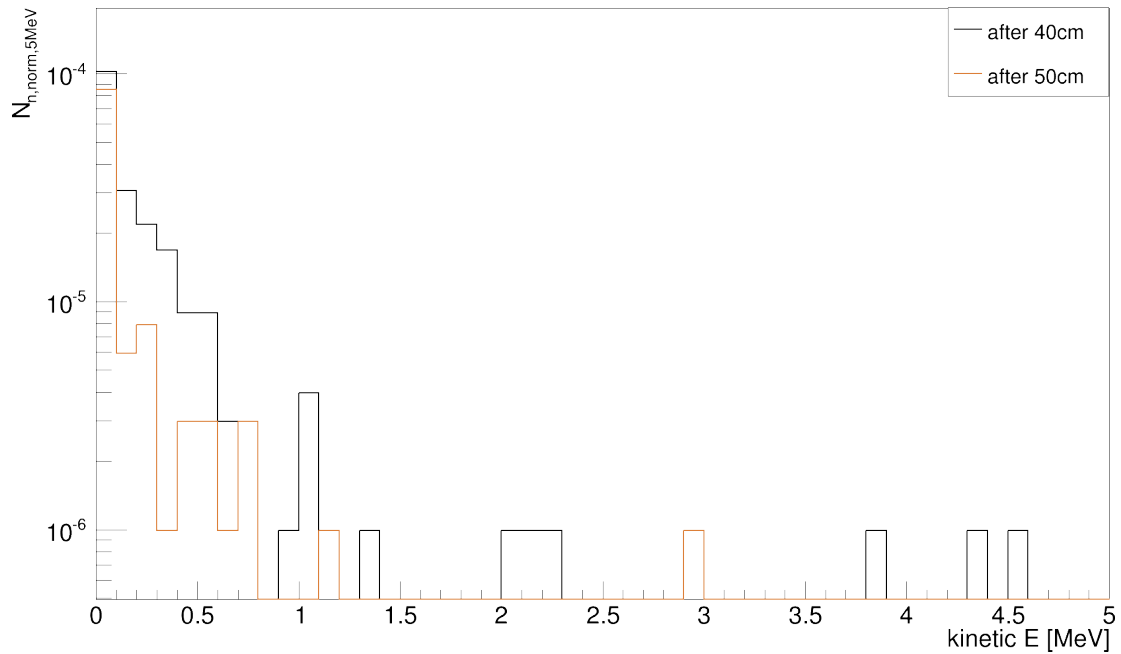
(a) Kinetic energy of neutrons
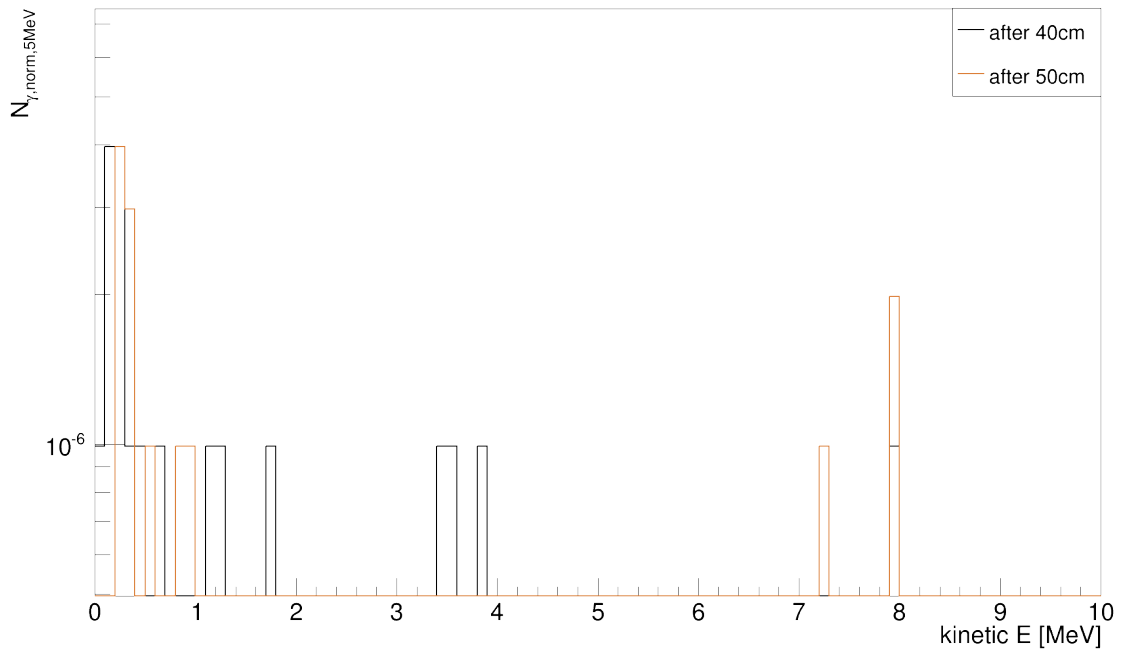
(b) Kinetic energy of gammas

Figure 4.10: Plotted is the kinetic energy for neutrons and gammas for an incident neutron energy of $E = 5\,\text{MeV}$ in a PEB5 $(10\,\text{cm})$ – Lead $(20\,\text{cm})$ – Copper shield after certain thicknesses. A thicker shield reduces the neutron less than on order of magnitude, but the energy distribution is moved to lower energies. Yet, higher energetic gammas are produced.

4.5 Active Component

COBRA will have to operate at an extremely low level of background, under 10^{-3} counts per keV, kg and year in the signal region. The developed radiation shield suppresses the hadronic component of cosmic radiation, particularly neutrons, and gamma radiation to a minimum, but does not shield against the cosmic muons. While they are minimal ionizing particles, they can pass through the whole shield depositing energy in the detectors. In addition, neutrons and therefore also photons can be produced in the shielding material itself. The only way to suppress this form of background is an active veto alongside the passive shield in the final design.

Instead of using plastic scintillators as an active veto, also the concept to immerse the detectors in liquid scintillator for operation is investigated [92]. Yet, no design is settled so far. Therefore, neither in VENOM nor in the performed simulation an active component is implemented. However, a possibility dealing with muons in the current status is the modular design of COBRA via multiplicity analysis. Thus, in further analysis of background events calculating the total background rate, this method is used. The contribution of muons to the expected total background rate is calculated in Section 5.14.1.

Chapter 5

Total Background Estimation

Due to cosmic radiation and the existence of natural radioactivity in the environment all radiation detectors have to fight background signals depending on the size and type of the detector and of the external shield. The magnitude of the background determines the minimum detectable radiation level. Therefore, it is significant to keep background low for low-level counting experiments like COBRA. The majority of radiation detectors are surrounded with an external shield and furthermore operated in a degree of isolation.

The strategy to get control on the background level consists of two components. First the background has to be reduced within or near the detector array. Next to a shield and a deep laboratory, a low inactive mass design for the setup is necessary and ultra-pure materials have to be used. Furthermore, all detectors and materials need a clean handling. During operation events can be identified as background events and thus rejected. Methods used while analysis are a sufficient good energy resolution, the array granularity, pulse shape information and time correlations.

In this section the determined shield for COBRA is simulated within the CO-BRA hut at the LNGS to calculate the background rate for different background sources and setup parts. In Section 5.1 the simulated geometry is presented detailedly for documentation reasons, followed by the description of the simulation, see Section 5.2, and the calculation of the individual background rates, see Section 5.3. Furthermore, contamination measurements are compared to the LNGS data in Section 5.4. From Section 5.5 the simulations of different background sources, setup parts and their results are shown.

5.1 The large scale COBRA Setup

In this section the large scale COBRA setup used as GDML geometry in the simulations is described. In Figure 5.1, the hut with the setup and the developed shield is schematically depicted. The hut has an area of 9280 mm × 3495 mm × 3600 mm. Due to a crane, which is mounted under the ceiling, the height is restricted to 2650 mm corresponding to the maximal lifting height. In the inner part of the setup, a cube with the size 95.5 cm × 90 cm × 85 cm is reserved for the detectors and electronics. In the GDML geometry the crane and electronics are not implemented, however, the height is also limited to the maximal lifting height.
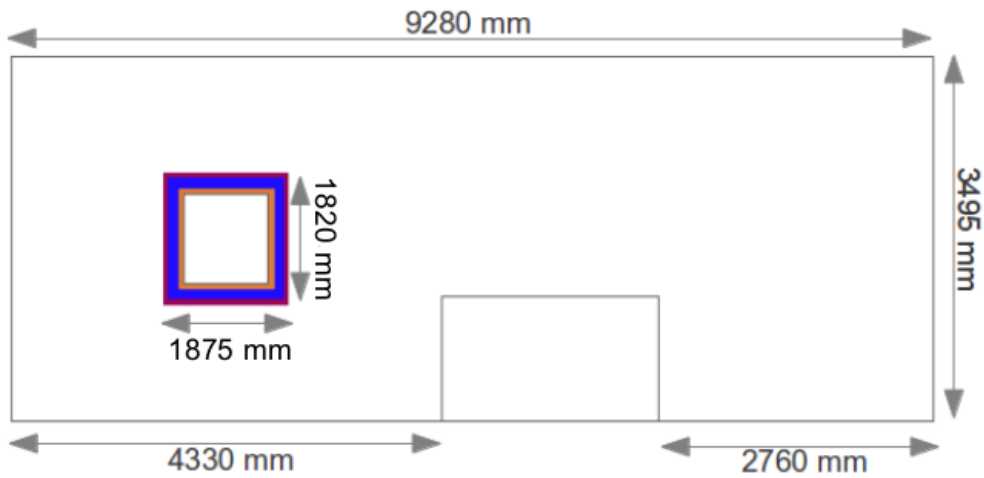

Figure 5.1: Schematically depicted is the COBRA hut at the LNGS with the setup and the shield. The hut has an area of 9280 mm × 3495 mm × 2650 mm. In the inner part of the setup, a cube with the size 95.5 cm × 90 cm × 85 cm is reserved for the detectors and electronics. The shield consists from inside to outside of 10 cm copper, 20 cm lead and 10 cm boron loaded polyethylene.

Altogether, 13824 detectors are simulated. One detector has a size of 2 cm × 2 cm × 1.5 cm and weighs of 36 g. The following details are taken into consideration in the GDML geometry and described in more detail: the cathode side of the detectors, the lacquer surrounding the detectors, the circuit boards (CB) for the anode readout and HV supply, the Delrin support structure and ASICs[1].
The cathode of the detectors is constructed out of an aluminum (0.08 μm) and a platinum (0.1 μm) layer. In addition, the surface of the detectors is covered with a Glyptal 1201 lacquer with a thickness of 10 μm. Hence, the dimension of the detectors in z is 1.502018 cm. In reality, the lacquer is not placed on all sides of the detectors and in addition, the thickness varies, because it is applied manually. Nine detectors are arranged in a holder, which is built out of three Delrin plates forming a support structure. The total holder has a size of 8.5 cm × 8.5 cm × 1.682018 cm. The top plate

---
[1]ASIC: Application-Specific Integrated Circuit

of the holder has a size of 8.5 cm × 8.5 cm × 0.2 cm and holds the detector in place at
the anode side. Gaps with a size of 2.002 cm × 2.002 cm are left to fit the detectors.
The distance between the detectors in x and y is 0.5 cm. The surrounding border has
a size of 0.75 cm. It is schematically depicted in Figure 5.2 on the right side. The
bottom plate has a thickness of 0.15 cm. The detectors are facing the bottom plate
with the cathode side. Gaps with a size of 1.0 cm × 1.0 cm enable the operation of the
cathode in the real experiment. Furthermore, a third Delrin plate with a thickness of
0.15 cm is also placed on top of the bottom plate holding the detectors in place at the
cathode side. Here, also gaps with a size of 2.002 cm × 2.002 cm are left. Accordingly,
all detectors are encircled with Delrin. In Figure 5.2 on the left side both bottom plates
of the Delrin holder are shown, one on top of the other. The bottom plate is made out
of one piece in reality, whereas in the GDML geometry it has to be build out of two, so
that the detectors can be arranged.

Next to the support structure parts, the high voltage supply can be identified in
Figure 5.2. It is built out of 50 μm Kapton and 50 μm copper. The nine HV plates have
a size of 1.8 cm × 1.8 cm with a 1.2 cm × 1.2 cm gap leaving a border of 0.2 cm Delrin.
The inner connections of single HV plates have a size of 0.2 cm × 0.7 cm, whereas the
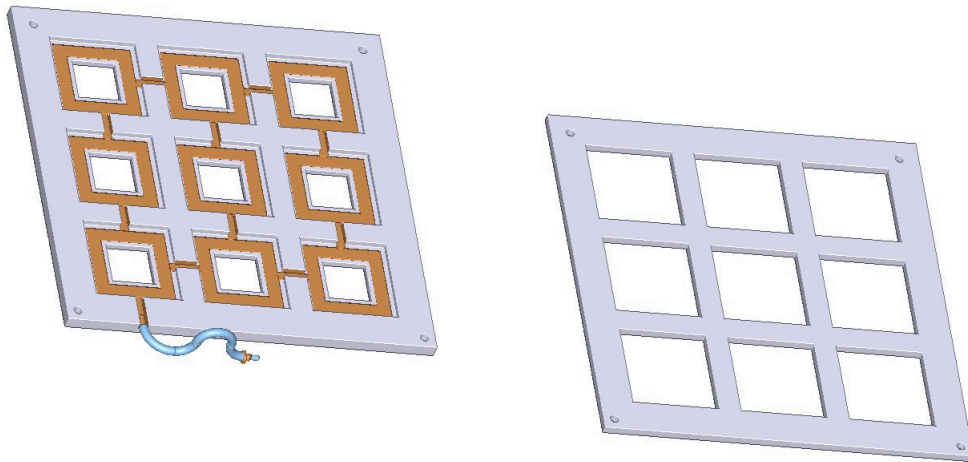outer connection has a size of 0.2 cm × 0.85 cm.

Figure 5.2: Schematically depicted is the Delrin support structure for one holder. The total
holder has a size of 8.5 cm × 8.5 cm × 1.812018 cm. The top plate (on the right
side), has a thickness of 0.2 cm. Gaps are left to fit the detectors. The bottom
plate (on the left side), has a in total thickness of 0.3 cm. In addition, the HV
voltage supply, which is mounted on the bottom plate, is shown. [93]

The complete holder is depicted in Figure 5.3. In addition, the Kapton cable for the
anode readout is applied. It has a thickness of 200 μm. The anode grids of the detectors,
also depicted in Figure 5.3, are not implemented in the simulations. The weight of one
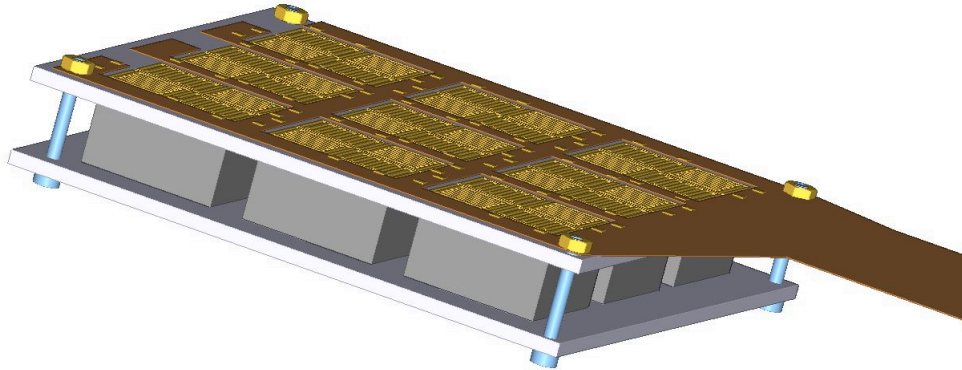complete holder is 285 g.

Figure 5.3: Schematically depicted is the complete holder. Nine detectors are arranged in one holder, supported by the Delrin structure. Furthermore, the Kapton cable for the anode readout is mounted on the top plate of the holder. [93]

Eight holders are aligned in a row, which is also built as a Delrin structure. The size of one row is $9.5 \, \text{cm} \times 90 \, \text{cm} \times 1.682018 \, \text{cm}$. There is no space between two holders in the GDML geometry, but a surrounding border out of Delrin with a thickness of $0.5 \, \text{cm}$. In front of the first holder in a row a $15 \, \text{cm}$ wide border is constructed holding the ASIC, which has a size of $1.388 \, \text{cm} \times 0.736 \, \text{cm} \times 0.1 \, \text{cm}$. Wires to connect the ASICs with the detectors are not implemented.

Eight rows are lined up in a shelf with a gap of $1.5 \, \text{cm}$ between two rows. In Figure 5.4 one shelf is schematically illustrated. Finally, 24 shelves are stacked with a distance of $1.5 \, \text{cm}$, building a cubic arrangement of the detectors for the inner part of the setup. At the bottom is a $2 \, \text{cm}$ gap between the first layer of the shield and the first shelf. With this configuration the total source mass is $498 \, \text{kg}$.

The inner part is surrounded by the developed shield, see Chapter 4. It consists of $10 \, \text{cm}$ radiopure copper, followed by $20 \, \text{cm}$ of lead. The outer layer is made of $10 \, \text{cm}$ boron loaded polyethylene. This configuration showed the best performance of effective attenuation of fast neutrons and (n,γ) self-shielding effects. The weight of the shield is $31041 \, \text{kg}$.

The whole setup has therefore a total volume of $1875 \times 1820 \times 1770 \, \text{mm}^3$ and a total mass of $31700 \, \text{kg}$.
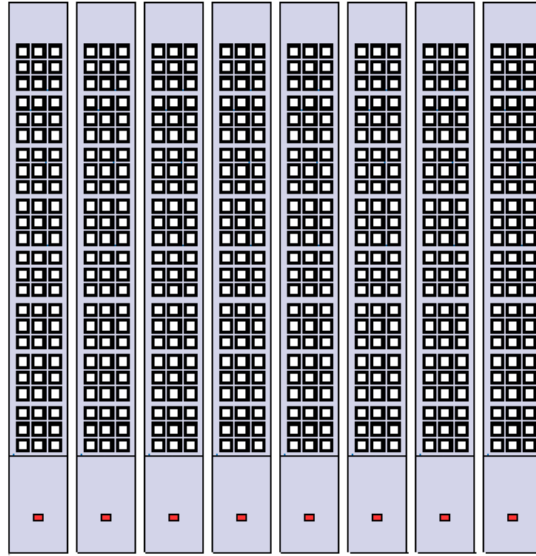
Figure 5.4: Schematically depicted is one shelf for the inner part of the setup. It consists of
the detectors (in white), the Delrin holders (in light grey) and ASICs (in red).
Altogether, 13824 detectors are arranged in 24 shelves. Nine detectors are
arranged in a holder, eight holders are aligned in a row and eight rows are lined
up in a shelf. Finally, 24 shelves are stacked. The ASICs are mounted on the
Delrin border of the rows.

5.2   Description of the Simulations

The simulations of the different background sources have to be distinguished. Here,
important criteria are energy and angular distributions. Nevertheless, three main groups
can be formed: single radioactive isotopes, thermal neutrons and high-energetic external
radiation sources, like neutrons and muons.

5.2.1   Single Radioactive Isotopes

The simulations of radioactive sources are all comparable. Individual radionuclei are
generated with a quantity of $1.01 \cdot 10^6$ events as intrinsic or surface source of different
setup parts with a randomly chosen starting position.

As decay chains the uranium, see Table 2.1, and thorium, see Table 2.2, series were
taken into consideration. Each isotope was simulated separately, but clustered into sev-
eral groups in the analysis, because it is reasonable to suppose that within the groups
the same activity of the single isotopes can be expected. The border between two
groups was set, if the half-lives of the affected isotopes can be distinguished by several
orders of magnitude, e.g. ^{234m}Pa with a half-life of 1.175 min and ^{234}U with a half-life
of $2.45 \cdot 10^5$ yr. In particular, for the uranium series four groups are created. The first
group includes ^{238}U, ^{234}Th and the metastable isotope ^{234m}Pa. The long-living isotopes

^{234}U and ^{230}Th are summarized in the second group. The third group consists of ^{226}Ra, ^{222}Rn, ^{218}Po, ^{214}Pb, ^{214}Bi and ^{214}Po. The last group comprises the radionuclei ^{210}Pb, ^{210}Bi and ^{210}Po and is also considered as surface source.

The simulation of the thorium series, see Table 2.2, was set equally. All isotopes are split into different groups. The first group includes only the isotope ^{232}Th, whereas the second one comprises the radionuclei ^{228}Ac plus ^{228}Ra and ^{228}Th. The third group consists of the isotopes ^{224}Ra, ^{220}Rn, ^{216}Po. Here, the last group summarizes the isotopes ^{212}Pb, ^{212}Bi, ^{212}Po and ^{208}Th.

From the third natural decay chain ^{235}U only the mother nuclide ^{235}U itself was considered. In addition, the isotopes ^{40}K, ^{137}Cs, ^{60}Co and, if necessary, cosmogenic isotopes are regarded. As setup parts the following segments are taken into consideration for intrinsic sources: all layers of the shield, the lacquer surrounding the detectors, the ASICs, the Delrin holder as well as the circuit boards. For surface simulations events were started on the surface of the lacquer, the holder, the cathode, and the circuit boards.

The last setup part for radioactive source is the gas. Although a constant nitrogen flushing is done in experimental operation, the influence of airborne source in the gas itself has to be controlled.

5.2.2 Thermal Neutrons

The shape of the neutron spectrum originating from spontaneous fission follows Watt spectrum:

$$N(E) = C \cdot e^{-\frac{E}{a}} \cdot \sinh\left((b \cdot E)^{\frac{1}{2}}\right), \tag{5.1}$$

with C is a normalization constant and plotted in Figure 5.5. The two coefficients a and b vary from one isotope to another. In this work the following values were used: $C = 1$, $a = 0.7124\,\text{MeV}$ and $b = 5.6405\,\text{MeV}^{-1}$ [94], convenient for ^{238}U.

Thus, fission-induced neutrons were generated following the Watt spectrum, Equation 5.1, with an isotropic angular distribution uniformly within the lacquer, Delrin, ASICs, CB of the HV supply and anode read-out and the shield layers.

Thermal neutrons originating from (α,n) reactions are already covered by the single radioactive isotopes simulations and hence, in the analysis integrated.
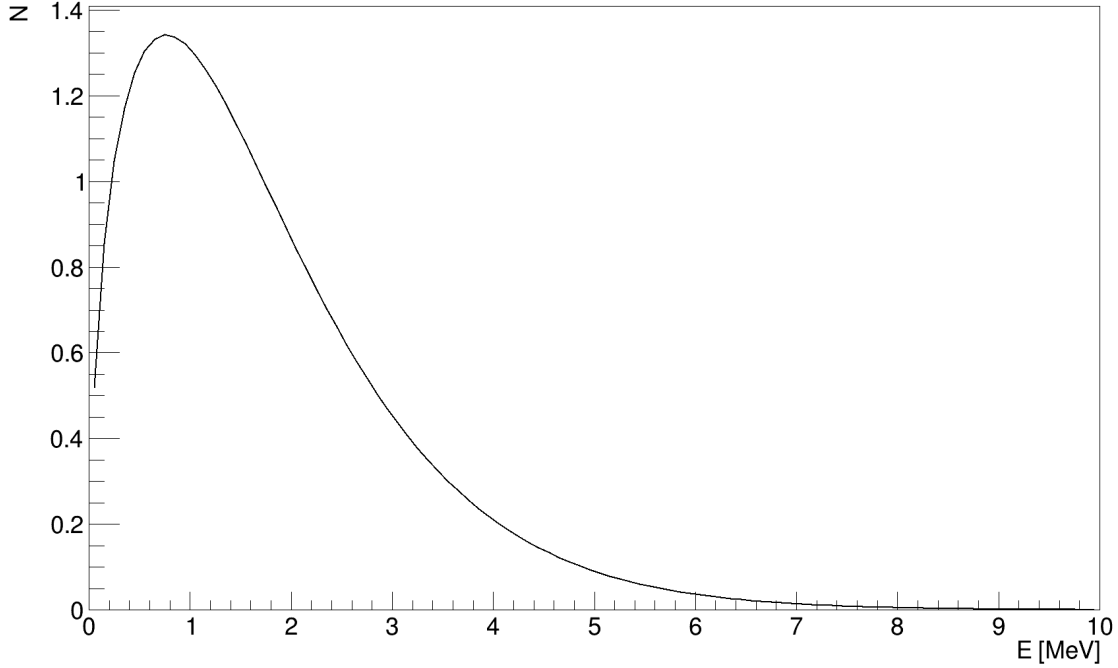
Figure 5.5: Plotted is the Watt spectrum with coefficient values of $C = 1$, $a = 0.7124\,\mathrm{MeV}$ and $b = 5.6405\,\mathrm{MeV}^{-1}$.

5.2.3   External Radiation Sources

As external radiation sources muons and muon-induced neutrons are taken into consideration. Both simulations are based on the results of [95].

The differential muon intensity corresponding to a slant-depth h is given by [95]

$$I(h) = (I_1 \cdot e^{\frac{-h}{\lambda_1}} + I_2 \cdot e^{\frac{-h}{\lambda_2}}), \tag{5.2}$$

with the free fitting parameters I_1, I_2, λ_1 and λ_2. For underground laboratories with a flat overburden (e.g. WIPP[2], Soudan[3]), the muon intensity I_{th} is

$$I_{th}(h, \theta) = I(h) \cdot G(h, \theta) \tag{5.3}$$

$$I_{th}(h, \theta) = (I_1 \cdot e^{\frac{-h}{\lambda_1}} + I_2 \cdot e^{\frac{-h}{\lambda_2}}) \cdot \sec\theta,$$

with $h = h_0 \cdot \sec\theta$ and h_0 is the vertical depth at a underground site with flat overburden. With the help of experimental data of the total muon flux and the knowledge of the vertical depth the fitting coefficients could be determined [95].

In case of a mountain overburden, additional information regarding the mountain shape is required. After integrating over the mountain shape, it is possible to enter the result into Equation 5.3 determining an equivalent vertical depth h_0 relative to a flat

---

[2]WIPP: Waste Isolation Pilot Plant, USA
[3]Soudan: Soudan Underground Mine State Park, USA

overburden for the Gran Sasso Laboratory, leading to [95]

$$h_0 = (3.1 \pm 0.2)\,\text{km w.e..} \tag{5.4}$$

In Table 5.1a the used fitting parameters for the angular distribution, see Equation 5.3, are summarized.

The energy distribution is given by [95]

$$\frac{dN}{dE_\mu} = A \cdot e^{-b \cdot h(\gamma_\mu - 1)} \cdot (E_\mu + \epsilon_\mu \cdot (1 - e^{-b \cdot h}))^{-\gamma_\mu}, \tag{5.5}$$

where A is a normalization constant and E_μ is the muon energy after passing the rock slant depth h. In Table 5.1b the used fitting parameters are shown. In addition, the measured muon energy E_μ is given [96]. In Figure 5.6a the energy distribution is plotted.

Table 5.1: Tabulated are the fitting parameters for the energy and angular distribution for the muon simulation [95, 96].

(a) Angular distribution

I_1 [cm^{-2}s^{-1}]	I_2 [cm^{-2}s^{-1}]	λ_1 [km w.e.]	λ_2 [km w.e.]	h_0 [km w.e.]	E_μ [GeV]
$67.97 \cdot 10^{-6}$	$2.071 \cdot 10^{-6}$	0.285	0.698.	3.1	270

(b) Energy distribution

A	b [km w.e.$^{-1}$]	γ_μ	ϵ_μ [GeV]
1	0.4	3.77	693

Attention was also given to the muon-induced fast neutron activity for different underground sites. The neutron flux ϕ_n as a function of depth was determined. With a fit function of the form

$$\phi_n = P_0 \frac{P_1}{h_0} \exp \frac{-h_0}{P_1} \tag{5.6}$$

with an equivalent vertical depth $h_0 = 3,1$ km w.e. relative to a flat overburden and the fit parameters $P_0 = (4.0 \pm 1.1) \cdot 10^{-7}\,\text{cm}^{-2}\,\text{s}^{-1}$ and $P_1 = (0.86 \pm 0.05)\,\text{km w.e.}$ the total neutron flux for the LNGS was calculated to be

$$\phi_n = (3.0 \pm 0.7) \cdot 10^{-9}\,\text{cm}^{-2}\,\text{s}^{-1}\,\text{[95].} \tag{5.7}$$

The neutron energy spectrum was derived from FLUKA[4] simulation leading to a convenient parametrization based upon the following fitting function

$$\frac{dN}{dE_n} = A_\mu \left(\frac{e^{-a_0 E_n}}{E_n} + B_\mu(E_\mu) \cdot e^{-a_1 E_n} \right) + a_2 E_n^{-a_3}, \tag{5.8}$$

---

[4]FLUKA: Flukturierende Kaskade, MC simulation package

where E_n is the neutron energy, a_i (i$=$0,1,2,3) are fitting parameters, A_μ is a normalization constant and $B_\mu(E_\mu)$ is the function of muon energy with E_μ in GeV ,

$$B_\mu(E_\mu) = 0.324 - 0.641 \cdot e^{-0.014 \cdot E_\mu} \text{ [95].} \tag{5.9}$$

This parametrization is valid for neutron energy $E_n > 10\,\text{MeV}$. In Figure 5.6b the energy distribution is plotted. The angular distribution of neutrons is parametrized according to

$$\frac{dN}{d\cos\theta} = \frac{A_\theta}{(1 - \cos\theta)^{B_\theta(E_\mu)} + C_\theta(E_\mu)}. \tag{5.10}$$

A_θ is a constant. The functions B_θ and C_θ are

$$B_\theta(E_\mu) = 0.482 \cdot E_\mu^{0.045} \tag{5.11}$$

$$C_\theta(E_\mu) = 0.832 \cdot E_\mu^{-0.152} \text{ [95].} \tag{5.12}$$

In Table 5.2 the used fitting parameters are summarized. The individual events for both simulations were generated on the outer surface of the polyethylene layer of the shield, see Figure 5.1. The starting position was randomly chosen.

Table 5.2: Summarized are the fitting parameters for the energy and angular distribution of the muon-induced neutron simulation [95].

A_μ	A_θ	a_0	a_1	a_2	a_3
1	1	7.828	2.23	$-7.505 \cdot 10^{-15}$	2.831
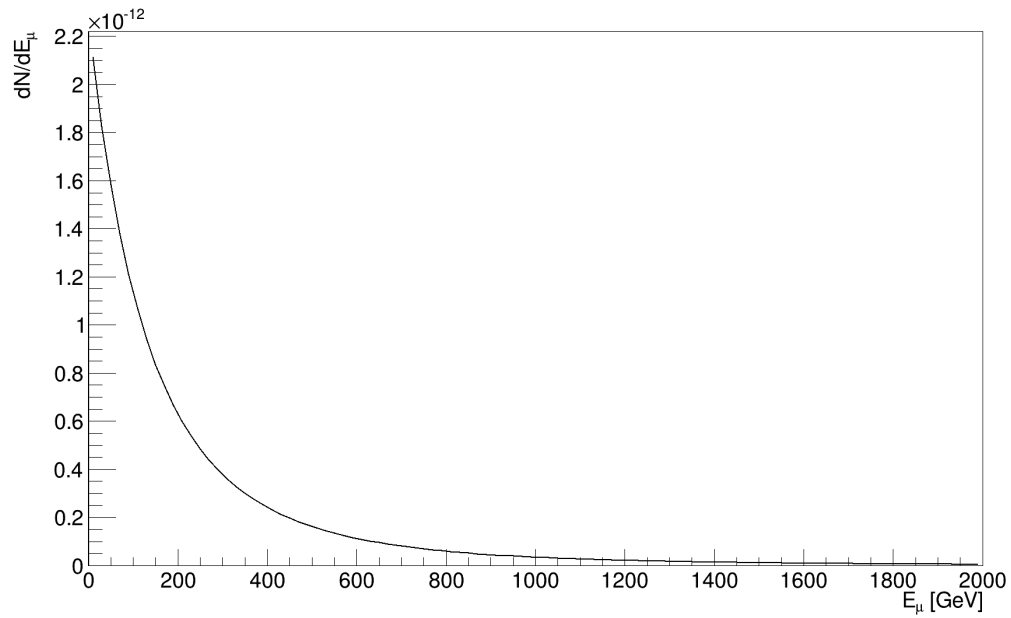
(a) Muon energy spectrum
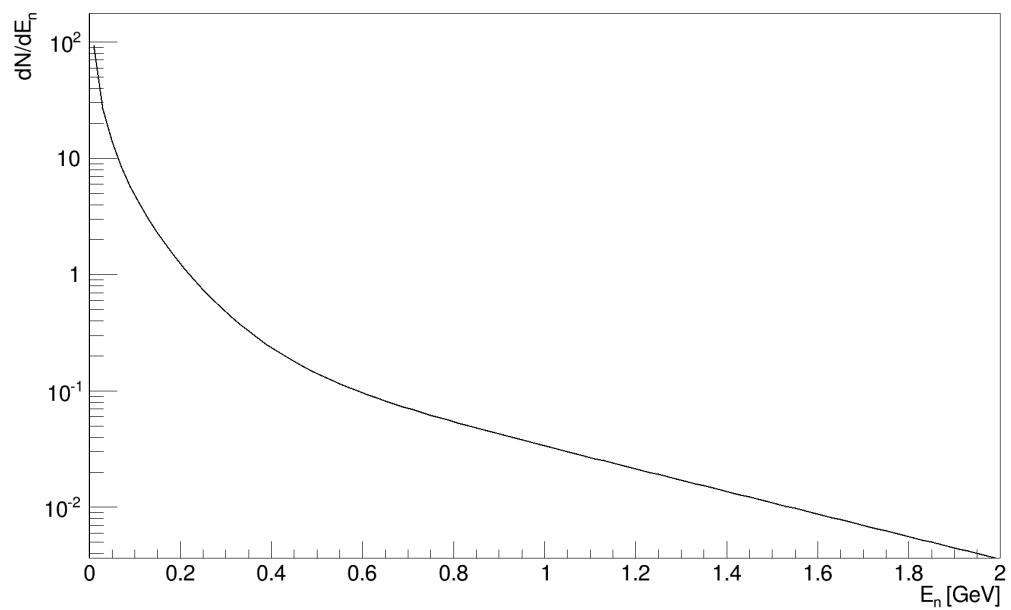
(b) Neutron energy spectrum

Figure 5.6: Plotted are the spectra of the muon and neutron energy local to the LNGS underground site.

5.3   Calculation of the Background Rate

In the analysis of the individual simulations the background rate is calculated using

$$B = \frac{N_{CUTS}}{m \cdot \Delta E \cdot t}. \tag{5.13}$$

Here, N_{CUTS} indicates all events, which survived multiple cuts. One crucial cut is the energy (ROI) cut. The Q-value of ^{116}Cd is 2.814 MeV and the interval defining the ROI is given by the Q-value as mean µ and a known standard deviation σ, which depends on the energy resolution ΔE, by µ ± σ. The energy resolution is assumed to be 2 % FWHM at the Q-value resulting in

$$\Delta E = 0.02 \cdot 2.814 \, \text{MeV} = 56 \, \text{keV}. \tag{5.14}$$

Thus, the standard deviation is given by

$$\sigma = \frac{\Delta E}{2.355} = 24 \, \text{keV}. \tag{5.15}$$

In Section 3.4 the energy resolutions of operated detectors at the demonstrator setup were shown. The median value is 1.5 %FWHM. Hence, the assumed energy resolution for the calculation of the background rate is an upper limit. The mass m is calculated via

$$\begin{aligned} m &= m_{det} \cdot N_{det} \\ &= 36 \, \text{g} \cdot (3 \cdot 3 \cdot 8 \cdot 8 \cdot 24) \\ &= 498 \, \text{kg} \end{aligned} \tag{5.16}$$

with the mass of one detector m_{det}, the number of simulated detectors N_{det}. The last quantity is the measuring time t, which depends on the expected activity A in Bq/kg and is computed via

$$t = \frac{N_{sim}}{A \cdot m_{mat}} \tag{5.17}$$

taking into account the number of simulated events N_{sim} and the mass of the material m_{mat}, in which the simulated events were generated. For surface sources, e.g. on the surface of the holders or lacquer, the measuring time is calculated using

$$t = \frac{N_{sim}}{A \cdot a_{mat}} \tag{5.18}$$

with the surface a_{mat}, on which the events were started. The assumed activity A has now the unit Bq/cm^2.

In Table 5.3 the masses m_{mat}, the density ρ_{mat} and the size of the surface a_{mat} of the used materials in the simulations and subsequently in the analysis are summarized.

Table 5.3: Summarized are the densities of ρ_{mat} and the masses m_{mat} of the used materials in the simulation and the analysis to calculate the background rate.

	ρ_{mat} [g/cm^3]	m_{mat} [kg]	a_{mat} [cm^2]
CdZnTe	5.78	498	–
Cathode	21.43	$11.8 \cdot 10^{-3}$	110592
Lacquer	1.4	0.39	280627
Delrin	1.411	48	391373
CB HV	Kapton: 1.4 / Cu: 8.92	1.408	113050
CB Anode	1.4	1.2	–
ASICs	–	110.3	–
Gas	1.251	0.84	–
Cu	8.92	5383	–
Pb	11.324	23193	–
B5PE	1.6	2465	–

Next to the already applied ROI cut, four further cuts are used for N_{CUTS} corresponding to the LNGS data analysis. The first cut regards the multiplicity of detectors registering events. Only events, which interact with only one single detector are used. Therefore, the cut is called single detector event (SDE) cut. The second cut deals with the interaction depth. In the simulation the detectors are subdivided into 150 1 mm thick bins in z. In addition, a resolution in z is applied with $\Delta z = 1$ mm. Only events with $z > 2$ and $z < 149$ are considered to calculate B neglecting the four bins, two on top and bottom side of the detectors building a fiducial volume. The third cut regards events on the lateral surfaces (LSE) of the detectors. Since the pulse shapes are not recorded in the simulation, the developed LSE cut [89] for the LNGS data analysis cannot be applied. Nevertheless, the LSE cut affects mostly α particles with a current efficiency of 75 %. In the simulation the particle type is saved for each event depositing energy. Therefore, 75 % of α events are neglected to calculate B. However, it has to kept in mind, that the LSE cut cannot be applied to all simulations, e.g. the intrinsic contamination of CdZnTe detectors. Furthermore, in the LNGS data analysis a multi-side (MSE) cut is used. The distinction between multi-side and single-side (SSE) events cannot be applied, because the simulation is not sensitive to such events. However, the MSE cut affects mostly γ particles with an efficiency of 90 % in the ROI [97]. Thus, 90 % of γ events are neglected for the calculation of B. The MSE cut depends on the energy. The full energy peak of a gamma line has for example a high fraction of multi-side events, whereas the Compton edge as well as the single and double escape peak are almost always single-side events. Therefore, it is only applied in the ROI and furthermore, isotopes emitting γ particles with a higher energy than the Q-value were neglected. Due to the drop in the intensity of gamma lines beyond the ^{208}Tl line at 2.615 MeV, this assumption is reasonable. In Table 5.4 the cuts used are summarized.

Table 5.4: Summarized are the cuts used to calculate the background rate

Cut	Name	Description
SDE	Single detector events cut	Only events, which interact with one single detector are regarded.
z	Fiducial volume cut	Four bins are neglected in z: $2 < z < 149$.
LSE	Lateral surface events cut	α particles are neglected with a efficiency of 75 %. Cannot be applied to all simulations!
MSE	Multi-side event cut	γ particle are neglected with a efficiency of 90 % in the ROI only.

The variables N_{sim} and N_{CUTS} are Poisson distributed, thus their standard deviation is given by the square root. An error for the measuring time t and the background rate B is calculated via propagation of uncertainty and is therefore based on the statistic. If $N_{CUTS} < 20$ an upper limit via the Feldman-Cousins method [98] with a 90 % confidence level is calculated, instead of the standard deviation.

In sum, see Section 5.15, the total background rate should be in the order of $10^{-3} \frac{\text{Entries}}{\text{kg·keV·yr}}$ corresponding to an effective Majorana mass of $\langle m_{\beta\beta} \rangle \approx 0.05\,\text{eV}$ to be competitive with other next-generation experiments and to reach the inverse mass hierarchy, see Figure 2.6.

5.4 Comparison with LNGS Data

A crucial factor to determine the total background rate is the activity of the different background sources in different setup parts. For many parts contamination measurements were performed using mass or gamma ray spectroscopy. Furthermore, the ILIAS[5] database offer a collection of contamination measurements from many experiments. However, often the instrumentation used is not sensitive enough to detect low counting rates and thus, most measurements are upper limits.

For setup parts, which are already worked with in the demonstrator setup at LNGS it is also possible to determine upper limits on the contaminations with the measured data and compare them with the contamination measurements. Feasible detector parts are the detector material CdZnTe itself, the cathode, the Glyptal lacquer and the Delrin support structure.

The measured data with the demonstrator setup was introduced in Section 3.4. As already mentioned, the main contamination in the ROI originates from α sources. Furthermore, two prominent peaks corresponding to ^{190}Pt and ^{210}Po could be identified at the cathode side.

To determine upper limits on contaminations from the LNGS data, first, the activity of known sources has to be calculated. Therefore, a GDML geometry referring to one holder of the demonstrator setup is created. The following detector parts are implemented: 16 1 cm^3 detectors, the lacquer surrounding the detectors, the cathode and the Delrin support structure. The support structure consists of two plates, with a thickness of 1 mm at the anode side (top plate) and 2 mm at the cathode (bottom plate). The whole holder has a size of $7.6{\times}7.6{\times}10\,\text{mm}^3$. The lacquer has a thickness of 10 µm. Figure 5.7 illustrates schematically the GDML geometry for a 4×4 holder.

^{190}Pt and ^{210}Po are generated individually on the surface of the cathode and the obtained spectra normalized to the exposure of 84.376 kg·d. Hereby, an expected activity A_{exp} of 1 mBq for ^{210}Po and an expected contamination c_{exp} of 0.01 % for ^{190}Pt is used. Furthermore, the LNGS data is prepared with a z cut guaranteeing only events from the cathode side: $0.98 < z < 1.02$. Other cuts, like the energy, LSE or MSE cut are not used. In a second step, the normalized spectra obtained from the simulations are compared to the LNGS data and scaled with a factor k so that the bins with the maximal number of entries in the peak region have the same heights. Thus, an upper limit can be calculated for a more reliable activity A_{ana} or contamination c_{ana} for the analysis concerning the background rate, because they also scale with k in a form

$$A_{ana} \leq k \cdot A_{exp} \tag{5.19}$$
$$c_{ana} \leq k \cdot c_{exp}.$$

In Figure 5.8 the spectrum of the LNGS data with the z cut is plotted in combination

---

[5]ILIAS: Integrated Large Infrastructures for Astroparticle Science

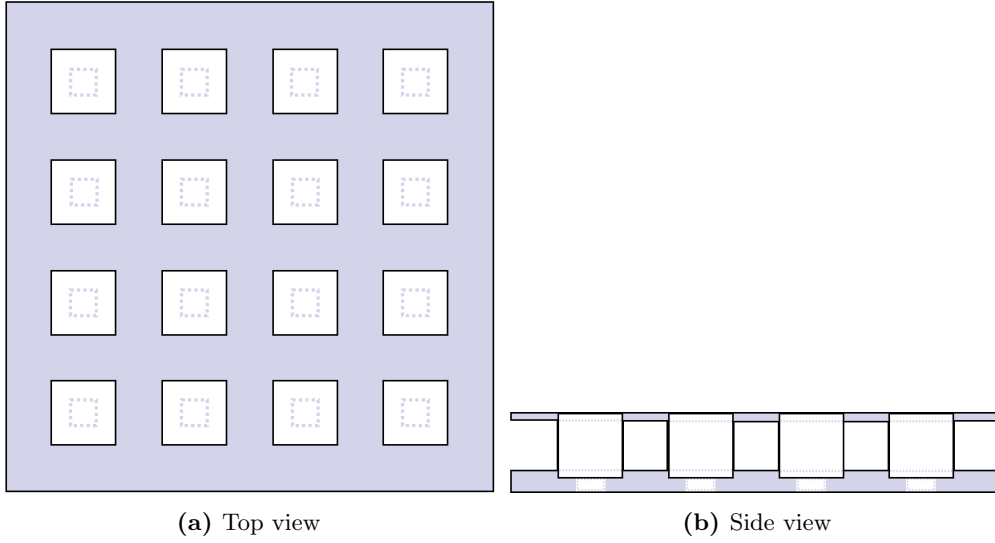**(a)** Top view   **(b)** Side view

Figure 5.7: Schematically depicted is the GDML geometry for the 4×4 holder MC to compare
with the LNGS data. 16 1 cm^3 detectors are arranged in a Delrin support structure.
On the left side the 4×4 holder is shown in top view. Dotted light gray indicate
holes in the bottom plate of the Delrin to operate the cathode. On the right side,
the holder is illustrated in side view. Here, dotted light gray lines show the Delrin
between the detectors.

with the simulated spectra of ^{190}Pt and ^{210}Po. It is shown, that the position of the α
peaks in the LNGS data and the MC fit to each other. The difference in the peak width
can be explained by the thickness of the lacquer surrounding the detectors. In reality,
it is applied manually. Therefore, the thickness varies with a mean value of 40 µm,
whereas in the MC the thickness is constant with a value of 10 µm. The scaling factor k
is $k = 0.04$ for ^{190}Pt and $k = 361$ for ^{210}Po. Thus, the upper limit on the contamination
or activity is $c_{ana} \leq 40$ ppm for ^{190}Pt and $A_{ana} \leq 361$ mBq/kg.

Another α peak can be identified at 6.4 MeV, depicted in Figure 5.9. This peak also
originates from ^{190}Pt, but at the anode side. Because of the comb-shape structure of
the anode and the specific recorded pulse shape for anode near events the deposited
energy is doubled [99]. To determine the contamination of ^{190}Pt at the anode side,
the deposited energy was doubled afterwards in the analysis, because pulse shapes are
not implemented in the MC. Furthermore, the same mass and contamination as for the
cathode was expected. A scaling factor k was determined to be $k = 0.17$, hence, a
contamination of $c_{ana} \leq 17$ ppm was calculated.
For the further analysis and the determination of upper limits of activities or contami-
nation from other detector parts the LNGS data is corrected by the already calculated
values in a way that a constant exponential falling background spectrum remains, which
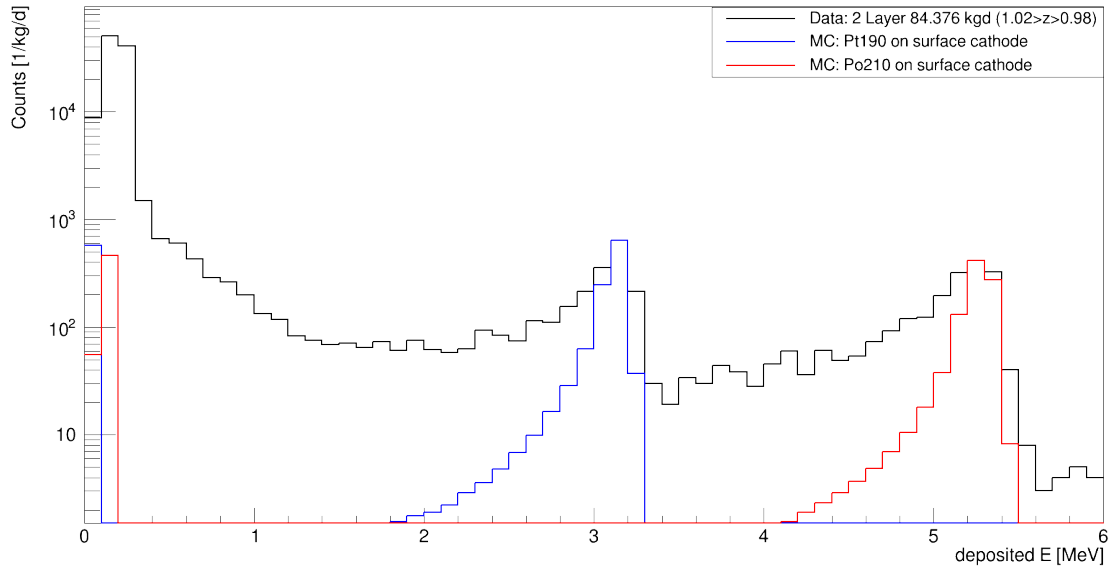is plotted in Figure 5.9. It can also be seen, that the ^{210}Po is not removed completely

Figure 5.8: Plotted are the spectra of LNGS data at the cathode side with ^{190}Pt and ^{210}Po obtained from MC. The peak heights were fitted with the help of the scaling factor k. The peak width varies due to the distinctive thickness of the lacquer of the detectors, whereas in the MC a default thickness of $10\,\mu$m is employed.

referring to either a different thickness of the lacquer or other detector parts ^{210}Po is located.
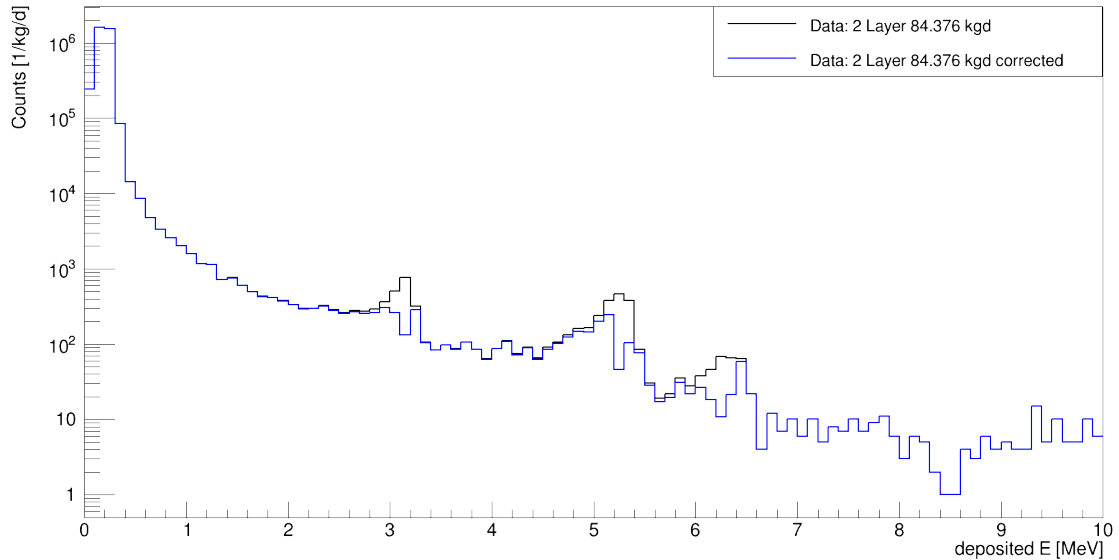

Figure 5.9: Plotted is the (corrected) spectrum of the LNGS data. Determined background sources originating from the cathode and anode were subtracted so that a constant exponential falling background spectrum remains. The ^{210}Po peak at $5.3\,$MeV is not removed completely.

With the corrected spectrum of the LNGS data, it is now possible to determine scaling factors for other setup parts next to the cathode and anode. But, as already mentioned, not all setup parts can be regarded, only the detector material, the gas, the lacquer and the Delrin support structure. For each part the obtained spectra of the uranium and thorium series simulation as well as other radionuclei was compared to the corrected LNGS data working out scaling factors.

The advantage of this analysis method is, that it is very conservative way to determine upper limits, because overlaid background sources are not considered. Thus, an underestimation of contaminations is hardly possible. In addition, only statistically relevant bins with more than 20 entries are used.

The expected activities A_{exp} or contamination levels c_{exp}, which are starting values for the analysis are based on measurements and can be found in Appendix B. Table 5.5 and 5.6 summarize all results.

The difference between the results from the contamination measurements and upper limits on the activities A_{ana} or contamination levels c_{ana} determined by the discussed method is remarkable due to the limited sensitivity of the instrumentation. For the detector material the upper limits of contamination values could be decreased by several orders of magnitude. Thus, CdZnTe can be indeed produced radiopure. In addition, radionuclei, which do not belong to a decay chain, can be neglected completely due to contaminations in the order of $< 10^{-23}$. The same was determined for the Glyptal lacquer and Delrin. For the lacquer a maximal reduction of a factor $< 10^{-3}$ was computed, whereas for Delrin also scaling factors in the order of $< 10^{-5}$ were calculated.

The new calculated activities A_{ana} and contaminations c_{ana} are further employed to calculate the measuring time via Equation 5.17 and the individual background rates with Equation 5.13.

There are two further possibilities to maybe improve the method used, but are not regarded in this thesis. First detectors with a higher background rate could be neglected. Figure 5.10 illustrates the counting rate for events with an deposited energy larger than $2\,\mathrm{MeV}$ per detector. Especially detector number 19, next to detector number 1, 5, and 12, shows a higher counting rate. It could be presumed that those detectors are not representative and by neglecting them the calculation of A_{ana} and c_{ana} is more reliable. However, the current method is more conservative and an underestimation is prevented by taking all detectors into consideration.

By considering a additional constant background beside the simulated radionuclide, e.g. ^{190}Pt, the fitting to the LNGS data would be more realistic leading also to a better corrected LNGS spectrum. Furthermore, the determination of the scaling factor k can be enhanced by choosing an interval, instead of the maximal bin. Here, the χ^2 method

[100] has to be used:

$$\chi^2 = \sum_i \frac{(N_{data,i} - k \cdot N_{sim,i})^2}{N_{data,i}} \tag{5.20}$$

with the number of bins i, the number of entries in the LNGS data $N_{data,i}$ and the number of entries in the simulation $N_{sim,i}$ in bin i.
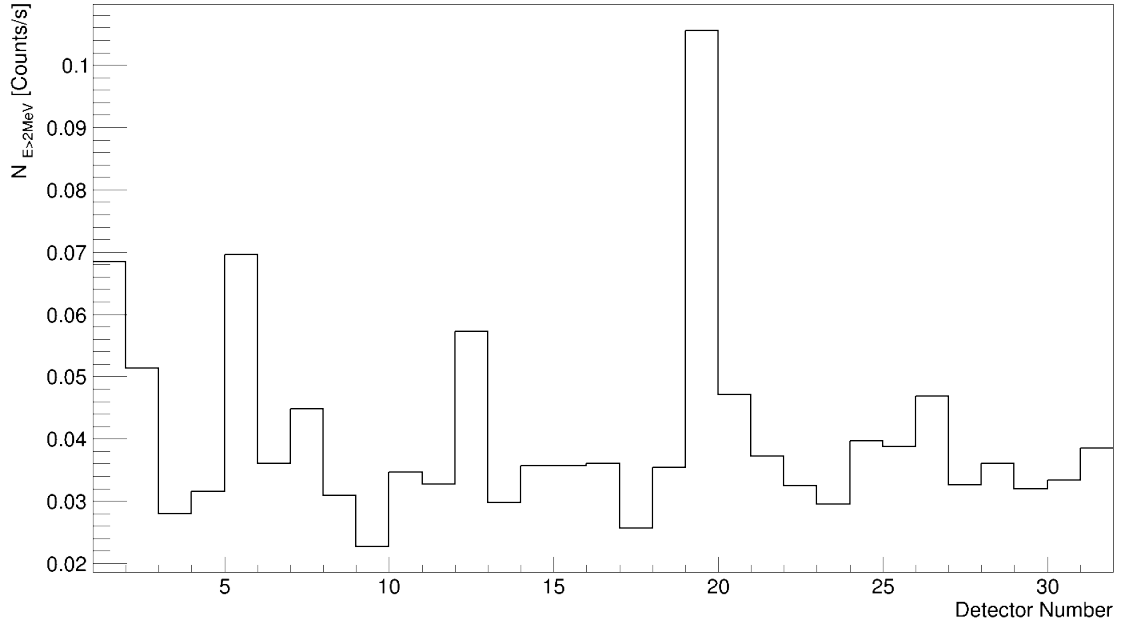

Figure 5.10: Shown is the counting rate for events with an deposited energy higher than 2 MeV per detector of the LNGS data. In particular, shows a much higher rate. By neglecting not representative detectors, A_{ana} and c_{ana} can be improved.

Table 5.5: Summarized are calculated activities from LNGS data concerning the cathode, the
CB of the anode and the detector material CdZnte itself.

		A_{exp} [mBq/kg]	c_{exp}	k	A_{ana} [mBq/kg]	c_{ana}
Cathode	^{222}Rn	1	–	60.1	60.1	
	^{210}Po	1	–	361	361	
	^{190}Pt	–	0.01 %	0.04	–	0.004 %
CB Anode	^{190}Pt	–	0.01 %	0.17	–	0.0017 %
CdZnTe	^{238}U	< 210	–	$3.13 \cdot 10^{-6}$	–	$657 \cdot 10^{-6}$
	^{234}U	< 1200	–	$1.11 \cdot 10^{-6}$	$1332 \cdot 10^{-6}$	–
	^{230}Th	< 1200	–	$9.9 \cdot 10^{-7}$	$1188 \cdot 10^{-6}$	–
	^{226}Ra	< 51	–	$2.96 \cdot 10^{-5}$	$151 \cdot 10^{-5}$	–
	^{222}Rn	< 51	–	$5.19 \cdot 10^{-6}$	$265 \cdot 10^{-6}$	–
	^{218}Po	< 51	–	$4.43 \cdot 10^{-6}$	$226 \cdot 10^{-6}$	–
	^{214}Po	< 51	–	$2.77 \cdot 10^{-6}$	$141 \cdot 10^{-6}$	–
	^{210}Po	< 51	–	$1.97 \cdot 10^{-5}$	$1 \cdot 10^{-3}$	–
	^{232}Th	< 47	–	$1.83 \cdot 10^{-5}$	$86 \cdot 10^{-5}$	–
	^{228}Th	< 60	–	$5.31 \cdot 10^{-6}$	$319 \cdot 10^{-6}$	–
	^{224}Ra	< 60	–	$3.95 \cdot 10^{-6}$	$237 \cdot 10^{-6}$	–
	^{220}Rn	< 60	–	$5.66 \cdot 10^{-6}$	$340 \cdot 10^{-6}$	–
	^{216}Po	< 60	–	$1.87 \cdot 10^{-6}$	$112 \cdot 10^{-6}$	–
	^{212}Po	< 60	–	$9.4 \cdot 10^{-7}$	$564 \cdot 10^{-7}$	–
	^{60}Co	< 19	–	0.02	0.38	–
	^{9}Li	–	< 5.3 ppb	10^{-22}	–	$5.3 \cdot 10^{-31}$
	^{23}Mg	–	97 ppb	10^{-21}	–	$97 \cdot 10^{-30}$
	^{23}Na	–	97 ppb	10^{-20}	–	$97 \cdot 10^{-29}$
	^{60}Cu	–	28 ppb	10^{-27}	–	$28 \cdot 10^{-36}$
	^{66}Ga	–	1.1 %	10^{-21}	–	$1.1 \cdot 10^{-23}$
	^{82}As	–	440 ppb	10^{-22}	–	$440 \cdot 10^{-31}$
	^{140}La	–	97 ppb	10^{-16}	–	$97 \cdot 10^{-25}$
	^{140}Pr	–	97 ppb	10^{-19}	–	$97 \cdot 10^{-28}$
	^{166}Tm	–	46 ppb	10^{-16}	–	$46 \cdot 10^{-25}$
	^{202}Au	–	< 5 ppb	10^{-19}	–	$5 \cdot 10^{-28}$

Table 5.6: Summarized are calculated activities from LNGS data concerning the Glyptal lacquer and the Delrin support structure

		A_{exp} [mBq/kg]	k	A_{ana} [mBq/kg]
Glyptal Lacquer	^{238}U	< 1500	0.02	< 30
	^{234}U	< 4300	0.004	< 17.4
	^{230}Th	< 4300	0.005	< 21.5
	^{226}Ra	< 140	0.16	< 22.4
	^{222}Rn	< 140	0.24	< 33.6
	^{218}Po	< 140	0.05	< 7
	^{214}Po	< 140	0.01	< 1.4
	^{210}Po	< 140	0.42	< 58.8
	^{210}Po sur	< 140	0.09	< 12.6
	^{222}Rn sur	< 140	0.13	< 18.2
	^{232}Th	< 180	0.17	< 30.6
	^{228}Th	< 190	0.07	< 13.3
	^{224}Ra	< 190	0.06	< 11.4
	^{220}Rn	< 190	0.04	< 7.6
	^{216}Po	< 190	0.005	< 0.95
	^{212}Po	< 190	0.001	< 0.19
Delrin support structure	^{222}Rn	< 5	0.2	< 0.1
	^{210}Po	< 200	$1.28 \cdot 10^{-5}$	< 0.003
	^{210}Po sur	< 200	$4.87 \cdot 10^{-6}$	$< 9.74 \cdot 10^{-4}$
	^{222}Rn sur	< 5	0.09	0.45

5.5   Results: CdZnTe Detectors

The source material of COBRA is CdZnTe. Although it is said, that it can be produced radiopure, radionuclei including natural radioactivity and cosmogenic activation were investigated. Furthermore, the intrinsic background of the accompanied $2\nu\beta\beta$ decay cannot be neglected nor reduced. All calculated background rates for the detector material can be found in Table 5.8.

Radionuclei originating from the uranium and thorium decay series were generated in the detector material with a randomly chosen starting position. Contamination measurements were performed using gamma ray and mass spectroscopy and can be found in Table B.1. Furthermore, a comparison with the LNGS data, measured with the demonstrator setup, was done, see Section 5.4. The measured upper limits could be decreased by several orders of magnitude leading to equally low background rates in the order of $10^{-6} - 10^{-7}$ /kg/keV/yr. Thus, CdZnTe can be indeed produced radiopure.

The production of cosmogenic radionuclei due to activation depends on the particle flux, activation time and the cross sections of the activated material. At sea level, cosmogenic radionuclei are mainly generated by neutrons, whereas 15 % originate from protons. Muon activation can be neglected at sea level. As discussed in Section 2.4.4, materials exposed at the surface are often kept underground for several month or even years to eliminate short-living cosmogenic isotopes. Therefore, long-living isotopes are a crucial issue.

Altogether 13 isotopes, either long-living or short-living, but with a long-living mother nuclide, with Q-values near or above the ROI are regarded. A list can be found in Table 5.7. For the simulation three different neutron fluxes (CRY[6], Armstrong [103] and Gordon [104]) at sea level were considered and compared with each other. The production rate r [105] of each isotope is determined and in combination with the detection efficiency ϵ for each radionuclei the background rate can be calculated for different scenarios. In Table 5.7 the production rate and the efficiency are summarized. It is shown that four isotopes have either a high efficiency, production rate or both. Thus, the most important cosmogenic radionuclei are ^{88}Y, ^{106}Rh, ^{110m}Ag and ^{124}Sb. ^{88}Y and ^{110m}Ag have half-lives over 100 days, thus are long-living isotopes, whereas ^{106}Rh is short-living, but has a long-living mother nuclide. ^{124}Sb is a short-living isotope with a half-life of 60 days. In Table 5.8 the background rates for the four most important isotopes is shown. As the background rates depend on the time of activation of the material and further the time of decaying different scenarios are possible. Here, a scenario where one year activation and one year decaying is assumed. In addition, no extra shield to protect the source material during activation is used. The different neutron fluxes all lead to comparable results. The calculated background rates are

---

[6]CRY: Cosmic-Ray Yield, MC toolkit [101, 102]

in the order of $10^{-4} - 10^{-5}$ /kg/keV/yr, although one year of decaying was already expected. Therefore, they cannot be neglected and have to be kept in mind. For a better approximation on the contribution of cosmogenic radionuclides to the total background rate the exact exposure conditions, like altitude, latitude, time and a possible shield have to be known.

Table 5.7: Tabulated are the cosmogenic radionuclei for CdZnTe with their Q-value, half-life $T_{\frac{1}{2}}$, detection efficiency ϵ and production rate r. For some isotopes the mother nuclide and its half-life is also noted, because it is long-living, while the daughter nuclide is short-living. Four radionuclei are important due to either a high efficiency, production rate or both.

Isotope	Q-value [keV]	$T_{\frac{1}{2}}$	ϵ	r
^{22}Na	2842	2.6 yr	$5 \cdot 10^{-5}$	0.02
^{42}K/^{42}Ar	3525	12 h/33 yr	$1.9 \cdot 10^{-2}$	0.005
^{44}Sc/^{42}Ti	3654	3.9 h/63 yr	$4 \cdot 10^{-4}$	0.01
^{48}V	4012	16 d	$7 \cdot 10^{-5}$	0.06
^{56}Co	4566	77 d	$6 \cdot 10^{-4}$	0.1
^{68}Ga/^{68}Ge	2921	68 min/271 d	$1 \cdot 10^{-4}$	0.24
^{82}Rb/^{82}Sr	4400	1.3 min/26 d	$4 \cdot 10^{-3}$	1
^{84}Rb	2681	33 d	0	0.15
^{88}**Y**	2824	107 d	$\mathbf{2 \cdot 10^{-3}}$	**4.3**
^{106}**Rh**/^{106}**Ru**	3541	30 s/374 d	$\mathbf{1.4 \cdot 10^{-2}}$	**1.1**
^{110m}**Ag**	2892	250 d	$\mathbf{1 \cdot 10^{-4}}$	**19.5**
^{124}**Sb**	2905	60 d	$\mathbf{3 \cdot 10^{-4}}$	**18.2**
^{126}Sb/^{126}Sn	3670	12.5 d/100000 yr	$2 \cdot 10^{-4}$	1.3

In the simulation for the $2\nu\beta\beta$ and $0\nu\beta\beta$ decay ^{116}Cd was used as source isotope. The main code generates two β particles and when required the excited daughter isotope. For the $0\nu\beta\beta$ decay the 2n mechanism, see Section 2.2.1, was chosen for Majorana neutrinos. The detection efficiency is $73.08 \pm 0.01 \%$. As background levels are reduced, the energy resolution becomes important to diminish the contribution of $2\nu\beta\beta$ events in the peak and therefore to distinguish both decays. In Figure 5.11a the spectra of the $0\nu\beta\beta$ decay and the end-point of the $2\nu\beta\beta$ decay is depicted with an energy resolution of 5 % FWHM. It is shown that the $0\nu\beta\beta$ decay is overlaid with the $2\nu\beta\beta$ decay. For an energy resolution of 2 % FWHM, depicted in Figure 5.11b, both signals can be distinguished. Since the contribution of the $2\nu\beta\beta$ decay cannot be reduced nor shielded, the only way to get hold on it, is a sufficiently good energy resolution of at least 2 % at the Q-value of ^{116}Cd. With the chosen ROI, the contribution of the $2\nu\beta\beta$ decay to the total background rate is zero.

However, an upper limit of the background rate of

$$B_{CdZnTe}^{SDE,z} < 0.34 \cdot 10^{-3} \frac{\text{Entries}}{\text{kg} \cdot \text{keV} \cdot \text{yr}} \ (90\,\% \text{ C.L.}) \tag{5.21}$$

is determined.

Table 5.8: Tabulated are all background rates calculated for the **detector material CdZnTe**. In total an upper limit of the background rate of less than $0.34 \cdot 10^{-3}$ /kg/keV/yr (90 % C.L.) is determined.

Source	A_{ana} [mBq/kg]	B^{SDE}	$B^{SDE,z}$ [10^{-3}/kg/keV/yr]	$B_{MSE}^{SDE,z}$
^{238}U	$< 657 \cdot 10^{-6}$	$< 7.3 \cdot 10^{-3}$	$< 5.6 \cdot 10^{-3}$	$< 5.6 \cdot 10^{-3}$
^{234}U	$< 1332 \cdot 10^{-6}$	$< 1.1 \cdot 10^{-2}$	$< 7.4 \cdot 10^{-3}$	$< 7.4 \cdot 10^{-3}$
^{230}Th	$< 1188 \cdot 10^{-6}$	$< 1.8 \cdot 10^{-2}$	$< 1.3 \cdot 10^{-2}$	$< 1.3 \cdot 10^{-2}$
^{226}Ra	$< 151 \cdot 10^{-5}$	$< 1.8 \cdot 10^{-2}$	$< 1.2 \cdot 10^{-3}$	$< 1.2 \cdot 10^{-3}$
^{222}Rn	$< 265 \cdot 10^{-6}$	$(3.1 \pm 0.7) \cdot 10^{-3}$	$< 3.0 \cdot 10^{-3}$	$< 3.0 \cdot 10^{-3}$
^{218}Po	$< 266 \cdot 10^{-6}$	$< 3.5 \cdot 10^{-3}$	$< 1.6 \cdot 10^{-3}$	$< 1.6 \cdot 10^{-3}$
^{214}Bi	$< 141 \cdot 10^{-6}$	$(5.1 \pm 0.2) \cdot 10^{-2}$	$(4.7 \pm 0.6) \cdot 10^{-3}$	$(4.7 \pm 0.6) \cdot 10^{-3}$
^{214}Po	$< 141 \cdot 10^{-6}$	$< 2.0 \cdot 10^{-3}$	$< 1.4 \cdot 10^{-3}$	$< 1.4 \cdot 10^{-3}$
^{210}Po	$< 1 \cdot 10^{-3}$	$< 1.1 \cdot 10^{-2}$	$< 7.8 \cdot 10^{-3}$	$< 7.8 \cdot 10^{-3}$
^{232}Th	$< 86 \cdot 10^{-5}$	$< 6 \cdot 10^{-3}$	$< 4 \cdot 10^{-3}$	$< 4 \cdot 10^{-3}$
^{228}Th	$< 319 \cdot 10^{-6}$	$< 5 \cdot 10^{-3}$	$< 5 \cdot 10^{-3}$	$< 5 \cdot 10^{-3}$
^{224}Ra	$< 237 \cdot 10^{-6}$	$< 3 \cdot 10^{-3}$	$< 2 \cdot 10^{-3}$	$< 2 \cdot 10^{-3}$
^{220}Rn	$< 340 \cdot 10^{-6}$	$(4.2 \pm 0.9) \cdot 10^{-3}$	$< 4 \cdot 10^{-3}$	$< 4 \cdot 10^{-3}$
^{216}Po	$< 112 \cdot 10^{-6}$	$< 2 \cdot 10^{-3}$	$< 0.7 \cdot 10^{-3}$	$< 0.7 \cdot 10^{-3}$
^{212}Bi	$< 564 \cdot 10^{-7}$	$< 0.4 \cdot 10^{-3}$	$< 0.2 \cdot 10^{-3}$	$< 0.2 \cdot 10^{-3}$
^{212}Po	$< 564 \cdot 10^{-7}$	$< 1 \cdot 10^{-3}$	$< 0.8 \cdot 10^{-3}$	$< 0.8 \cdot 10^{-3}$
^{208}Tl	$< 564 \cdot 10^{-7}$	$(8.5 \pm 0.5) \cdot 10^{-3}$	$(1.4 \pm 0.2) \cdot 10^{-3}$	$(1.4 \pm 0.2) \cdot 10^{-3}$
^{88}Y	$-$	0.14 ± 0.02	< 0.03	< 0.03
^{106}Rh	$-$	0.99 ± 0.02	0.102 ± 0.006	0.102 ± 0.006
^{110m}Ag	$-$	< 0.58	< 0.13	< 0.13
^{124}Sb	$-$	0.15 ± 0.02	< 0.019	< 0.019
Σ	$-$	$-$		$\mathbf{< 0.34}$
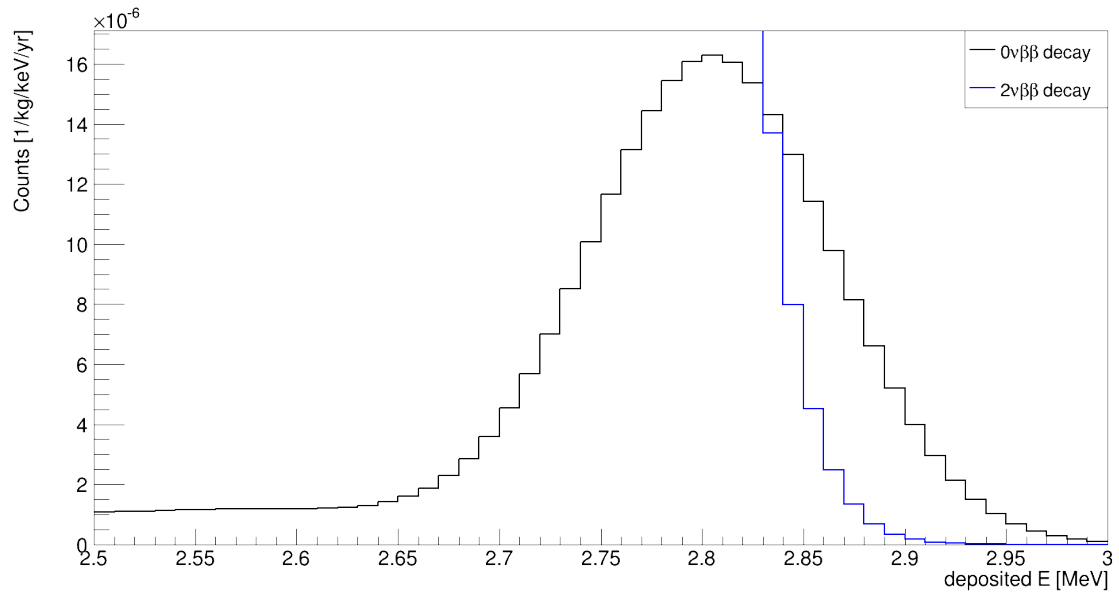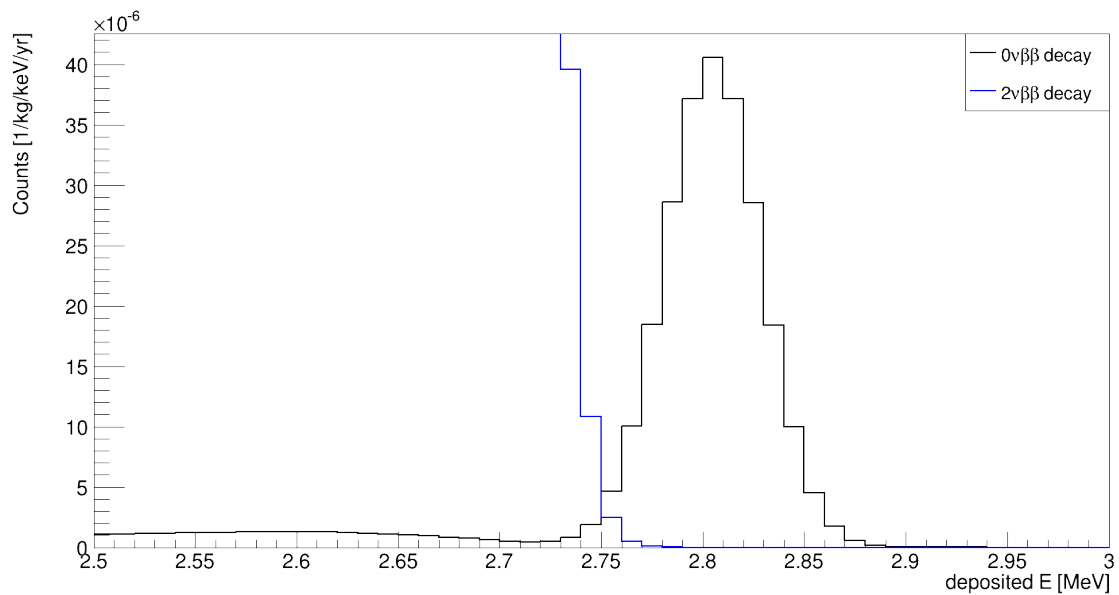
(a) 5 % FWHM

(b) 2 % FWHM

Figure 5.11: Schematically depicted are the spectra of the 0νββ decay and the end-point of the 2νββ decay of ^{116}Cd with an energy resolution of of 5 % FWHM in the upper figure and of 2 % FWHM in the bottom figure. The 0νββ decay is overlaid by the 2νββ decay in the 5 % FWHM case, whereas both signals can be distinguished for the 2 % FWHM energy resolution.

5.6   Results: Cathode

The background sources concerning the cathode can be sorted into intrinsic and surface sources. The cathode of the detectors contains platinum, which emits alpha particles. Additionally, airborne sources, like the progeny of ^{222}Rn can be attracted to the cathode. Therefore, both background categories are investigated in this section.

^{190}Pt is a COBRA-specific radionuclide. It is contained in the platinum layer building the cathode, see Section 5.1. Natural platinum contains 0.01 % of ^{190}Pt, which decays with a half-life of $6.5 \cdot 10^{11}$ years to ^{186}Os emitting an alpha ray with an energy of 3.249 MeV. The alpha peak can also be identified in the LNGS data taken from the demonstrator setup, see Section 3.4. Furthermore, the expected contamination c_{exp} of 0.01 % was compared to the LNGS data. It was shown, that c_{exp} is overestimated and thus, the contamination has to be decreased to $c_{ana} = 0.004$ %.

In the MC, platinum events were generated intrinsic in the cathode of all detectors. The starting position was randomly chosen. A background rate of $< 0.84 \cdot 10^{-3}$ /kg/keV/yr was calculated with a contamination of 0.004 % of ^{190}Pt.

As airborne sources on the surface of the cathode ^{222}Rn and ^{210}Po are considered. For both isotopes activities were derived from the comparison with the LNGS data. Therefore, ^{210}Po has an upper limit on the expected activity of less than 39 nBq/cm^2, while ^{222}Rn has 6 nBq/cm^2. For ^{210}Po a background rate of less than $0.01 \cdot 10^{-3}$ /kg/keV/yr was determined, whereas for ^{222}Rn a background rate of less than $0.0002 \cdot 10^{-3}$ /kg/keV/yr wa computed.

In Table 5.9 all results are summarized. The background rate can be further reduced by adding a fiducial volume cut, the z cut, and the LSE cut. Figure 5.12 shows the interaction depth z for events with deposited energies between 2.3–3.2 MeV originating from the ^{190}Pt simulation . The clustering at the first two bins $z \leq 0.2$ mm is clearly recognizable.

However, altogether the background rate for the cathode is

$$B_{cathode}^{SDE, z, LSE} < 0.85 \cdot 10^{-3} \frac{\text{Entries}}{\text{kg} \cdot \text{keV} \cdot \text{yr}} \ (90\,\% \text{ C.L.}) \qquad (5.22)$$

and dominated by ^{190}Pt events. To further reject events the z cut has to be modified, disregarding e.g. the first three bins resulting in a negligible background rate.
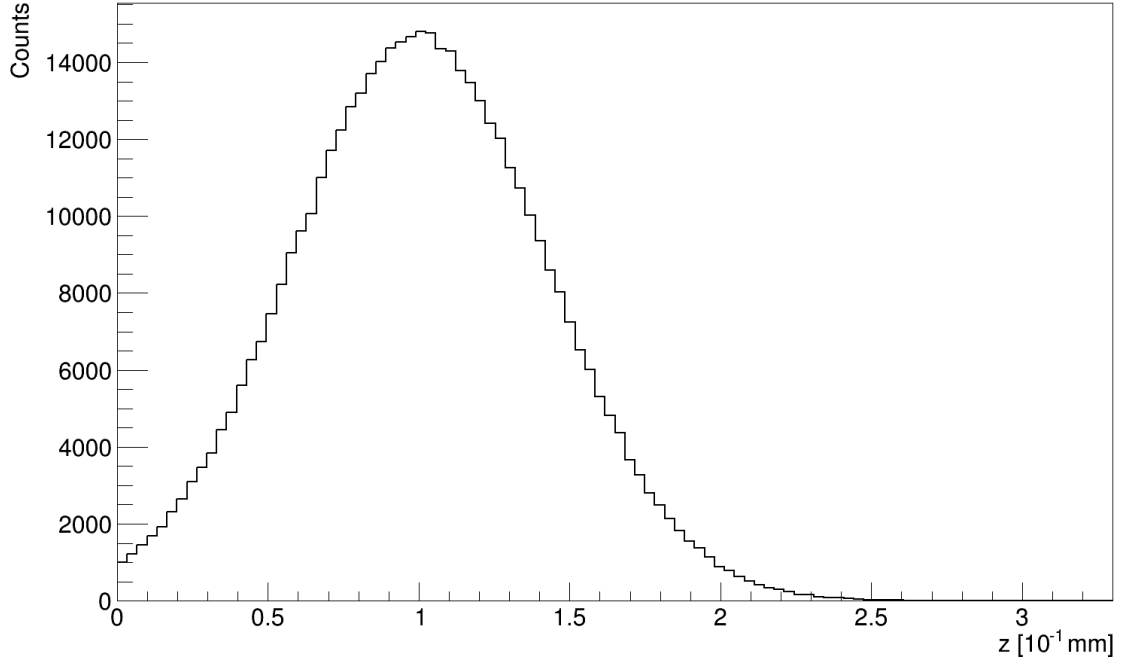
Figure 5.12: Depicted is the interaction depth z for ^{190}Pt events at the cathode with an energy resolution of 2% FWHM and a z resolution of $1\,\mathrm{mm}$. Only events with a deposited energy between 2.3–3.2 MeV are regarded. The events are clustered at $z \leq 2\,\mathrm{mm}$. By modifying the z cut, neglecting the first three bins, the background rate originating from ^{190}Pt can be further reduced.

Table 5.9: Tabulated are all background rates calculated for the **cathode**. Surface sources are noted with "sur". In total an upper limit of the background rate of less than $0.85 \cdot 10^{-3}\,/\mathrm{kg}/\mathrm{keV}/\mathrm{yr}$ (90 % C.L.) is determined.

Source	A_{ana}	c_{ana}	B^{SDE}	$B^{SDE,z}$	$B^{SDE,z}_{LSE}$	$B^{SDE,z}_{LSE,MSE}$
	$[\mathrm{mBq/cm^2}]$	$[\%]$	$[10^{-3}/\mathrm{kg}/\mathrm{keV}/\mathrm{yr}]$			
^{222}Rn sur	$< 6 \cdot 10^{-6}$	$-$	0.104 ± 0.009	< 0.003	< 0.002	< 0.002
^{210}Po sur	$< 3.9 \cdot 10^{-5}$	$-$	0.59 ± 0.05	< 0.02	< 0.01	< 0.01
^{190}Pt		0.004	275 ± 4	2.0 ± 0.3	< 0.84	< 0.84
Σ		$-$	$-$	$-$	$-$	$< \mathbf{0.85}$

5.7   Results: Glyptal Lacquer

The Glyptal lacquer covers all sides of the detector with a thickness of 10 μm in the MC. It can contain intrinsic sources of the environmental radioactivity. Besides, thermal neutrons are considered. For surface sources, the progeny of ^{222}Rn are treated. The contamination of the lacquer was measured with gamma [106] and mass spectroscopy [107] and results can be found in Table B.2. However, contaminations on the surface cannot be distinguished to intrinsic contaminations. Therefore, the same value is used in the analysis, but normalized to the surface of the painted detectors. Furthermore, a comparison with the measured LNGS data was performed resulting in reduced contamination values, see Section 5.4.

In Table 5.10 the calculated background rates obtained for the Glyptal lacquer are summarized. They are in the order of $10^{-3} - 10^{-6}$ /kg/keV/yr. The background is dominated by α emitters. Although their contribution can be decreased by the LSE cut, the cut efficiency of 75 % is too low. Furthermore, the expected activities are still conservatively approximated.

For the surface sources ^{222}Rn and ^{210}Po produce entries in the ROI. The results are in the same order compared to the corresponding intrinsic sources. There are two options to reduce the contribution of surface sources: cleansing and higher thickness of the lacquer. A cleansing would have been carried out before operation. It would reduce the contamination due to the handling of the painted detectors. A higher thickness of the lacquer would also reduce background, which is attracted to the surface during operation. Here, it is important to investigate an optimal thickness, because intrinsic sources produce more entries due to the higher mass.

In addition to the uranium and thorium decay chains, ^{60}Co, ^{235}U, and neutrons originating from spontaneous fission are investigated. They can be reduced effectively. Therefore, they can be neglected.

However, altogether a background rate of

$$B_{lacquer}^{SDE,\,z,\,LSE,\,MSE} < 61.11 \cdot 10^{-3} \, \frac{\text{Entries}}{\text{kg} \cdot \text{keV} \cdot \text{yr}} \; (90\,\% \text{ C.L.}) \qquad (5.23)$$

is determined for the Glyptal lacquer.

Table 5.10: Tabulated are all background rates calculated for the **Glyptal lacquer**. Surface sources are noted with "sur". In total an upper limit of the background rate of less than $61.11 \cdot 10^{-3}$ /kg/keV/yr (90 % C.L.) is determined.

Source	A_{ana} [mBq/kg]	A_{ana} [mBq/cm²]	B^{SDE}	$B^{SDE,z}$ [10^{-3}/kg/keV/yr]	$B^{SDE,z}_{LSE}$	$B^{SDE,z}_{LSE,MSE}$
^{238}U	< 30	–	75.4 ± 0.9	29.8 ± 0.6	8.2 ± 0.3	7.3 ± 0.3
^{234}U	< 17.4	–	35.1 ± 0.5	13.2 ± 0.3	3.8 ± 0.2	3.2 ± 0.2
^{230}Th	< 21.5	–	46.4 ± 0.7	17.9 ± 0.4	5.3 ± 0.2	4.3 ± 0.2
^{226}Ra	< 22.4	–	44.2 ± 0.7	16.8 ± 0.4	4.5 ± 0.2	4.1 ± 0.2
^{222}Rn	< 33.6	–	37.1 ± 0.7	23.9 ± 0.6	6.0 ± 0.3	6.0 ± 0.3
^{218}Po	< 7	–	6.0 ± 0.1	3.19 ± 0.09	0.80 ± 0.05	0.80 ± 0.05
^{214}Bi	< 1.4	–	0.111 ± 0.008	< 0.01	< 0.01	< 0.006
^{214}Po	< 1.4	–	0.48 ± 0.02	0.23 ± 0.01	0.056 ± 0.006	0.056 ± 0.006
^{210}Po	< 58.8	–	73 ± 1	32.9 ± 0.9	8.2 ± 0.5	8.2 ± 0.5
^{222}Rn sur	–	$< 2.5 \cdot 10^{-5}$	39.8 ± 0.6	28.5 ± 0.5	7.1 ± 0.2	7.1 ± 0.2
^{210}Po sur	–	$< 1.8 \cdot 10^{-5}$	36.2 ± 0.4	24.8 ± 0.4	6.2 ± 0.2	6.2 ± 0.2
^{232}Th	< 30.6	–	78 ± 1	30.5 ± 0.6	8.8 ± 0.3	7.4 ± 0.3
^{228}Th	< 13.3	–	14.7 ± 0.3	6.3 ± 0.2	2.0 ± 0.1	1.48 ± 0.09
^{224}Ra	< 11.4	–	10.8 ± 0.2	5.4 ± 0.1	1.41 ± 0.08	1.33 ± 0.08
^{220}Rn	< 7.6	–	6.1 ± 0.1	3.4 ± 0.1	0.85 ± 0.05	0.85 ± 0.05
^{216}Po	< 0.95	–	0.58 ± 0.01	0.27 ± 0.01	0.068 ± 0.005	0.068 ± 0.005
^{212}Bi	< 0.19	–	0.058 ± 0.002	0.029 ± 0.002	0.022 ± 0.001	$(9.1 \pm 0.9) \cdot 10^{-3}$
^{212}Po	< 0.19	–	0.036 ± 0.001	0.017 ± 0.001	$(4.2 \pm 0.6) \cdot 10^{-3}$	$(4.2 \pm 0.6) \cdot 10^{-3}$
^{208}Tl	< 0.19	–	$(8.2 \pm 0.8) \cdot 10^{-3}$	$< 7.1 \cdot 10^{-4}$	$< 7.1 \cdot 10^{-4}$	$< 3.6 \cdot 10^{-4}$
^{235}U	< 15	–	0.70 ± 0.07	< 0.06	< 0.03	< 0.02
SFN	< 0.00075	–	$(4.7 \pm 0.6) \cdot 10^{-5}$	$< 3.4 \cdot 10^{-6}$	$< 3.4 \cdot 10^{-6}$	$< 3.4 \cdot 10^{-6}$
Σ	–	–	–	–	–	$< \mathbf{61.11}$

5.8   Results: Delrin Support Structure

The support structure holds nine detectors in place. Altogether, 1536 holders are in the setup. They are made out of Delrin and in the simulations all background sources originating from environmental radioactivity are considered. Moreover, the progeny of ^{222}Rn can settle down on the surface of the holder and thus are also regarded. Contamination measurements were performed via gamma ray spectroscopy [106]. Furthermore, a comparison with the measured LNGS data was performed. Here, for ^{222}Rn and ^{210}Po intrinsic as well as on the surface the assumed activity could be reduced.

Table 5.11 summarizes the results calculated for the Delrin support structure. The background is dominated by α emitters with the main background source originating from the second group of the uranium series, ^{234}U. With already < 46 /kg/keV/yr, these radionuclide produces more than $70\,\%$ of the background of the Delrin structure. An activity $< 700\,\mathrm{mBq/kg}$ was assumed based on measurements with gamma ray spectroscopy. A recalculation via the comparison with the measured LNGS data was not possible, because with the method used, see Section 5.4, the individual spectra obtained from the simulation of the single nuclei of the decay chains do not overlay the spectrum of the LNGS data. However, Figure 5.13 shows the summed spectra of the ^{238}U decay chain in the Delrin holder compared to the LNGS data. An overestimation is visible, in particular below 2 MeV. Therefore, the real contamination has to be smaller as the expected ones in the analysis.
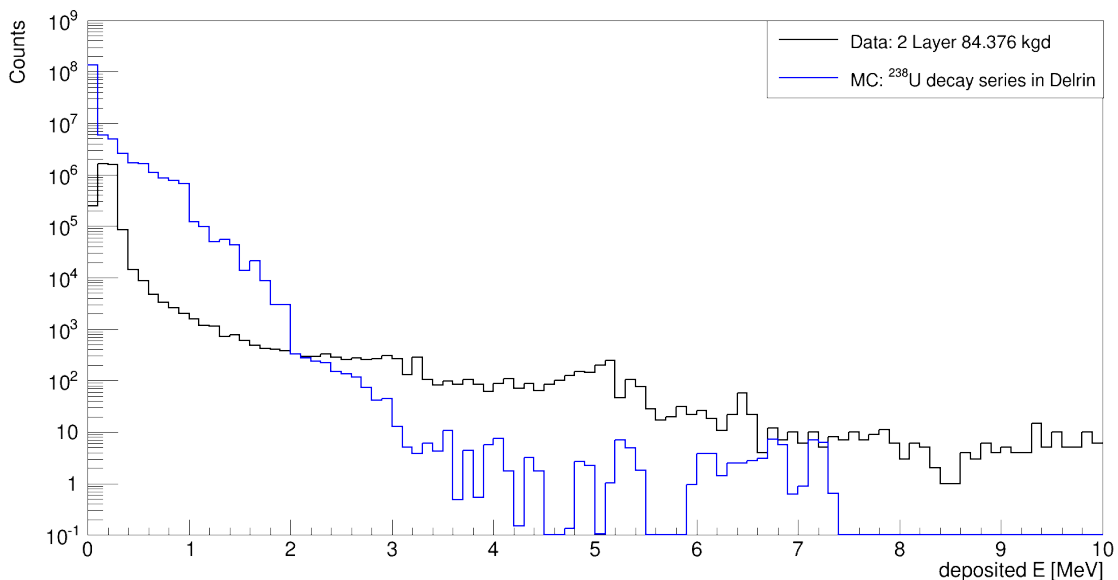
Figure 5.13: Plotted are the summed spectra of ^{238}U decay chain in the Delrin holder compared to the LNGS data. An overestimation is visible, especially below 2 MeV

The examined airborne sources on the surface of the support structure is dominated by ^{222}Rn. Here, an activity of less than $5.5 \cdot 10^{-6}$ mBq/cm^2 was determined. ^{210}Po can be neglected. To reduce the influence of the surface sources cleaning before operation and a possible higher thickness of the lacquer surrounding the detectors is possible and was mentioned in Section 5.7.

Furthermore ^{235}U and neutrons from spontaneous fission are investigated, but can also be neglected.

The thorium decay chain produces background rates in the order of $10^{-3} - 10^{-4}$ /kg/keV/yr, which is acceptable.

Altogether, a background rate of

$$B_{Delrin}^{SDE,\,z,\,LSE,\,MSE} < 63.89 \cdot 10^{-3} \, \frac{\text{Entries}}{\text{kg} \cdot \text{keV} \cdot \text{yr}} \ (90\,\% \ \text{C.L.}) \tag{5.24}$$

is determined for the Delrin support structure with the quoted activities.

Table 5.11: Tabulated are all background rates calculated for the **Delrin support structure**. Surface sources are noted with "sur". In total an upper limit of the background rate of less than $63.89 \cdot 10^{-3}$ /kg/keV/yr (90 % C.L.) is determined.

Source	A_{ana} [mBq/kg]	A_{ana} [mBq/cm^2]	B^{SDE}	$B^{SDE,z}$ [10^{-3}/kg/keV/yr]	$B^{SDE,z}_{LSE}$	$B^{SDE,z}_{LSE,MSE}$
^{234}U	< 700	—	< 111	< 111	< 46	< 46
^{226}Ra	< 0.1	—	0.03	< 0.02	< 0.007	< 0.007
^{222}Rn	< 0.1	—	0.067	< 0.04	< 0.01	< 0.01
^{218}Po	< 0.1	—	0.07 ± 0.01	0.036 ± 0.007	< 0.004	< 0.004
^{214}Bi	< 0.1	—	0.13 ± 0.02	0.03	0.03	< 0.02
^{214}Po	< 0.1	—	0.18 ± 0.03	0.012	< 0.04	< 0.04
^{210}Po	< 0.003	—	< 0.002	0.001	< 0.0005	< 0.0005
^{222}Rn sur	—	$< 5.5 \cdot 10^{-5}$	35.2 ± 0.7	28.1 ± 0.6	7.0 ± 0.3	7.0 ± 0.3
^{210}Po sur	—	$< 1.2 \cdot 10^{-7}$	0.086 ± 0.002	0.070 ± 0.001	0.0174 ± 0.0007	0.0174 ± 0.0007
^{228}Th	< 5	—	3.1 ± 0.6	< 3.5	< 1.2	< 1.2
^{224}Ra	< 5	—	< 3.4	< 2.7	< 0.9	< 0.9
^{220}Rn	< 5	—	5.1 ± 0.8	3.8 ± 0.7	< 1.7	< 1.7
^{216}Po	< 5	—	6.7 ± 0.9	3.8 ± 0.7	< 1.7	< 1.7
^{212}Bi	< 5	—	< 2.7	< 2.2	< 1.7	< 1.2
^{212}Po	< 5	—	7.8 ± 0.1	5.2 ± 0.8	< 2.1	< 2.1
^{208}Tl	< 5	—	10 ± 1	< 1.8	< 1.8	< 1.5
^{235}U	< 3	—	< 1.6	< 0.19	< 0.19	< 0.19
SFN	< 0.00035	—	$(4.3 \pm 0.3) \cdot 10^{-3}$	$< 1.67 \cdot 10^{-4}$	$< 1.67 \cdot 10^{-4}$	$< 1.67 \cdot 10^{-4}$
Σ	—	—	—	—	—	**< 63.89**

5.9 Results: Circuit Board of High Voltage Supply

The circuit board for the HV supply consists of two layers, which are mounted on the surface of the bottom plate of the holder. The first layer is out of Kapton covered with a second layer made out of copper. For more information see Section 5.1. All background sources originating from environmental radioactivity are regarded. Furthermore, the progeny of ^{222}Rn can be attracted to the surface of both layers of the High Voltage supply. Hence, they are also examined as a surface source.

In Table 5.12 the calculated background rates obtained for the circuit board for the HV supply are summarized. Measured activities can be found in Table B.4. Since another HV supply is used in the demonstrator setup currently, it is not possible to compare simulated data with the measured LNGS data. Furthermore, contamination measurements performed by the collaboration were not done yet. Therefore, values from the ILIAS database were used.

The background rates are in the order of 10^{-4} /kg/keV/yr and thus, acceptable. The most effective cuts in this case are the z and the LSE cut to create a fiducial volume. In addition, ^{235}U and neutrons from spontaneous fission were regarded. Here, SF neutrons can be neglected. The main background is created by ^{210}Po on the surface of the circuit board. The expected activity is $< 6.3 \cdot 10^{-3}$ mBq/cm^2 or < 500 mBq/kg, because surface and intrinsic sources cannot be distinguished by contamination measurements. However, for a surface source it is large. On the surface of the cathode, ^{210}Po has a contamination level of $< 3.9 \cdot 10^{-5}$ mBq/cm^2 or 361 mBq/kg, whereas for the Delrin support structure $< 1.2 \cdot 10^{-7}$ mBq/cm^2 or $< 9.74 \cdot 10^{-4}$ mBq/kg were determined, see Section 5.4. Therefore, a smaller contamination is likely.

In sum a background rate of

$$B_{CBHV}^{SDE,\,z,\,LSE,\,MSE} < 31.08 \cdot 10^{-3} \, \frac{\text{Entries}}{\text{kg} \cdot \text{keV} \cdot \text{yr}} \ (90\,\%\text{ C.L.}) \tag{5.25}$$

is determined for the circuit board for the HV supply with the quoted activities.

Table 5.12: Tabulated are all background rates calculated for the **circuit board of the HV supply**. Surface sources are noted with "sur". In total an upper limit of the background rate of less than $31.08 \cdot 10^{-3}$ /kg/keV/yr (90 % C.L.) is determined.

	A_{ana} [mBq/kg]	A_{ana} [mBq/cm²]	B^{SDE}	$B^{SDE,z}$ [10^{-3}/kg/keV/yr]	$B^{SDE,z}_{LSE}$	$B^{SDE,z}_{LSE,MSE}$
^{234}U	< 300	—	15 ± 2	< 1.0	< 0.6	< 0.6
^{230}Th	< 300	—	6 ± 1	< 1.0	< 0.6	< 0.6
^{226}Ra	< 90	—	5.0 ± 0.6	< 0.3	< 0.2	< 0.2
^{222}Rn	< 90	—	20 ± 1	< 1.2	< 0.42	< 0.42
^{218}Po	< 90	—	22 ± 1	< 0.99	< 0.42	< 0.42
^{214}Bi	< 90	—	12.8 ± 0.9	< 0.31	< 0.31	< 0.31
^{214}Po	< 90	—	27 ± 1	< 0.61	< 0.31	< 0.31
^{210}Po	< 500	—	934 ± 19	10 ± 2	< 5	< 5
^{222}Rn sur	—	$< 1.1 \cdot 10^{-3}$	351 ± 5	5.9 ± 0.6	1.5 ± 0.3	1.5 ± 0.3
^{210}Po sur	—	$< 6.2 \cdot 10^{-3}$	2881 ± 48	65 ± 7	16 ± 4	16 ± 4
^{228}Th	< 40	—	7.7 ± 0.5	< 0.27	< 0.14	< 0.14
^{224}Ra	< 40	—	8.2 ± 0.5	< 0.32	< 0.14	< 0.14
^{220}Rn	< 40	—	11.8 ± 0.6	< 0.40	< 0.14	< 0.14
^{216}Po	< 40	—	10.2 ± 0.6	< 0.36	< 0.14	< 0.14
^{212}Bi	< 80	—	7.6 ± 0.7	< 0.28	< 0.28	< 0.15
^{212}Po	< 80	—	25 ± 1	< 1.0	< 0.37	< 0.37
^{208}Tl	< 80	—	13 ± 1	< 0.15	< 0.15	< 0.15
^{235}U	< 100	—	14 ± 1	< 0.19	< 0.19	< 0.19
SFN	< 0.00015	—	$(4.7 \pm 0.4) \cdot 10^{-5}$	$< 1.2 \cdot 10^{-6}$	$< 1.2 \cdot 10^{-6}$	$< 1.2 \cdot 10^{-6}$
Σ	—	—	—	—	—	**< 31.08**

5.10 Results: Circuit Board of Anode Read-Out

The circuit board for the anode read-out consists of Kapton in the MC, like the first layer of the High Voltage supply and is mounted on the surface of the top plate of the holder. Therefore, all background sources generated from environmental radioactivity are investigated.

Table 5.13 shows the determined background rates for the read-out Kapton cable. Contamination were not measured so far. Therefore, values were taken from the ILIAS database and can be found in Table B.5. The rates are in general low in the order of $10^{-4} - 10^{-7}$/kg/keV/yr. Due to the top plate of the Delrin holder, most events are shielded. With an additional z cut and LSE cut events on the surface can be removed. Furthermore, γ rays from ^{214}Bi can be eliminated by the MSE cut.

Altogether, a background rate of

$$B^{SDE,z,LSE,MSE}_{CBAnode} < 0.95 \cdot 10^{-3} \frac{\text{Entries}}{\text{kg} \cdot \text{keV} \cdot \text{yr}} \ (90\,\% \text{ C.L.}) \qquad (5.26)$$

is calculated for the circuit board of the anode read-out with the measured activities, which is acceptable low.

Table 5.13: Tabulated are all background rates calculated for the **circuit board for the anode read-out**. In total an upper limit of the background rate of less than $0.95 \cdot 10^{-3}$ /kg/keV/yr (90 % C.L.) is determined.

	A_{ana} [mBq/kg]	B^{SDE}	$B^{SDE,z}$	$B^{SDE,z}_{LSE}$	$B^{SDE,z}_{LSE,MSE}$
			$[10^{-3}$/kg/keV/yr$]$		
^{214}Bi	< 70	2.0 ± 0.4	< 0.41	< 0.41	< 0.23
^{214}Po	< 70	< 1.8	< 0.41	< 0.23	< 0.23
^{216}Po	< 40	< 0.46	< 0.13	< 0.13	< 0.13
^{212}Po	< 40	< 1.1	< 0.23	< 0.13	< 0.13
^{208}Tl	< 40	1.2 ± 0.3	< 0.23	< 0.23	< 0.23
^{235}U	< 0.001	$< 7.9 \cdot 10^{-6}$	$< 3.3 \cdot 10^{-6}$	$< 3.3 \cdot 10^{-6}$	$< 3.3 \cdot 10^{-6}$
SFN	$< 35 \cdot 10^{-6}$	$(9 \pm 1) \cdot 10^{-6}$	$< 4.9 \cdot 10^{-7}$	$< 4.9 \cdot 10^{-7}$	$< 4.9 \cdot 10^{-7}$
Σ	$-$	$-$	$-$	$-$	$\mathbf{< 0.95}$

5.11   Results: ASICs

The ASICs are made out of silicon and are in the MC mounted on the Delrin support structure of a row, which also holds eight holders in place, in front of the first holder. Here, background sources from environmental radioactivity and the progeny of ^{222}Rn are investigated.

Measured activities were determined via gamma ray spectroscopy [106] and can be found in Table B.6. As the ASICs are approximately in $10\,\mathrm{cm}$ distance to the detectors, α and also β particles do not reach the detectors. Only radionuclei emitting γ rays can produce counts in the ROI, which is also shown in Table 5.14. In this case, events from ^{208}Tl are already removed to a minimum the fiducial volume cut in z, whereas entries from ^{214}Bi are reduced by the z and MSE cut. Neutrons from spontaneous fission can be neglected completely due to a rate in order of 10^{-4}/kg/keV/yr. In sum, a background rate of

$$B_{ASICs}^{SDE,z,LSE,MSE} < 1.25 \cdot 10^{-3} \frac{\text{Entries}}{\text{kg} \cdot \text{keV} \cdot \text{yr}} \; (90\,\% \text{ C.L.}) \qquad (5.27)$$

is determined for the circuit board for the anode read-out with the quoted activities.

Table 5.14: Tabulated are all background rates calculated for the **ASICs**. In total an upper limit of the background rate of less than $1.25 \cdot 10^{-3}$ /kg/keV/yr (90 % C.L.) is determined.

	A_{ana} [mBq/kg]	B^{SDE}	$B^{SDE,z}$	$B_{LSE}^{SDE,z}$	$B_{LSE,MSE}^{SDE,z}$
		$[10^{-3}$/kg/keV/yr]			
^{214}Bi	< 1.6	< 2.5	< 1.7	< 1.5	< 0.86
^{208}Tl	< 1.3	< 0.70	< 0.39	< 0.39	< 0.39
SFN	$< 125 \cdot 10^{-7}$	$(3.5 \pm 0.4) \cdot 10^{-4}$	$< 3.2 \cdot 10^{-5}$	$< 2.7 \cdot 10^{-5}$	$< 2.7 \cdot 10^{-5}$
Σ	$-$	$-$	$-$	$-$	$< \mathbf{1.25}$

5.12 Results: Gas

The inner part of the setup, the detectors and the support structures, is in reality constantly flushed with nitrogen. But even though, airborne sources can also be present in the gas. In the MC, the gas is also set to nitrogen. As airborne sources radon and its progeny are examined.

It is complicated to measure the activity in gases, because it depends on the construction materials of the laboratory and the quality of the nitrogen flushing. Therefore, a default activity of $1\,\mathrm{mBq/kg}$ was assumed corresponding to standard activity levels for low counting experiments. Table 5.15 shows the obtained background rates. First, only α emitters generate events in the ROI. Furthermore, they can be effectively eliminated to a minimum by the LSE cut.

In sum, a background rate of

$$B_{\mathrm{gas}}^{SDE,z,LSE,MSE} < 0.17 \cdot 10^{-3} \frac{\mathrm{Entries}}{\mathrm{kg} \cdot \mathrm{keV} \cdot \mathrm{yr}} \ (90\,\% \ \mathrm{C.L.}) \tag{5.28}$$

is calculated for the gas, which is acceptable low. Yet, a reliable contamination level has to be determined.

Table 5.15: Tabulated are all background rates calculated for the **gas**. In total an upper limit of the background rate of less than $0.17 \cdot 10^{-3}$ /kg/keV/yr (90 % C.L.) is determined.

Source	A_{ana} [mBq/kg]	B^{SDE}	$B^{SDE,z}$	$B_{LSE}^{SDE,z}$	$B_{LSE,MSE}^{SDE,z}$
		[10^{-3}/kg/keV/yr]			
^{222}Rn	< 1	0.290 ± 0.005	0.285 ± 0.005	0.071 ± 0.003	0.071 ± 0.003
^{210}Po	< 1	0.358 ± 0.006	0.354 ± 0.006	0.088 ± 0.003	0.088 ± 0.003
Σ	−	< 1.64	< 1.626	< 0.0002	**< 0.17**

5.13   Results: Shielding Materials

The shield consists of three layers – copper, lead and boron loaded polyethylene. All layers are regarded concerning environmental radioactivity. Contamination measurements were performed via gamma ray spectroscopy [106] for the copper. The results can be found in Table B.7. For the lead and PE, no measurements were done by the collaboration so far. Therefore, values from the ILIAS database were taken and are summarized in Table B.8 and B.9.

The calculated background rates for the shield layers can be found in Table 5.16. Only neutrons from spontaneous fission generate events in the ROI. However, they can be removed by the cuts. Furthermore, α, β and γ rays from outer layers, like the lead and PE, are effectively shielded by the inner layer copper. Nevertheless, it has to be kept in mind, that no holes are implemented in the shield in the MC. In reality, the shield is build out of bricks leading to gaps between them. Furthermore, cable feedthroughs are neither implemented in the simulation, but necessary for the operation of the experiment.

Table 5.16: Tabulated are all background rates calculated for the **shield layers**.

Material	Source	A_{ana} [mBq/kg]	B^{SDE}	$B^{SDE,z}$	$B^{SDE,z}_{LSE}$	$B^{SDE,z}_{LSE,MSE}$
			$[10^{-3}/\text{kg/keV/yr}]$			
Copper	SFN	< 0.00005	0.046 ± 0.006	< 0.004	< 0.003	< 0.002
Lead	SFN	< 0.0000675	0.09 ± 0.02	< 0.01	< 0.01	< 0.01

5.14 Results: External Radiation Sources

As external background sources only cosmogenic muons and muon-induced neutrons are important. Radiation originating from radionuclei is not regarded, because the emitted particles are not able to penetrate the shield, which was already shown with the simulation of the different layers of the shield. Since the development of the shield was optimized for fast neutrons, the individual background rate is now calculated. Furthermore, the background generated from muons is regarded.

5.14.1 Muons

So far, the large scale COBRA experiment setup gets by without an active veto. As discussed in Section 4.5, different veto systems are possible, including plastic or liquid scintillator. However, there is no active component implemented in the GDML geometry. Thus, the background rate of muons is determined without using any veto, just by employing the analysis cuts.

Overall $1 \cdot 10^6$ events were produced on the outer surface of the B5PE layer of the shield, corresponding to a measuring time of 5.853 ± 0.006 years, which is calculated using

$$t = \frac{N_{sim}}{a} \cdot \phi_m \tag{5.29}$$

with the muon flux ϕ_m and the area $a = 16351.5 \, \text{cm}^3$, on which the muons were simulated. The muon flux is given by [95]

$$\phi_m = (2.58 \pm 0.3) \cdot 10^{-8} \, \text{cm}^{-2} \, \text{s}^{-1}. \tag{5.30}$$

In the ROI 6489 ± 81 entries were detected without applying any further cut, besides the energy cut. Considering only single detector events and neglecting lateral surface and multi side events, only 0.5 entries remain. Combining Equation 5.13 and 5.29 produces an upper limit for the background rate, which is summarized in Table 5.17. In total an upper limit of the background rate of less than $0.02 \cdot 10^{-3}$ /kg/keV/yr is determined.

Table 5.17: Tabulated are all background rates calculated for **muons**.

Source	B^{SDE}	$B^{\text{SDE, z}}$	$B_{\text{LSE}}^{\text{SDE, z}}$	$B_{\text{LSE, MSE}}^{\text{SDE, z}}$
	$[10^{-3}/\text{kg/keV/yr}]$			
Muons	< 0.06	< 0.04	< 0.02	$\mathbf{< 0.02}$

5.14.2 Fast Neutrons

The background rate for fast neutrons is calculated also using Equation 5.13. The measuring time t is determined by Equation 5.31 and depends on the neutron flux ϕ_n,

see Equation 5.7, and the area $a = 16351.5\,\mathrm{cm}^3$, on which the neutrons were simulated.

$$t = \frac{N_{sim}}{a} \cdot \phi_n \qquad (5.31)$$

Altogether, $1 \cdot 10^6$ neutrons were generated and 774 ± 28 entries were registered in the ROI without any additional cut. Combining Equation 5.13 and 5.31 and employing the SDE cut as well as the z cut, all entries are removed to a minimum in the ROI. In Table 5.18 the calculated background rates combining Equation 5.13 and 5.31 are shown.

Table 5.18: Tabulated are all background rates calculated for **fast neutrons**.

Source	B^{SDE}	$B^{SDE,z}$	$B^{SDE,z}_{LSE}$	$B^{SDE,z}_{LSE,MSE}$
		$[10^{-3}/\mathrm{kg}/\mathrm{keV}/\mathrm{yr}]$		
Neutrons	0.008	< 0.002	< 0.002	**< 0.002**
Neutrons (Warwick)	< 0.005	< 0.003	< 0.002	< 0.002

Furthermore, the MC was repeated for the shield design created by the University of Warwick, introduced in Section 4.1.1. The obtained background rate can also be found in Table 5.18. The performance is comparable. The background rates have the same order of magnitude. However, the new shield design consisting of only three instead of eleven layers offers an easier handling and mounting.

5.15   Summary

In Section 5.5 – 5.14, the calculated background rates in different setup parts were presented and discussed. In Table 5.19, they are summarized. Altogether, a background rate of

$$B_{total}^{SDE,z,LSE,MSE} < 160 \cdot 10^{-3} \frac{\text{Entries}}{\text{kg} \cdot \text{keV} \cdot \text{yr}} \ (90\,\% \text{ C.L.}) \qquad (5.32)$$

is computed.

Table 5.19: Tabulated are all background rates calculated for the different setup parts. In total an upper limit of the background rate of less than $160 \cdot 10^{-3}$ /kg/keV/yr is determined. In addition, the scaled background rates are summarized.

	$B_{LSE,MSE}^{SDE,z}$ $[10^{-3}$/kg/keV/yr]	$B_{LSE,MSE,scaled}^{SDE,z}$ $[10^{-3}$/kg/keV/yr]
CdZnTe	< 0.34	< 0.054
Cathode	< 0.85	< 0.136
Lacquer	< 61.11	< 9.78
Delrin	< 63.89	< 10.22
CB HV	< 31.08	< 31.08
CB Anode	< 0.95	< 0.95
ASICs	< 1.25	< 1.25
Gas	< 0.17	< 0.17
Shield	< 0.01	< 0.01
External	< 0.01	< 0.01
Σ_{total}	< 160	< 54

Figure 5.14 illustrates the contribution to the total background rate of the different parts. The main contribution originates from the Delrin support structure (holder) in quick succession of the Glyptal lacquer. In the third place follows the circuit board of the HV supply. These three setup parts are all located nearby the detectors and additionally reliable contamination measurements are not available. Although upper limits of the contamination of the lacquer and the Delrin were measured, see Table B.2 and B.3, by the collaboration and the simulations also compared to the LNGS data, see Section 5.4, many activities are still in the range of 10–1000 mBq/kg. Such values are high regarding low counting experiments like COBRA and it seems reasonable to assume that the activities have been overestimated, because precise measurements are often not possible due to the limited sensitivity of the instrumentation used.

This assumption is confirmed by Figure 5.15. Here, the LNGS data spectrum is plotted in comparison with the MC from the detector material CdZnTe, the lacquer, the Delrin and the cathode. The SDE, z, LSE and MSE cut were neither applied to the LNGS nor the MC data. It is shown, that the MC spectrum lies above the LNGS data spectrum.
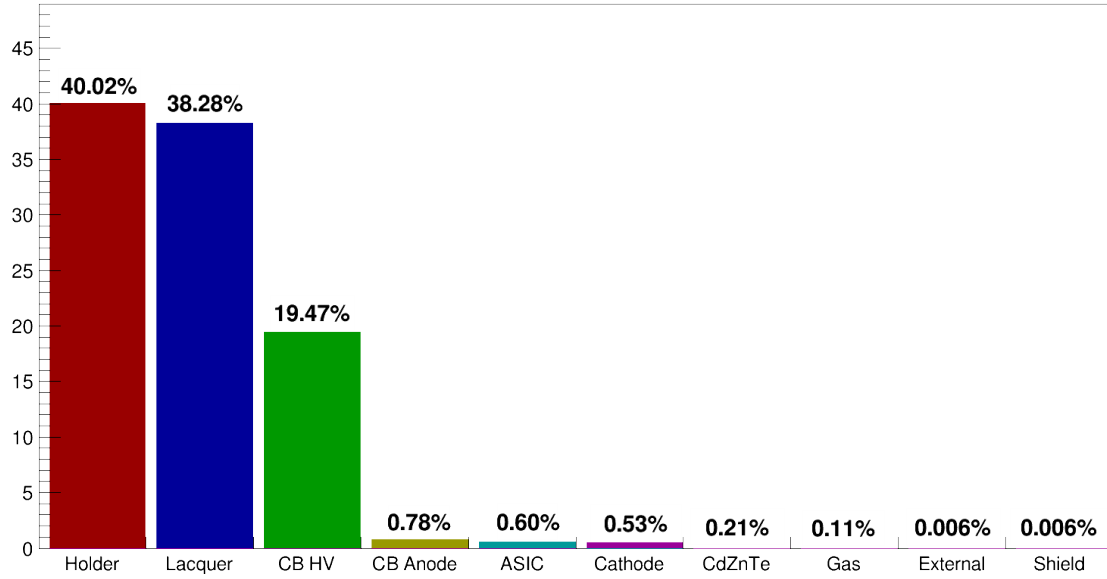
Figure 5.14: Illustrated is the contribution of the different setup parts to the total background rate. The main portion arise from the Delrin support structure, followed by the lacquer and the CB of the HV supply.
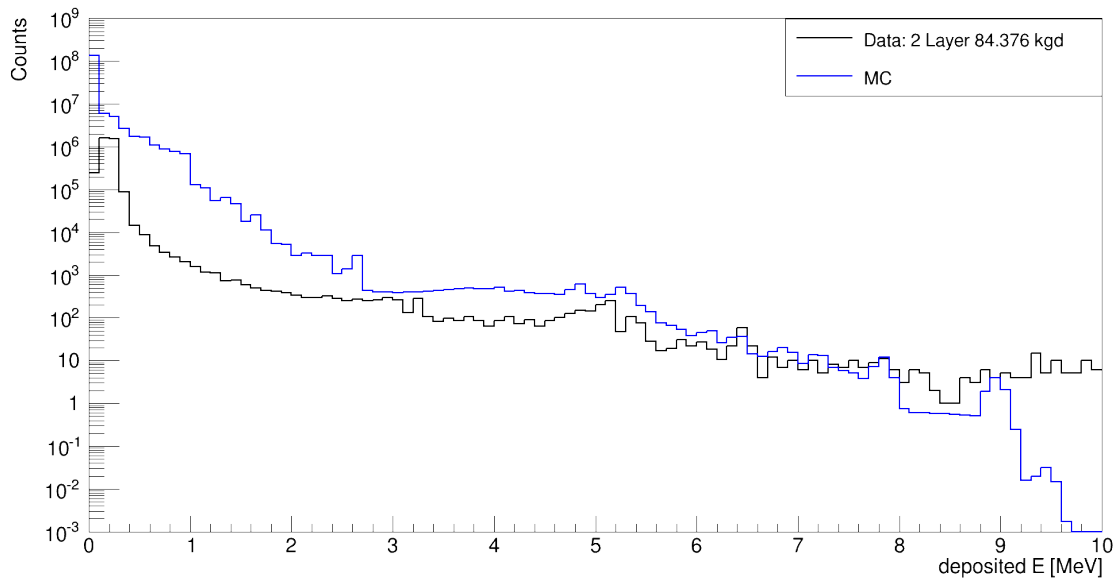
Figure 5.15: Plotted are the spectra of LNGS data compared to the MC spectrum of CdZnTe, the lacquer, the Delrin and the cathode. An overestimation of the employed activities in the analysis can be recognized due to the higher MC spectrum, especially below 2.5 MeV.

In particular, below 2.5 MeV the difference is approximately in the order of three magnitudes. Working out another scaling factor k following the example set by Section 5.4

in the ROI, the total background rate can be reduced to

$$B_{total,scaled}^{SDE,z,LSE,MSE} < 54 \cdot 10^{-3} \frac{\text{Entries}}{\text{kg} \cdot \text{keV} \cdot \text{yr}} \; (90\% \text{ C.L.}) \qquad (5.33)$$

under the presumption that the background in the ROI at the demonstrator setup originates from the four mentioned setup parts. k equals 0.16 in this case. In Table 5.19 the scaled background rates are summarized.

Figure 5.16 shows the influence of the different cuts on the MC data. With the SDE cut, the counting rate is reduced to one half. Events on the cathode and anode side of the detectors are removed by the z cut, whereas the LSE cut eliminates also events on the other lateral surfaces. Thus, many α events from the ^{238}U and ^{232}Th decay series are removed. The MSE cut is again not considered, for the reasons explained in 5.3, resulting in a peak nearby the ROI corresponding to ^{208}Tl. However, by applying the MSE cut in the analysis these events are removed.
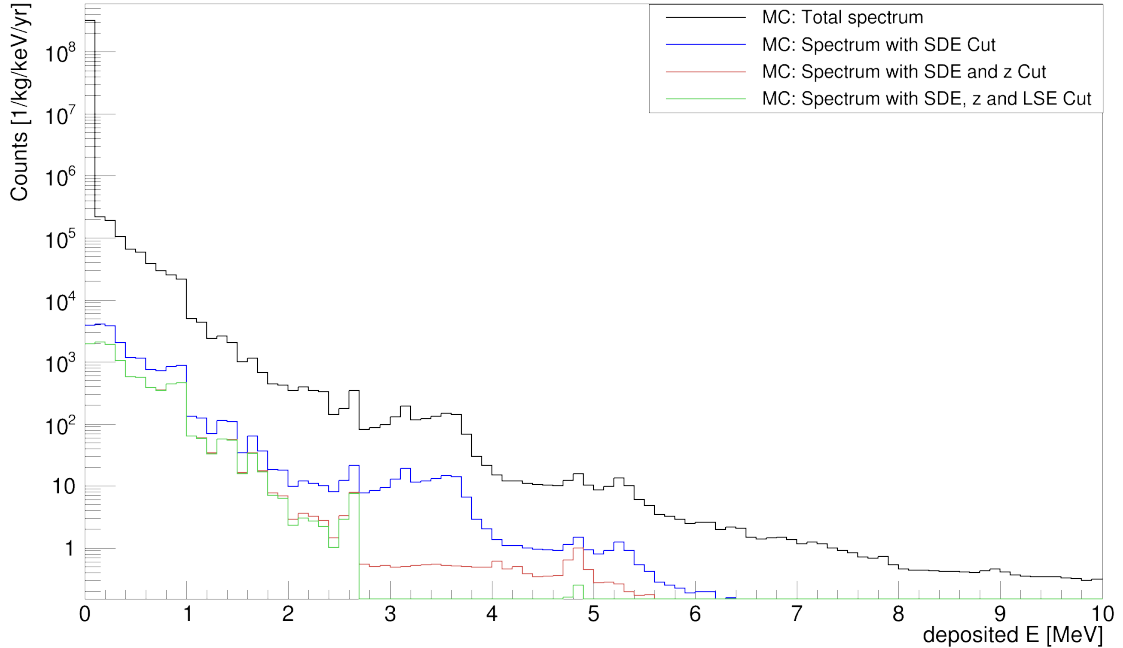
Figure 5.16: Plotted are the total MC spectra with different cuts. The counting rate is reduced by a factor of 2 by the SDE cut. The z cut removes events on the cathode and anode side of the detectors. Furthermore, the LSE cut eliminates α events on the lateral surfaces. The MSE cut is not considered due to the energy dependence of the cut.

The contribution by different particle types to the total background rate is shown in Figure 5.17. The dark colored bars correspond to the portion before applied cuts, while the lighter colored bars show the contribution after employed cuts. It is shown, that the implemented cuts eliminate successfully gammas, neutrons, electrons and muons. Alpha particles dominate in both cases. After the cuts their contribution is 99%.
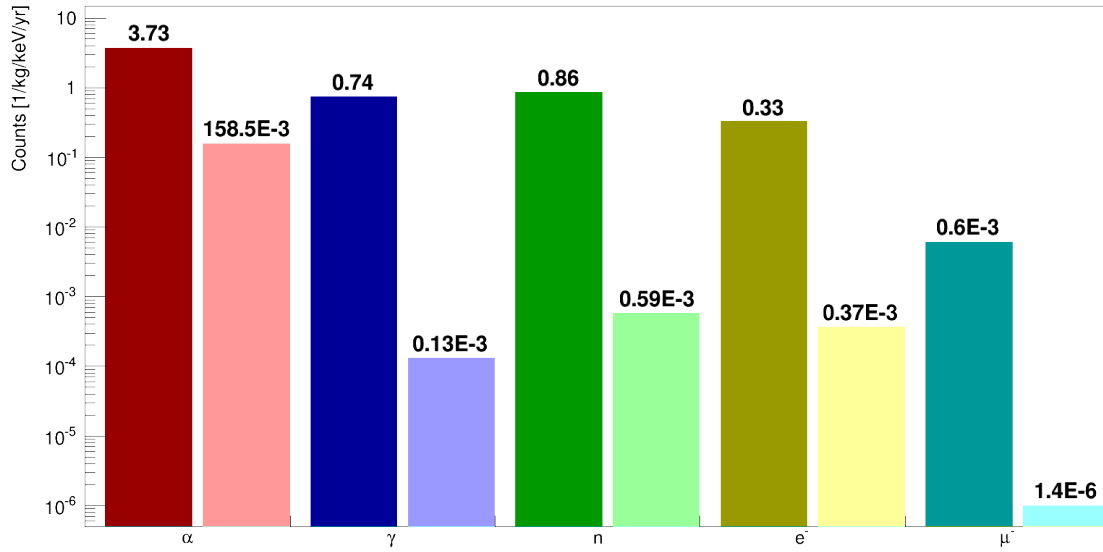
Figure 5.17: Illustrated is the contribution of different particle types to the total background
rate. The darker bars refer to the share before, the lighter colored ones after
applied cuts. The main portion arise from α particles.

In addition, the portion of the surface sources can be determined. Airborne sources,
in particular ^{222}Rn and ^{210}Po, can settle down on surfaces. Regarded surfaces are the
cathode, the lacquer, the Delrin, the CB of the HV and anode read-out. A contribution
on the total background rate of 26.8 % of airborne sources on surfaces was determined.

Chapter 6

Conclusion

Within this thesis, a multi-layer shield concerning the attenuation of the neutron and gamma activities was developed and the expected total background rate for the large scale COBRA experiment was determined based on Monte Carlo simulations. Geant4 was used as simulation toolkit with the COBRA specific software VENOM. Furthermore, two different physics lists were discussed.

A previous shield design was already created by the University of Warwick consisting of eleven narrow layers making it complex and difficult to handle and mount. The total thickness was 52 cm. The goal was to develop a shield less complex without the loss of effectiveness. For this, at first single-layer shields were investigated determining material properties concerning neutron attenuation and (n,γ) self-absorbing effects. Next, material layers were combined considering also other material properties, like radiopureness for the innermost layer. The new improved shield design consists of three layers: 10 cm 5 % boron doped polyethylene as outermost layer, 20 cm of lead and 10 cm of copper as innermost layer. Comparing both shields showed background rates in the same order of 10^{-6}/kg/keV/yr. Thus, they are equally good concerning external radiation suppression. Hence, the goal is achieved and additionally the size of the shield is reduced, because 12 cm were saved in the thickness.

For the calculation of the total background rate, the present large scale COBRA setup design was implemented in the simulation. Different background sources, covering natural radioactivity in the environment, detector material and near detector area, as well as cosmogenic radioactivity, thermal neutron and high-energetic radiation sources were simulated within various setup parts as intrinsic and surface sources. As surface sources radon progeny were considered. Activities and contamination measured via gamma ray or mass spectroscopy by the collaboration were employed in the analysis. Furthermore, cuts similar to the analysis of the LNGS data were also developed for the Monte Carlo simulations and implemented in the analysis software. For setup parts, which are already used in the COBRA demonstrator setup at the LNGS, simulations were compared to the measured LNGS data showing an overestimation of the measured contamination,

because the instrumentation used is often not sensitive enough to detect low counting rates. Therefore, a scaling factor was determined for the individual background channels to obtain a more realistic activity value. With this, each obtained Monte Carlo spectrum was compared individually to the LNGS data spectrum neglecting summed up background resulting in a very conservative calculation preventing an underestimation. Detector parts, which are already worked with at the LNGS and thus possible for this analysis, were the detector material, the cathode, the Delrin support structure and the lacquer surrounding the detectors. Here, also intrinsic and surface sources were distinguished. All measured contaminations could be decreased by several orders of magnitude.

With the newly determined contamination a total background rate of less than $160 \cdot 10^{-3}$/kg/keV/yr was calculated regarding also external radiation sources, the circuit boards of high voltage supply and anode read-out, the ASICs, the nitrogen gas surrounding the detectors and the shielding materials next to the already mentioned parts. The main contribution to the total background rate arise from the lacquer (44.6 %) and the Delrin support structure (42.3. %). Both setup parts are close to the detectors and reliable contamination measurements are not available. An overestimation of the individual contaminations was determined by combining all simulation from setup part, already operated in the demonstrator setup. By calculating a further scaling factor to reduce the influence of summed background sources, the total background rate could be decreased to less than $54 \cdot 10^{-3}$/kg/keV/yr. Concerning particle types contribution, it was shown that α particles dominate with a portion of 99 %. Furthermore, the share of surface sources is 26.8 %.

To be competitive with other next-generation neutrinoless double beta experiments COBRA must achieve a background level in the order of 10^{-3}/kg/keV/yr. Hence, the determined background is still too high. However, other options are still possible to reduce the background further. First, the quantity of simulated events can be increased to reduce the influence of the statistic error. With time-coincidence analysis, the decay sequence ^{214}Bi$\rightarrow^{214}$Po$\rightarrow^{210}$Pb could be identified with a efficiency of 41.42 % [108]. The efficiency was restricted by the time resolution of the ADCs operated at the LNGS. A new evaluation of the time-coincidence analysis is under investigation [109]. In addition, developing methods concerning surface cleaning of e.g. the Delrin support structure and the lacquer on the detectors, before operation to reduce their influence are planned. Also, the thickness of the applied lacquer is a crucial factor. With a thicker layer, surface contaminations could be reduced. Another powerful option is the discrimination of α and β particles in the detector. Here, first attempts were already made [110]. However, the most promising option is the development of a background model of the LNGS data and further contamination measurements to get reliable activity values. Here, an optimization of the ROI regarding the "signal to noise" ratio would also be an opportunity to reject events.

Nevertheless, the first attempt to determine the total background rate was done resulting in a promising background level of $54 \cdot 10^{-3}$/kg/keV/yr. The estimation was

done very conservatively to reduce the chance of an underestimation. Yet, plenty of options involving the analysis of the LNGS data as well as the investigation of additional experimental issues, like cleansing, are planned or already worked on to decrease the background rate further.

Appendix A

Cross Sections
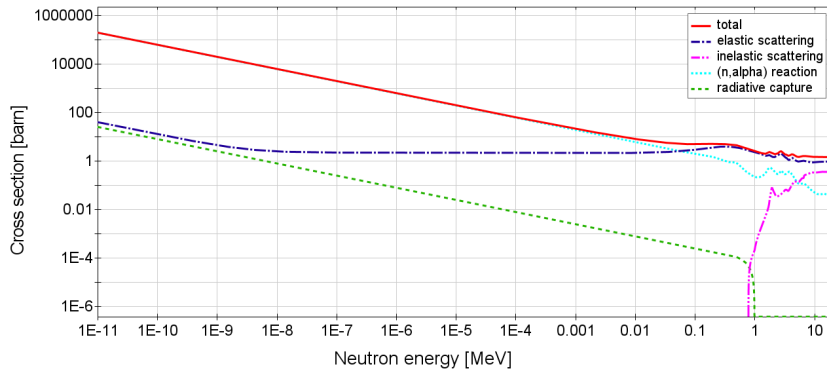
(a) Neutron cross section for ^{10}B
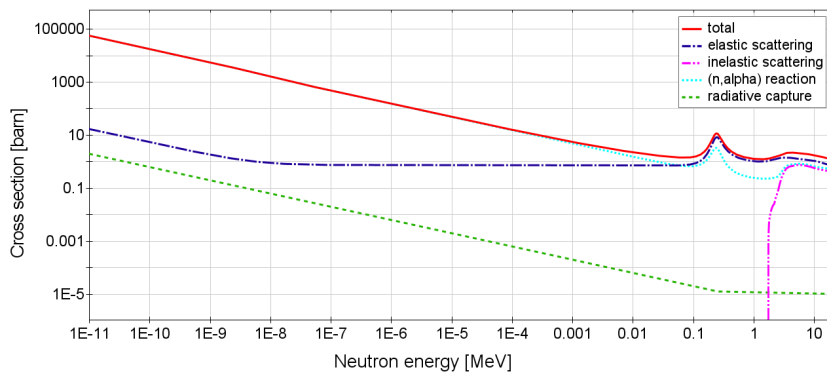
(b) Neutron cross section for ^{6}Li

Figure A.1: Incident neutron cross section for ^{10}B and ^{6}Li. The data is based on the ENDF/B-VII library. It is shown that for a wide energy range the total cross section is above 1 barn. For thermal neutrons ($\sim 10^{-9}$ MeV) the total cross section increases rapidly. For neutron energies above 1 MeV inelastic scattering becomes important.
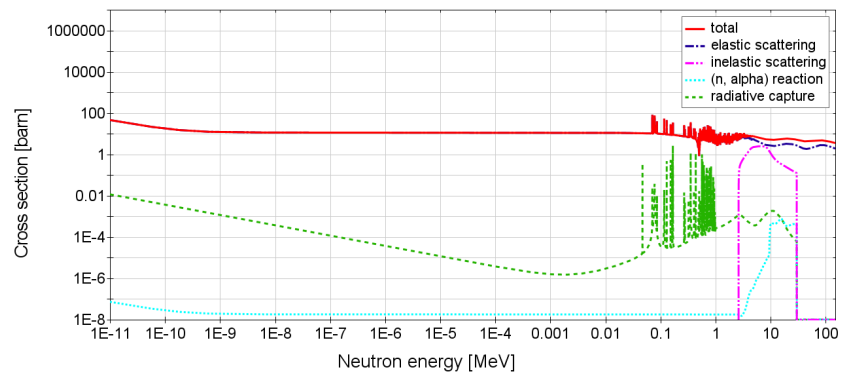
(a) Neutron cross section for ^{208}Pb
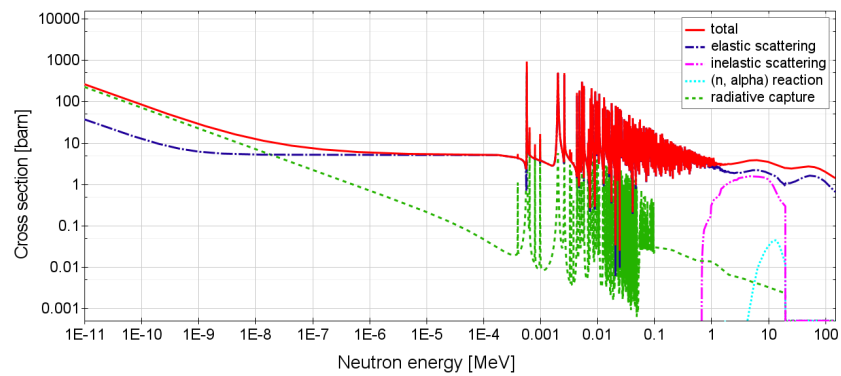
(b) Neutron cross section for ^{63}Cu

Figure A.2: Incident neutron cross section for ^{208}Pb and ^{63}Cu. The data is based on the ENDF/B-VII library. For neutron energies less than 1 MeV inelastic scattering becomes important in metals. Furthermore the cross section of radiative capture is one order of magnitude smaller compared to ^{10}B and ^{6}Li.

Appendix B

Contamination Measurements

Table B.1: Tabulated are the results of contamination measurements for CdZnTe. The upper limits of the activity A were determined via gamma ray spectroscopy [106], while the upper limits of the contamination c were measured via mass spectroscopy [107, 111].

Isotope	A [106] [mBq/kg]	c [107] [ppb]	c [111] [ppb]	c [111] [ppb]
^{228}Ra	< 47	$-$	$-$	$-$
^{228}Th	< 60	$-$	$-$	$-$
^{226}Ra	< 51	$-$	$-$	$-$
^{234}Th	< 210	$-$	$-$	$-$
^{234m}Pa	< 1200	$-$	$-$	$-$
^{235}U	< 5	$-$	$-$	$-$
^{40}K	< 260	$-$	$-$	$-$
^{137}Cs	40 ± 8	$-$	$-$	$-$
^{60}Co	< 19	$-$	$-$	$-$
^{9}Be (^{9}Li)	$-$	< 5.3	$-$	$-$
^{23}Na (^{23}Mg, ^{23}Na)	$-$	97	$-$	$-$
^{60}Ni (^{60}Cu)	$-$	28	$-$	$-$
^{66}Zn (^{66}Ga)	$-$	$1.1 \cdot 10^7$	$-$	$-$
^{82}Se (^{82}As)	$-$	440	$-$	$-$
^{140}Ce (^{140}La)	$-$	97	$-$	$-$
^{166}Er (^{166}Tm)	$-$	46	$-$	$-$
^{202}Hg (^{202}Au)	$-$	< 5	$-$	$-$
^{238}U	$-$	< 1.8	< 0.45	< 0.55
^{232}Th	$-$	< 1.7	< 0.45	< 1

Table B.2: Tabulated are the results of contamination measurements for Glyptal Lacquer. The upper limits of the activity A were determined via gamma ray spectroscopy [106], while the upper limits of the contamination c were measured via mass spectroscopy [107].

Isotope	A [106] [mBq/kg]		c [107] [ppb]
^{228}Ra	< 180	^{232}Th	146 ± 15
^{228}Th	< 190		
^{226}Ra	< 140	^{238}U	115 ± 10
^{234}Th	< 1500		
^{234m}Pa	< 4300		
^{235}U	< 15		
^{40}K	< 1000	^{40}K	1640 ± 400
^{137}Cs	< 56		
^{60}Co	< 72		

Table B.3: Tabulated are the results of contamination measurements for Delrin. The upper limits of the activity A were determined via gamma ray spectroscopy [106].

Isotope	A [mBq/kg]
^{228}Ra	< 5
^{228}Th	< 5
^{226}Ra	< 5
^{234m}Pa	< 700
^{235}U	< 3
^{40}K	< 31
^{137}Cs	3 ± 1
^{60}Co	< 2
^{210}Pb	< 200

Table B.4: Tabulated are the results of contamination measurements for the activity A for Kapton covered with copper [112].

Isotope	A [mBq/kg]	A [mBq/kg]	A [mBq/kg]	A [mBq/kg]	A [mBq/kg]
^{228}Ac	$-$	< 90	< 40	< 300	$-$
^{212}Pb	< 6	< 25	< 30	150	< 25
^{208}Tl	13	50	< 80	300	< 20
^{234}Th	$-$	< 240	< 300	< 950	$-$
^{214}Pb	14	< 40	< 70	< 240	< 15
^{214}Bi	14	< 80	90	280	< 60
^{235}U	$-$	< 90	< 100	< 400	$-$
^{40}K	< 90	< 900	700	< 2100	400
^{137}Cs	< 5	$-$	20	$-$	< 9
^{60}Co	10	150	< 40	700	< 15
^{210}Pb	300	< 250	< 500	< 2200	300

Table B.5: Tabulated are the results of contamination measurements for the activity A for Kapton [112].

Isotope	A [mBq/kg]
^{228}Ac	$-$
^{212}Pb	40
^{208}Tl	$-$
^{234}Th	$-$
^{214}Pb	30
^{214}Bi	70
^{235}U	$-$
^{40}K	< 90
^{137}Cs	< 5
^{60}Co	10
^{210}Pb	500

Table B.6: Tabulated are the results of contamination measurements for ASICs. The upper limits of the activity A were determined via gamma ray spectroscopy [106].

Isotope	A [mBq/kg]
^{228}Ra	< 1.9
^{228}Th	< 1.3
^{226}Ra	< 1.6
^{234}Th	< 25
^{234m}Pa	< 29
^{235}U	$< (1.5 \pm 0.6)$
^{40}K	$< (16 \pm 5)$
^{137}Cs	< 0.55
^{60}Co	< 0.13

Table B.7: Tabulated are the results of contamination measurements for copper. The upper limits of the activity A were determined via gamma ray spectroscopy [106].

Isotope	A [mBq/kg]
^{228}Ra	< 2.1
^{228}Th	< 2.3
^{226}Ra	< 2.5
^{234}Th	< 100
^{234m}Pa	< 47
^{235}U	< 1.4
^{40}K	< 11
^{137}Cs	< 0.9
^{60}Co	< 0.6

Table B.8: Tabulated are the results of contamination measurements for the activity A for lead [112].

Isotope	A [mBq/kg]
^{228}Ac	–
^{212}Pb	< 5
^{208}Tl	< 0.8
^{234}Th	< 135
^{214}Pb	< 3
^{214}Bi	< 2
^{235}U	< 6
^{137}Cs	< 0.6
^{210}Pb	24000

Table B.9: Tabulated are the results of contamination measurements for the activity A for PE [112].

Isotope	A [mBq/kg]
^{228}Ac	–
^{212}Pb	–
^{208}Tl	< 6
^{234}Th	–
^{214}Pb	–
^{214}Bi	< 16
^{235}U	–
^{137}Cs	< 20
^{40}K	< 70
^{60}Co	< 5
^{210}Pb	70

Appendix C

Additional plots for Chapter 4
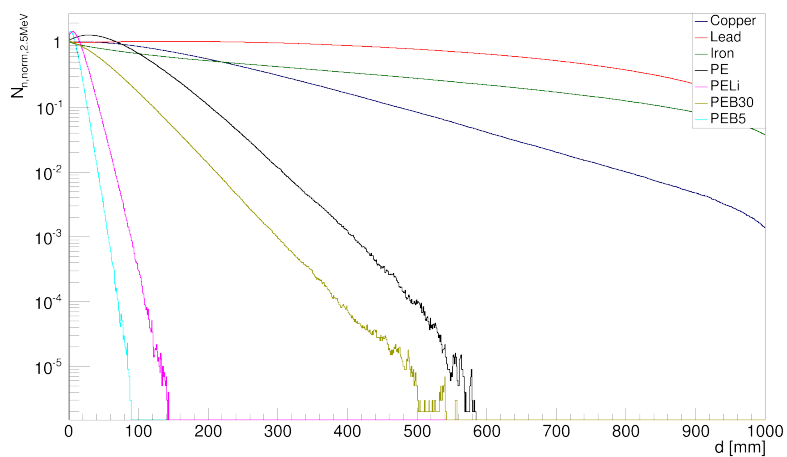
(a) Neutron population $N_{\mathrm{n,norm,2.5\,MeV}}$ for one layer shields
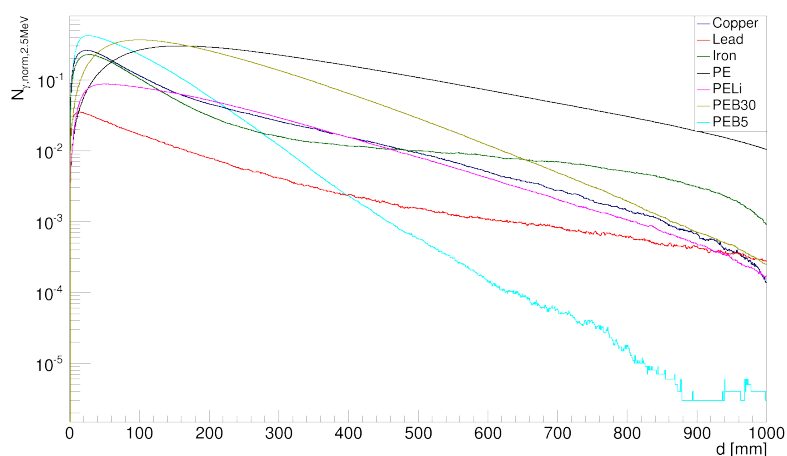
(b) Gamma population $N_{\gamma,\mathrm{norm,2.5\,MeV}}$ for one layer shields

Figure C.1: Plotted is the population for neutrons and gammas for an incident neutron energy of $E = 2.5\,\mathrm{MeV}$ in one layer shields.
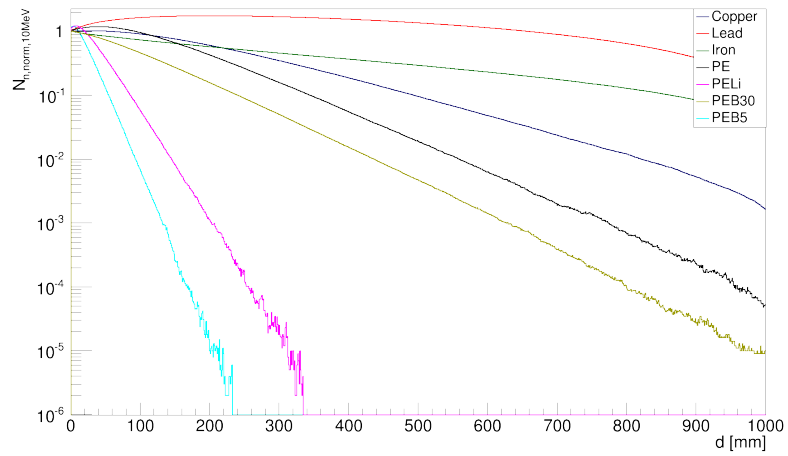
(a) Neutron population $N_{\mathrm{n,norm,10\,MeV}}$ for one layer shields
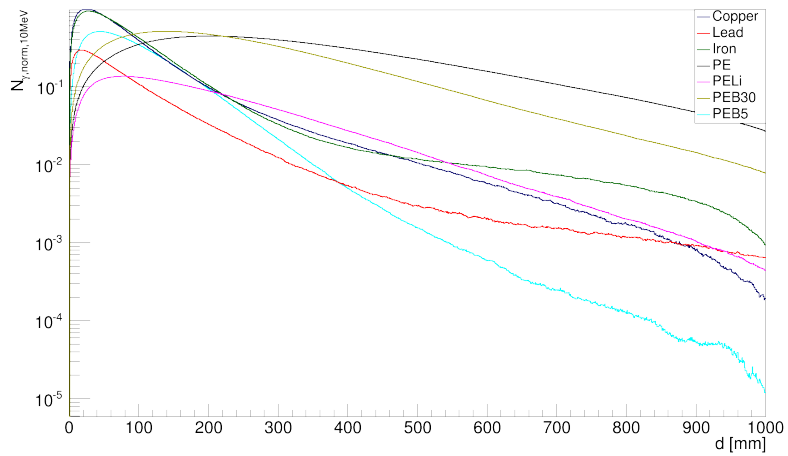
(b) Gamma population $N_{\gamma,\mathrm{norm,10\,MeV}}$ for one layer shields

Figure C.2: Plotted is the population for neutrons and gammas for an incident neutron energy of $E = 10\,\mathrm{MeV}$ in one layer shields.
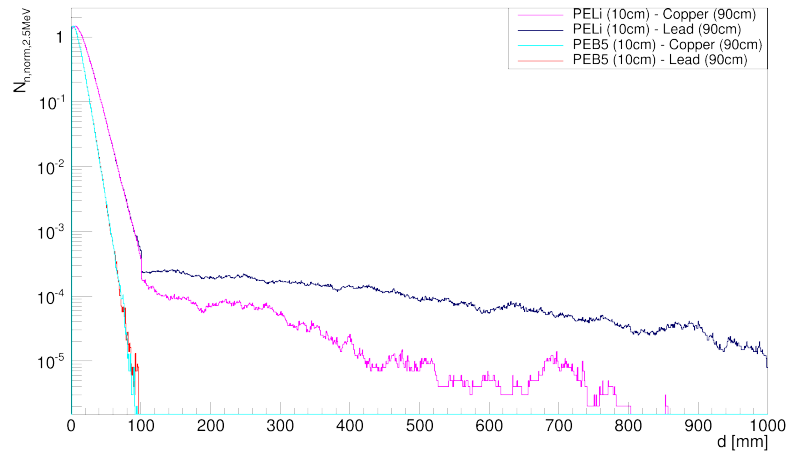
(a) Neutron population $N_{\mathrm{n,norm,2.5\,MeV}}$ for two layer shields
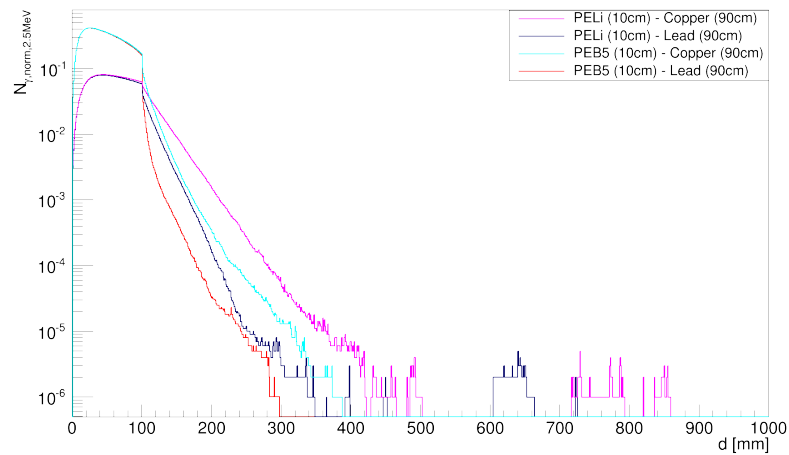
(b) Gamma population $N_{\gamma,\mathrm{norm,2.5\,MeV}}$ for two layer shields

Figure C.3: Plotted is the population for neutrons and gammas for an incident neutron energy of $E = 2.5\,\mathrm{MeV}$ in two layer shields.
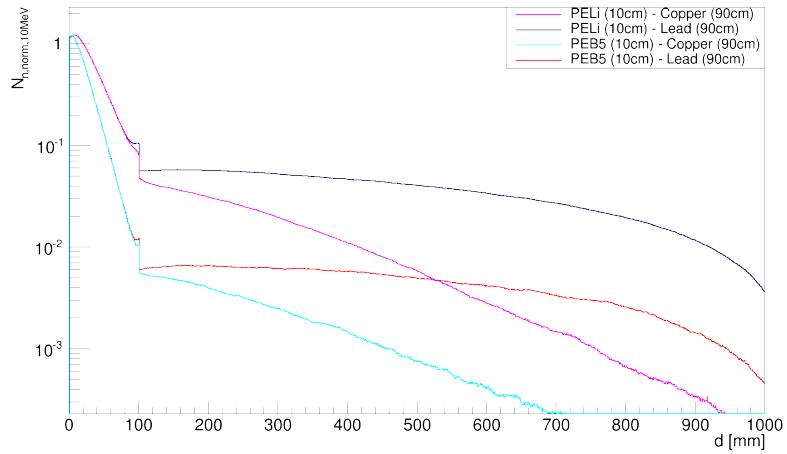
(a) Neutron population $N_{\mathrm{n,norm,10\,MeV}}$ for two layer shields
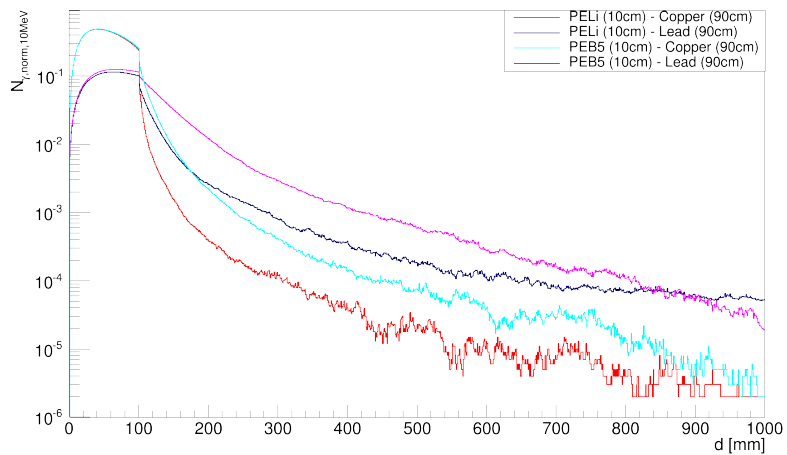
(b) Gamma population $N_{\gamma,\mathrm{norm,10\,MeV}}$ for two layer shields

Figure C.4: Plotted is the population for neutrons and gammas for an incident neutron energy of $E = 10\,\mathrm{MeV}$ in two layer shields.
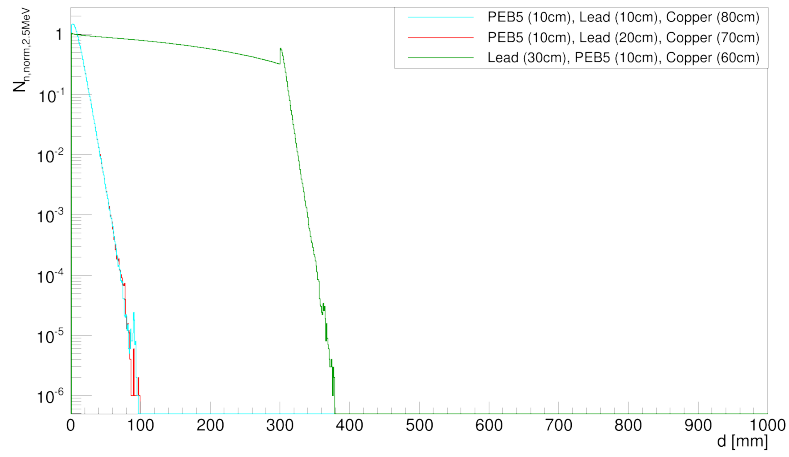
(a) Neutron population $N_{\mathrm{n,norm,2.5\,MeV}}$ for three layer shields
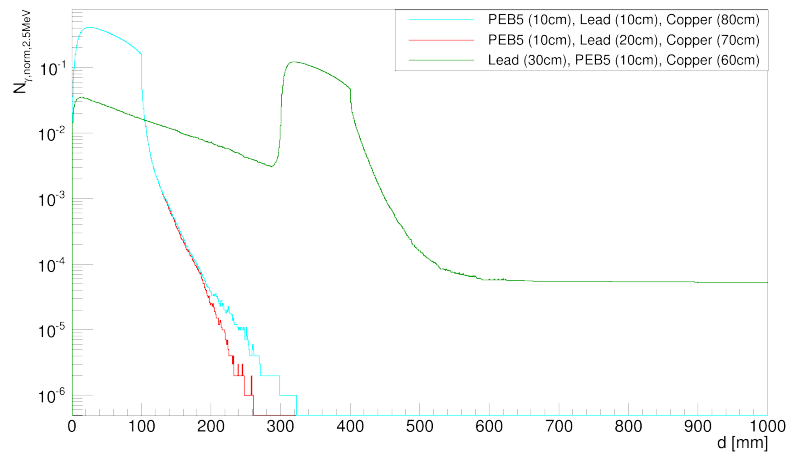
(b) Gamma population $N_{\gamma,\mathrm{norm,2.5\,MeV}}$ for three layer shields

Figure C.5: Plotted is the population for neutrons and gammas for an incident neutron energy of $E = 2.5\,\mathrm{MeV}$ in three layer shields.
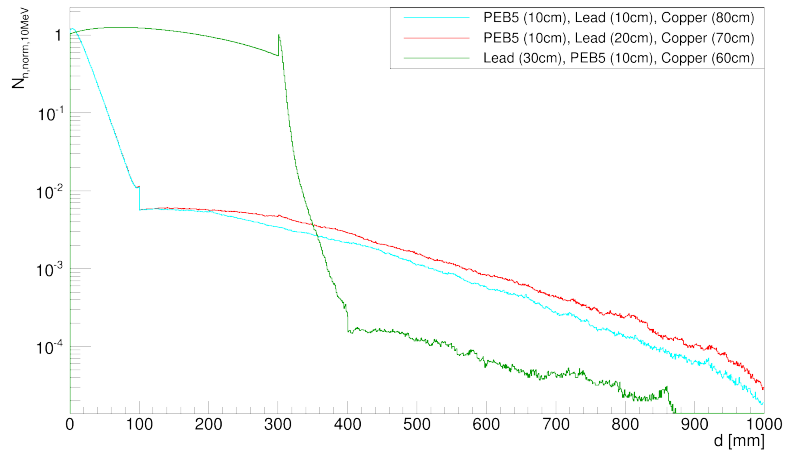
(a) Neutron population $N_{\mathrm{n,norm,10\,MeV}}$ for three layer shields
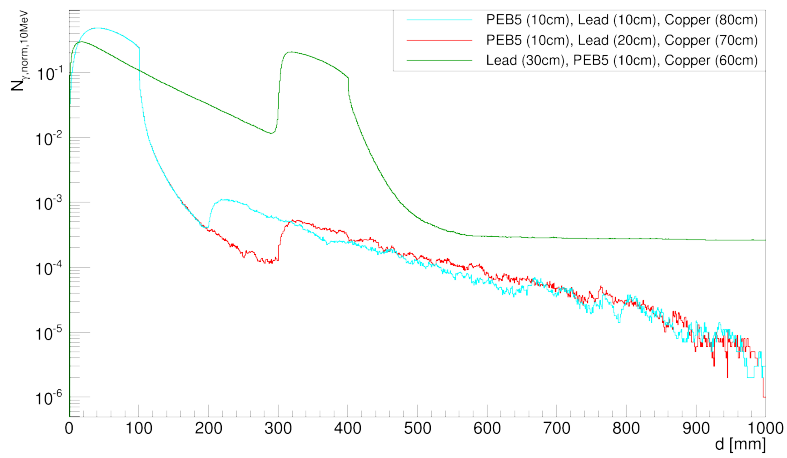
(b) Gamma population $N_{\gamma,\mathrm{norm,10\,MeV}}$ for three layer shields

Figure C.6: Plotted is the population for neutrons and gammas for an incident neutron energy of $E = 10\,\mathrm{MeV}$ in three layer shields.

List of Figures

List of Tables

Bibliography

[1] J. Schneps. *Proceedings of the International Conference on Neutrino Physics and Astrophysics. 13. Boston (Medford) : June 5 - 11, 1988.* World Scientific, 1989.

[2] M. Flanz et al. Baryogenesis through mixing of heavy majorana neutrinos. *Physics Letters B*, 389(4):693 – 699, 1996. DOI: 10.1016/S0370-2693(96)80011-6.

[3] E. Majorana. Teoria simmetrica dell'elettrone e del positrone. *Il Nuovo Cimento*, 14(4):171–184, 1937. DOI: 10.1007/BF02961314.

[4] G. Gelmini and E. Roulet. Neutrino masses. *Reports on Progress in Physics*, 58(10), 1995. DOI: 10.1088/0034-4885/58/10/002.

[5] H. V. Klapdor-Kleingrothaus and A. Staudt. *Teilchenphysik ohne Beschleuniger.* Teubner Verlag, 1995. ISBN: 9783519030881.

[6] R. Wendell et al. Atmospheric neutrino oscillation analysis with sub-leading effects in Super-Kamiokande I, II, and III. *Phys. Rev. D*, 81:092004, 2010. DOI: 10.1103/PhysRevD.81.092004.

[7] M. Kobayashi and T. Maskawa. CP-Violation in the Renormalizable Theory of Weak Interaction. *Progress of Theoretical Physics*, 49(2):652–657, 1973. DOI: 10.1143/PTP.49.652.

[8] K. Nakamura and Particle Data Group. Review of Particle Physics. *Journal of Physics G: Nuclear and Particle Physics*, 37(7A):075021, 2010. DOI: 10.1088/0954-3899/37/7A/075021.

[9] Z. Maki, M. Nakagawa, and S. Sakata. Remarks on the Unified Model of Elementary Particles. *Progress of Theoretical Physics*, 28(5):870–880, 1962. DOI: 10.1143/PTP.28.870.

[10] R. N. Cahn et al. White Paper: Measuring the Neutrino Mass Hierarchy. *ArXiv e-prints*, 2013. ArXiv: 1307.5487.

[11] J. Bian. The NOvA Experiment: Overview and Status. *ArXiv e-prints*, 2013. ArXiv: 1309.7898.

[12] Y.-F. Li. Overview of the Jiangmen Underground Neutrino Observatory (JUNO). *Int.J.Mod.Phys.Conf.Ser.*, 31:1460300, 2014. DOI: 10.1142/S2010194514603007.

[13] D. J. Koskinen. ICECUBE-DEEPCORE-PINGU: Fundamental Neutrino and Dark Matter Physics at the South Pole. *Modern Physics Letters A*, 26(39):2899–2915, 2011. DOI: 10.1142/S021773231103725X.

[14] K. Clark and D. F. Cowen. IceCube/DeepCore and IceCube/PINGU: Prospects for Few-GeV Scale ν Physics in the Ice. *Nuclear Physics B - Proceedings Supplements*, 233(0):223 – 228, 2012. Proceedings of the 10th International Conference on Beauty, Charm and Hyperons in Hadronic Interactions. DOI: 10.1016/j.nuclphysbps.2012.12.081.

[15] J. Tauber et al. The Scientific programme of Planck. *ArXiv e-prints*, 2006. ArXiv: astro-ph/0604069.

[16] P. A. R. Ade et al. Planck 2013 results. XVI. Cosmological parameters. *ArXiv e-prints*, 2013. ArXiv: 1303.5076.

[17] E. W. Otten and C. Weinheimer. Neutrino mass limit from tritium β decay. *Reports on Progress in Physics*, 71(8):086201, 2008. DOI: 10.1088/0034-4885/71/8/086201.

[18] C. Kraus et al. Final results from phase II of the Mainz neutrino mass search in tritium beta decay. *Eur.Phys.J.*, C40:447–468, 2005. DOI: 10.1140/epjc/s2005-02139-7.

[19] D. S. Parno. The KATRIN Experiment: Status and Outlook. *ArXiv e-prints*, 2013. ArXiv: 1307.5289.

[20] H. V. Klapdor-Kleingrothaus et al. Evidence for neutrinoless double beta decay. *Modern Physics Letters A*, 16:2409–2420, 2001. DOI: 10.1142/S0217732301005825.

[21] H. V. Klapdor-Kleingrothaus et al. The Evidence for the Observation of $0\nu\beta\beta$ Events from the full Spectra. *Modern Physics Letters A*, 21(20):1547 – 1566, 2006. DOI: 10.1142/S0217732306020937.

[22] C. E. Aalseth et al. Comment on 'Evidence for neutrinoless double beta decay'. *Mod.Phys.Lett.*, A17:1475–1478, 2002. DOI: 10.1142/S0217732302007715.

[23] M. Agostini et al. Results on Neutrinoless Double-β Decay of Ge76 from Phase I of the GERDA Experiment. *Phys. Rev. Lett.*, 111:122–503, 2013. DOI: 10.1103/PhysRevLett.111.122503.

[24] H. V. Klapdor-Kleingrothaus and I. V. Krivosheina. Why is the conclusion of the GERDA experiment not justified. *Phys.Part.Nucl.Lett.*, 10:704–709, 2013. DOI: 10.1134/S1547477113070133.

[25] N. Schmitz. *Neutrinophysik.* Teubner Verlag, 1997. ISBN: 9783519032366.

[26] K. Grotz and H. V. Klapdor. *Die schwache Wechselwirkung in Kern-, Teilchen- und Astrophysik. Eine Einführung.* Teubner Verlag, 1. Edition, 1989. ISBN: 9783519030355.

[27] K. Zuber. *Neutrino Physics (Series in High Energy Physics, Cosmology and Gravitation).* Taylor und Francis, 1. Edition, 2003. ISBN: 9780750307505.

[28] C. F. V. Weizsäcker. Zur Theorie der Kernmassen. *Zeitschrift fur Physik*, 96:431–458, 1935. DOI: 10.1007/BF01337700.

[29] Provided by J. Timm. Universität Hamburg.

[30] F. Boehm and P. Vogel, editors. *Physics of Massive Neutrinos.* Cambridge University Press, 1992. ISBN: 0521418240.

[31] H. V. Klapdor and K. Muto. *Neutrinos.* Springer-Verlag, 1988. ISBN: 3642466508.

[32] M. Goeppert-Mayer. Double Beta-Disintegration. *Phys. Rev.*, 48(6):512–516, 1935. DOI: 10.1103/PhysRev.48.512.

[33] R. Arnold et al. Limits on different Majoron decay modes of ^{100}Mo, ^{116}Cd, ^{82}Se and ^{96}Zr for neutrinoless double beta decays in the NEMO-2 experiment. *Nuclear Physics A*, 678(3):341 – 352, 2000. DOI: 10.1016/S0375-9474(00)00326-2.

[34] R. Arnold et al. First results of the search of neutrinoless double beta decay with the NEMO 3 detector. *Phys.Rev.Lett.*, 95:182302, 2005. DOI: 10.1103/PhysRevLett.95.182302.

[35] F. Piquemal. The SuperNEMO Project. *Physics of Atomic Nuclei*, 69(12):2096–2100, 2006. DOI: 10.1134/S1063778806120131.

[36] W. H. Furry. On Transition Probabilities in Double Beta-Disintegration. *Phys. Rev.*, 56(12):1184–1193, 1939. DOI: 10.1103/PhysRev.56.1184.

[37] J. Schechter and J. W. F. Valle. Neutrinoless double-β decay in SU(2)×U(1) theories. *Phys. Rev. D*, 25:2951–2954, 1982. DOI: 10.1103/PhysRevD.25.2951.

[38] M. Duerr, M. Lindner, and A. Merle. On the Quantitative Impact of the Schechter-Valle Theorem. *JHEP*, 1106:091, 2011. DOI: 10.1007/JHEP06(2011)091.

[39] M. Hirsch, K. Muto, T. Oda, and H. V. Klapdor-Kleingrothaus. Nuclear structure calculations of $\beta^+\beta^+$, β^+/EC and EC/EC decay matrix elements. *Z.Phys.*, A347:151–160, 1994. DOI: 10.1007/BF01292371.

[40] E. Caurier et al. Influence of pairing on the nuclear matrix elements of the neutrinoless $\beta\beta$ decays. *Phys. Rev. Lett.*, 100(5):052503, 2008. DOI: 10.1103/PhysRevLett.100.052503.

[41] F. Simkovic et al. Anatomy of the $\nu\beta\beta$ nuclear matrix elements. *Phys. Rev. C*, 77(4):045503, 2008. DOI: 10.1103/PhysRevC.77.045503.

[42] J. Barea and F. Iachello. Neutrinoless double-β decay in the microscopic interacting boson model. *Phys. Rev. C*, 79(4):044301, 2009. DOI: 10.1103/PhysRevC.79.044301.

[43] F. Simkovic. Matrix elements for neutrinoless double beta decay. *Nuclear Physics B - Proceedings Supplements*, 229-232(0):160 – 164, 2012. Neutrino 2010. DOI: 10.1016/j.nuclphysbps.2012.09.026.

[44] O. Cremonesi. Neutrinoless double beta decay: Present and future. *Nuclear Physics B - Proceedings Supplements*, 118:287 – 296, 2003. Proceedings of the XXth International Conference on Neutrino Physics and Astrophysics. DOI: 10.1016/S0920-5632(03)01331-8.

[45] G. F. Knoll. *Radiation Detection and Measurement.* Wiley, 3. Edition, 2000. ISBN: 9780471073383.

[46] H. Bethe. *Experimental Nuclear Physics – Passage of radiation through matter*, Volume 1, Part II. John Wiley and Sons, Inc., NewYork, 1953.

[47] W. R. Leo. *Passage of Radiation Through Matter.* Springer Berlin Heidelberg, 1994. ISBN: 978-3-540-57280-0, DOI: 10.1007/978-3-642-57920-2_2.

[48] P. Theodórsson. *Measurement Of Weak Radioactivity.* Wspc, 1. Edition, 1996. ISBN: 9810223153.

[49] G. Heusser. Low-Radioactivity Background Techniques. *Annual Review of Nuclear and Particle Science*, 45(1):543–590, 1995. DOI: 10.1146/annurev.ns.45.120195.002551.

[50] M. Haffke et al. Background measurements in the gran sasso underground laboratory. *Nuclear Instruments and Methods in Physics Research Section A: Accelerators, Spectrometers, Detectors and Associated Equipment*, 643(1):36 – 41, 2011. DOI: 10.1016/j.nima.2011.04.027.

[51] H. Bateman. Solution of a system of differential equations occurring in the theory of radioactive transformations. *Proceedings of the Cambridge Philosophical Society, Mathematical and physical sciences*, 423, 1843.

[52] W. Wahl. *Radionuklid-Handbuch für den Anwender in der Spektrometrie im Strahlenschutz und der Medizin.* ISuS Publikationen, 4.3 Edition, 2007.

[53] J. A. Formaggio and C.J. Martoff. Backgrounds to sensitive experiments underground. *Annual Review of Nuclear and Particle Sciense*, 54:361–412, 2004.

[54] F. F. Khalchukov and others. Hadrons and other secondaries generated by cosmic-ray muons underground. *Il Nuovo Cimento*, 18C(5), 1995. DOI: 10.1007/BF02506782.

[55] P. Belli et al. Deep undergrund neutron flux measurement with large BF_3 counters. *Il Nuovo Cimento*, 101A(6), 1989. DOI: 10.1007/BF02800162.

[56] F. Arneodo et al. Neutron background measurement in the hall c of the gran sasso laboratory. *Il Nuovo Cimento*, 112A(8), 1999.

[57] M. Aglietta et al. Measurement of the neutron flux produced by cosmic-ray muons with LVD at Gran Sasso. 1999.

[58] M. Aglietta et al. Neutron flux generated by cosmic–ray muons at 5200 hg/cm^2 underground. depth–neutron intensity curve. *Il Nuovo Cimento*, 12C(4), 1989. DOI: 10.1007/BF02525079.

[59] S. R. Elliott and P. Vogel. DOUBLE BETA DECAY. *Annual Review of Nuclear and Particle Science*, 52(1):115–151, 2002. DOI: 10.1146/annurev.nucl.52.050102.090641.

[60] T. Bloxham et al. First results on double beta decay modes of Cd, Te and Zn isotopes with the COBRA experiment. *Phys.Rev.*, C76:025501, 2007. DOI: 10.1103/PhysRevC.76.025501.

[61] S. Agostinelli et al. Geant4 – a simulation toolkit. *Nuclear Instruments and Methods in Physics Research Section A: Accelerators, Spectrometers, Detectors and Associated Equipment*, 506(3):250 – 303, 2003. DOI: 10.1016/S0168-9002(03)01368-8.

[62] J. Allison et al. Geant4 developments and applications. *Nuclear Science, IEEE Transactions on*, 53(1):270–278, 2006. DOI: 10.1109/TNS.2006.869826.

[63] G. A. P. Cirrone et al. Validation of the Geant4 electromagnetic photon cross-sections for elements and compounds. *Nuclear Instruments and Methods in Physics Research Section A: Accelerators, Spectrometers, Detectors and Associated Equipment*, 618(1-3):315 – 322, 2010. DOI: 10.1016/j.nima.2010.02.112.

[64] D. Wright. Shielding Physics List Description. 2012.

[65] V. Uzhinsky. Development of the Fritiof model in Geant4. *INIS*, 43, 2010. Proceedings of SNA + MC2010: Joint international conference on supercomputing in nuclear applications + Monte Carlo 2010.

[66] B. Andersson et al. A model for low-pT hadronic reactions with generalizations to hadron-nucleus and nucleus-nucleus collisions. *Nuclear Physics B*, 281(1-2):289 – 309, 1987. DOI: 10.1016/0550-3213(87)90257-4.

[67] A. Heikkinen et al. Bertini intranuclear cascade implementation in GEANT4. *eConf*, C0303241:MOMT008, 2003. ArXiv: nucl-th/0306008.

[68] Geant4 Collaboration. FTFP_BERT Physics List Description.

[69] Y. Watanabe et al. Status of jendl high energy file. *Journal of Korean Physical Society*, 59(2):1040–1045, 2011. DOI: 10.3938/jkps.59.1040.

[70] Nuclear Data Center. JENDL High Energy File 2007.

[71] M. B. Chadwick et al. ENDF/B-VII.1 Nuclear Data for Science and Technology: Cross Sections, Covariances, Fission Product Yields and Decay Data. *Nuclear Data Sheets*, 112(12):2887 – 2996, 2011. Special Issue on ENDF/B-VII.1 Library. DOI: 10.1016/j.nds.2011.11.002.

[72] L. Reichhart et al. Measurement and simulation of the muon-induced neutron yield in Lead. *Astropart.Phys.*, 47:67–76, 2013. DOI: 10.1016/j.astropartphys.2013.06.002.

[73] J. Apostolakis et al. Geometry and physics of the Geant4 toolkit for high and medium energy applications. *Radiation Physics and Chemistry*, 78(10):859–873, 2009. DOI: 10.1016/j.radphyschem.2009.04.026.

[74] J. Apostolakis et al. The performance of the Geant4 standard EM package for LHC and other applications. *Journal of Physics: Conference Series*, 119(3):032004, 2008. DOI: 10.1088/1742-6596/119/3/032004.

[75] T. Köttig. *Sensitivity Studies of CdZnTe Semiconductor Detectors for the COBRA Experiment.* PhD Thesis, TU Dortmund, 2012.

[76] R. Chytracek et al. Geometry Description Markup Language for Physics Simulation and Analysis Applications. *Nuclear Science, IEEE Transactions on*, 53(5):2892–2896, 2006. DOI: 10.1109/TNS.2006.881062.

[77] X-5 Monte Carlo Team. *MCNP – A General Monte Carlo N-Particle Transport Code.* 5. Edition, 2003.

[78] K. Zuber. COBRA–double beta decay searches using CdTe detectors. *Physics Letters B*, 519(1-2):1 – 7, 2001. DOI: 10.1016/S0370-2693(01)01056-5.

[79] S. Rahaman et al. Double-beta decay Q values of 116Cd and 130Te . *Physics Letters B*, 703(4):412 – 416, 2011. DOI: 10.1016/j.physletb.2011.07.078.

[80] Provided by D. Gehre. TU Dresden.

[81] M. Schwenke et al. Exploration of Pixelated detectors for double beta decay searches within the COBRA experiment. *Nuclear Instruments and Methods in Physics Research Section A: Accelerators, Spectrometers, Detectors and Associated Equipment*, 650(1):73 – 78, 2011. DOI: 10.1016/j.nima.2010.12.128.

[82] P. N. Luke. Single-polarity charge sensing in ionization detectors using coplanar electrodes. *Applied Physics Letters*, 65(22):2884–2886, 1994. DOI: 10.1063/1.112523.

[83] O. Frisch. British Atomic Energy Report BR-49. 1944.

[84] Z. He. Review of the Shockley-Ramo theorem and its application in semiconductor gamma-ray detectors. *Nuclear Instruments and Methods in Physics Research Section A: Accelerators, Spectrometers, Detectors and Associated Equipment*, 463(1-2):250 – 267, 2001. DOI: 10.1016/S0168-9002(01)00223-6.

[85] M. Fritts et al. Analytical model for event reconstruction in coplanar grid CdZnTe detectors. *Nuclear Instruments and Methods in Physics Research A*, 708:1–6, 2013. DOI: 10.1016/j.nima.2013.01.004.

[86] T. Neddermann. *Material Screening by means of Low-level Gamma Ray Spectrometry with the Dortmund Low Background HPGe Facility*. PhD Thesis, TU Dortmund, 2014.

[87] M. Fritts et al. Current Status and Future Perspectives of the COBRA Experiment. *Adv.High Energy Phys.*, 2013:703572, 2013. DOI: 10.1155/2013/703572.

[88] D. Schwickert. *Background analysis regarding the radioactive contamination of the Delrin holders of the COBRA detectors*. Bachelor Thesis, Universität Hamburg, 2014.

[89] M. Fritts et al. Pulse-shape discrimination of surface events in CdZnTe detectors for the COBRA experiment. *Nucl.Instrum.Meth.*, A749:27–34, 2014. DOI: 10.1016/j.nima.2014.02.038.

[90] J. Hong et al. Laboratory tests on neutron shields for gamma-ray detectors in space. *Nuclear Instruments and Methods in Physics Research Section A: Accelerators, Spectrometers, Detectors and Associated Equipment*, 452(1-2):192 – 204, 2000. DOI: 10.1016/S0168-9002(00)00428-9.

[91] D. Y. Stewart et al. Radiation shielding for underground low-background experiments. *AIP Conf. Proc.*, 870:568–571, 2006. DOI: 10.1063/1.2402703.

[92] C. Oldorf. *Thesis currently in preparation*. PhD Thesis, Universität Hamburg, 2014.

[93] Provided by S. Rajek. TU Dortmund.

[94] H. Wulandari. *Study on Neutron – Induced Background in the Dark Matter Experiment CRESST*. PhD Thesis, Technische Universität München, 2003.

[95] D.-M. Mei and A. Hime. Muon-induced background study for underground laboratories. *Physical Review D*, 73, 2006. DOI: 10.1103/PhysRevD.73.053004.

[96] M. Ambrosio et al. Measurement of the residual energy of muons in the Gran Sasso underground laboratories. *Astropart. Phys.*, 19:313–328, 2003. ArXiv: hep-ex/0207043.

[97] S. Zatschler. *Identification of Multi-Site Events in Coplanar-Grid CdZnTe-Detectors for the COBRA-Experiment.* Master's Thesis, TU Dresden, 2014.

[98] G. J. Feldman and R. D. Cousins. Unified approach to the classical statistical analysis of small signals. *Phys. Rev. D*, 57:3873–3889, 1998. DOI: 10.1103/PhysRevD.57.3873.

[99] O. Schulz. *Exploration of new Data Acquisition and Background Reduction Techniques for the COBRA Experiment.* PhD Thesis, TU Dortmund, 2011.

[100] K. Pearson. On the Criterion that a given System of Deviations from the Probable in the Case of a Correlated System of Variables is such that can be reasonably supposed to have arisen from Random Sampling. *Philosophical Magazine*, 50:157–175, 1900.

[101] C. Hagmann. Cosmic-ray Shower Library CRY. 2012.

[102] C. Hagmann. Cosmic-ray shower generator (cry) for monte carlo transport codes. *Nuclear Science Symposium Conference Record, 2007. NSS '07. IEEE*, 2:1143–1146, 2007. DOI: 10.1109/NSSMIC.2007.4437209.

[103] T. W. Armstrong. Calculations of neutron flux spectra induced in the Earth's atmosphere by galactic cosmic rays. *Journal of Geophysical Research*, 78(16):2715–2726, 1973. DOI: 10.1029/JA078i016p02715.

[104] M. S. Gordon et al. Measurement of the flux and energy spectrum of cosmic-ray induced neutrons on the ground. *Nuclear Science, IEEE Transactions on*, 51(6):3427–3434, 2004. DOI: 10.1109/TNS.2004.839134.

[105] Provided by B. Wonsak. Universität Hamburg.

[106] Measured by M. Laubenstein / Provided by S. Rajek. LNGS, Italy / TU Dortmund.

[107] Chemical lab of Servizio di Chimica-Impianti Chimici LNGS. LNGS, Italy.

[108] S. Kietzmann. *Background Studies for the COBRA Experiment Concerning the Natural Decay Chains and 113Cd.* Master's Thesis, Universität Hamburg, 2010.

[109] J. H. K. Timm. *Thesis currently in preparation.* PhD Thesis, Universität Hamburg, 2014.

[110] H. Rebber. *Thesis currently in preparation.* Master's Thesis, Universität Hamburg, 2015.

[111] Verein für Kernverfahrenstechnik und Analytik Rossendorf e. V. Dresden.

[112] ILIAS database on radiopurity of materials. URL: http://radiopurity.in2p3.fr/.